Bhlhe40 Coordinates T Cell Programs with Distinct CD4 and CD8 T Cell Requirements for Anti-PD-1 Versus Anti-CTLA-4

Akata Saha[1], Tomoyuki Minowa[1], Alexander S. Shavkunov[1], Avery J. Salmon[1], Sunita Keshari[1], Nicholas N. Jarjour[2*], Kristen E. Pauken[1], Kenneth H. Hu[1,3], Brian T. Edelson[2], Ken Chen[4], Matthew M. Gubin[1#]

1. Department of Immunology, The University of Texas MD Anderson Cancer Center, Houston, TX, USA

2. Department of Pathology and Immunology, Washington University School of Medicine, St. Louis, MO, USA

3. The Parker Institute for Cancer Immunotherapy, The University of Texas MD Anderson Cancer Center, Houston, TX, USA

4. Department of Bioinformatics and Computational Biology, The University of Texas MD Anderson Cancer Center, Houston, TX, USA

*Current address: Versiti Blood Research Institute, Milwaukee, WI and Department of Biochemistry, Medical College of Wisconsin, Milwaukee, WI, USA

M.M. Gubin reports a personal honorarium from Springer Nature Ltd for his role as a Deputy Editor for the journal Nature Precision Oncology and serves as a paid consultant for Merck. No disclosures were reported by the other authors.

#Corresponding author:

Matthew M. Gubin, PhD
Department of Immunology
The University of Texas MD Anderson Cancer Center
7455 Fannin St., Unit 901
Houston, TX 77054
Phone (713) 713-745-9790
Email mgubin@mdanderson.org

HIGHLIGHTS:

Bhlhe40 is essential in CD8 T cells for anti-PD-1 ICT, but dispensable for anti-CTLA-4 due to compensatory CD4 T cell function

CD8 T cell-intrinsic Bhlhe40 drives effector/exhausted states over TCF-1^{+} naïve and progenitor-exhausted like phenotypes

Bhlhe40 sustains T cell metabolic fitness, supporting glycolysis under both therapies and OXPHOS primarily during anti-PD-1

CD8 T cell-intrinsic Bhlhe40 is required for full ICT-driven macrophage remodeling

In human cancers, Bhlhe40 is enriched in tumor-reactive CD4 and CD8 T cells, positively linked to *TOX*/*IFNG* and inversely to *TCF7* (TCF-1)

ABSTRACT:

The transcriptional programs that enable CD4 and CD8 T cells to mediate effective anti-tumor immunity remain incompletely defined. Here, we identify distinct, therapy-specific roles for the transcriptional regulator Bhlhe40 in CD4 and CD8 T cells, revealing divergent requirements during anti-PD-1 versus anti-CTLA-4 immune checkpoint therapy (ICT). Using conditional knockout mice, we show that anti-PD-1 efficacy depends on CD8 T cell-intrinsic Bhlhe40 and may also require its expression in CD4 T cells, whereas anti-CTLA-4 relies primarily on CD4 T cell-intrinsic Bhlhe40 and remains effective without Bhlhe40 in CD8 T cells. Loss of Bhlhe40 skews CD8 T cells toward TCF-1-expressing naïve and progenitor exhausted-like states, particularly in the absence of ICT. Bhlhe40 sustains CD8 effector and exhausted phenotypes, promotes IFN-γ production, and supports glycolytic and mitochondrial programs, with Bhlhe40 deficiency leading to impaired glycolysis under either anti-PD-1 or anti-CTLA-4 ICT, and reduced mitochondrial function primarily during anti-PD-1. In addition, CD8 T cell-intrinsic Bhlhe40 is required for full ICT-induced remodeling of the tumor myeloid compartment from CX3CR1^{+} macrophages to iNOS^{+} macrophages. In contrast, anti-CTLA-4 can drive tumor rejection and partial macrophage remodeling in the absence of CD8 T cell-intrinsic Bhlhe40, provided CD4 T cell function is intact. Analysis of human cancer datasets revealed that *BHLHE40* is enriched in tumor-reactive and activated/exhausted CD8 T cells, where its expression is inversely correlated with *TCF7* (TCF-1) and positively associated with *TOX* and *IFNG*. Moreover, subsets of CD8 T cells expressed higher levels of *BHLHE40* in basal and squamous cell carcinoma responders compared with non-responders. Together, these findings establish Bhlhe40 not only as a transcriptional coordinator of T cell effector programs and metabolic fitness, but also as a therapy-specific, subset-dependent determinant of ICT efficacy, providing a mechanistic basis for the divergent modes of action of anti-PD-1 versus anti-CTLA-4.

INTRODUCTION:

Immune checkpoint therapy (ICT) targeting PD-1 or CTLA-4 can elicit durable tumor regression in some patients, but many fail to respond[1-7]. While tumor-reactive T cells are central to ICT efficacy[8-16], the transcriptional programs that enable CD4 and CD8 T cells to mediate effective anti-tumor immunity remain incompletely defined[17-19]. Understanding these requirements is particularly important because anti-PD-1 and anti-CTLA-4 each act through both overlapping as well as distinct mechanisms[20,21]. Basic helix-loop-helix family member e40 (Bhlhe40) has emerged as a critical transcription factor regulating immune responses[22]. Bhlhe40 can act as a transcriptional repressor but the mechanisms underlying this repression are not fully understood; in some cases, Bhlhe40 binds target genes and likely outcompetes transcriptional activators for occupancy (e.g., outcompeting transcriptional activators in promoter/enhancer regions of target loci, as observed with *Il10* [22-24]). Bhlhe40 can also function as a transcriptional activator, particularly when partnered with other transcription factors[25], and can also indirectly enhance transcription of certain T cell effector genes by sustaining intracellular acetyl-CoA levels to promote histone acetylation[26]. Bhlhe40 is expressed across multiple cell types, including T cells[27-29]. We and others previously found that expression of Bhlhe40 in T cells is induced by TCR engagement and further enhanced by CD28 co-stimulation[29,30]. Cytokines such as GM-CSF and IL-1β can also induce Bhlhe40 expression, while PD-1 signaling can blunt its expression[22,26]. CD4-Cre Bhlhe40$^{fl/fl}$ mice, which lack Bhlhe40 in both CD4 and CD8 T cells, are resistant to experimental autoimmune encephalomyelitis, reflecting the requirement for Bhlhe40 to repress IL-10 and promote GM-CSF production in T cells[23,27,31]. Conversely, these mice exhibit increased susceptibility to certain infections, associated with elevated IL-10 and reduced IFN-γ production in the absence of Bhlhe40[24,32].

We recently demonstrated neoantigen (NeoAg)-specific intratumoral CD4 and CD8 T cells upregulate Bhlhe40 in tumor bearing mice treated with anti-PD-1 or anti-CTLA-4 ICT[29]. Using CD4-Cre Bhlhe40$^{fl/fl}$ mice—where deletion occurs in both CD4 and CD8 T cells—we found that T cell-intrinsic Bhlhe40 is essential for tumor rejection in response to either ICT. Global deletion of Bhlhe40 disrupted T cell effector gene expression and impaired ICT-driven remodeling of the tumor microenvironment (TME). Independent work demonstrated Bhlhe40 is required for response to anti-PD-1/PD-L1 ICT in preclinical models, with loss of T cell-intrinsic Bhlhe40 linked to defective mitochondrial fitness[26]. These findings established Bhlhe40 as a critical transcriptional regulator of ICT efficacy, but they did not reveal whether the requirement for Bhlhe40 is cell-type-specific, or whether its role differs between anti-PD-1 and anti-CTLA-4.

Here, we dissect the cell-type-specific requirements for Bhlhe40 in ICT by selectively deleting it in CD8 T cells or in both CD4 and CD8 T cells using tumor models where both subsets are essential for therapeutic response. We show that CD8 T cell-intrinsic Bhlhe40 is required for tumor control by anti-PD-1, with additional contributions from CD4 T cell-intrinsic Bhlhe40, whereas anti-CTLA-4 efficacy is largely dependent on CD4 T cell-intrinsic Bhlhe40 and remains intact when Bhlhe40 is absent from CD8 T cells. Loss of Bhlhe40 skews CD8 T cells toward a more naïve or progenitor exhausted-like state with elevated TCF-1 and reduced acquisition of terminal effector features, particularly in the absence of ICT. In addition, Bhlhe40 supports glycolysis under either anti-PD-1 or anti-CTLA-4 therapies, mitochondrial respiration primarily during anti-PD-1, and is required for full ICT-driven remodeling of the tumor myeloid compartment from CX3CR1^{+} to iNOS^{+} macrophages. Analysis of multiple human cancer datasets demonstrates that *BHLHE40* is enriched in tumor-reactive and activated/exhausted CD8 T cell populations across tumor types, inversely correlated with *TCF7*, and positively associated with *TOX* and *IFNG*. Together, these findings establish Bhlhe40 as a key regulator of T cell effector programming and metabolic fitness,

and as a transcriptional determinant of the subset-specific functions that underlie response to anti-PD-1 versus anti-CTLA-4 therapy.

RESULTS:

Human Tumor-Reactive CD4 and CD8 T Cells with Activated Phenotype Express Bhlhe40

We previously found that CD4-Cre Bhlhe40$^{f/f}$ (B$^{\Delta T}$) mice lacking Bhlhe40 in both CD4 and CD8 T cells exhibit profound defects in anti-PD-1- and anti-CTLA-4- driven TME remodeling and fail to respond to ICT[29]. Consistent with this requirement, Bhlhe40 expression was detected in both CD4 and CD8 T cells and was enriched in tumor NeoAg-specific T cells[29]. To extend these findings to human tumors, we first examined *BHLHE40* expression across immune cell types inferred from The Cancer Genome Atlas (TCGA) RNA-sequencing (RNA-seq) data. Both CD4 and CD8 T cells consistently expressed *BHLHE40* across multiple cancer types (**Figs. 1A** and **S1**). Next, we reanalyzed basal cell carcinoma patient datasets (Yost et al.)[33] containing pre- and post-treatment samples from responders and non-responders treated with PD-1 blockade. Pre-treatment, CD8 T cells classified by Yost et al. as "activated" or "exhausted" expressed higher levels of *BHLHE40* in responders compared with non-responders, and post-treatment, exhausted CD8 T cells showed elevated *BHLHE40* expression in responders (**Fig. 1B**).

We next asked whether the association of Bhlhe40 with tumor-infiltrating T cells observed in mice is also evident in human cancers. Tumor-reactive CD8 T cells were identified in studies by Oliveira et al. and Minowa et al. [34,35], which analyzed human cutaneous melanoma (an immunogenic tumor type that frequently responds to ICT), and acral melanoma (a less immunogenic tumor type), respectively. Despite these differences, reanalysis of datasets from both these studies revealed enrichment of *BHLHE40* in tumor-reactive CD8 T cells compared with CD8 T cells that are likely predominately non-tumor-reactive bystanders (**Fig. 1C**). Overall, these findings align with our

observations in murine models, where Bhlhe40 is expressed in both CD4 and CD8 T cells, particularly within tumor-reactive populations[29].

CD8 T Cell-Intrinsic Bhlhe40 Is Essential for Anti-PD-1 but Not Anti-CTLA-4 Efficacy

We previously used *CD4-Cre Bhlhe40*$^{fl/fl}$ conditional knockout (KO) mice in which Bhlhe40 is deleted in both CD4 and CD8 T cells because CD4-Cre is expressed in CD4^{+} CD8^{+} double-positive thymocytes that later differentiate into CD4 or CD8 T cells[36]. Consequently, we sought to determine whether Bhlhe40 expression specifically within CD8 T cells is required for the therapeutic efficacy of anti-PD-1 or anti-CTLA-4 ICT. We used *CD8 E8I-Cre* mice, in which Cre recombinase is driven by the E8I CD8 enhancer that is active exclusively in CD8 T cells[37]. We crossed *CD8 E8I-Cre* mice with *Bhlhe40*$^{fl/fl}$ mice [*CD8 E8I-Cre Bhlhe40*$^{fl/fl}$ (B$^{\Delta CD8}$)] to conditionally delete Bhlhe40 specifically in CD8 T cells (and not CD4 T cells) and verified the specificity of the deletion (**Fig. S2A**). Next, we used the well-characterized 1956 MCA sarcoma transplant model[29,38,39], injecting tumor cells into *Bhlhe40*$^{fl/fl}$ (B$^{f/f}$) (control mice), B$^{\Delta CD8}$ (Bhlhe40 KO in CD8 T cells), B$^{\Delta T}$ (Bhlhe40 KO in CD4 and CD8 T cells) mice and treated mice with isotype control antibody (Ab), anti-PD-1, or anti-CTLA-4 (**Fig. 2A**). Consistent with our prior findings[29], tumor outgrowth was observed in B$^{\Delta T}$ mice treated with anti-PD-1 or anti-CTLA-4 (**Fig. S2B**). While tumor regression occurred in anti-PD-1-treated B$^{f/f}$ mice, anti-PD-1 failed to control tumor growth in B$^{\Delta CD8}$ mice (**Figs. 2B, 2C,** and **S2C**). Interestingly, anti-CTLA-4 elicited effective tumor control in both B$^{f/f}$ and B$^{\Delta CD8}$ mice. We obtained similar results using the *Braf*^{V600E} *Pten*$^{-/-}$ *Cdkn2*$^{-/-}$ YUMM1.7[40]-modified Y1.7LI melanoma model[41] (**Figs. S3A-S3C**). To confirm that expression of Cre itself does not affect anti-tumor immune responses, we compared *CD8 E8I-Cre Bhlhe40*$^{+/+}$ mice to B$^{f/f}$ mice and observed comparable tumor growth and responses to ICT (**Fig. S3D**). Altogether, these results demonstrate that CD8 T cell-intrinsic Bhlhe40 is required for anti-PD-1 efficacy but is not necessary for response to anti-CTLA-4.

Bhlhe40 Governs CD8 T Cell Functions Driving Anti-PD-1 Responses

To gain insights into the divergent effects of anti-PD-1 and anti-CTLA-4 therapies in the absence of Bhlhe40 in CD8 T cells, we performed single-cell RNA sequencing (scRNAseq) on immune cells isolated from tumors of Bhlhe40-sufficient ($B^{f/f}$) and T cell-specific Bhlhe40 knockout mice, including CD8 T cell-restricted knockout ($B^{\Delta CD8}$) and CD4 and CD8 T cell knockouts ($B^{\Delta T}$). 1956 tumor bearing $B^{f/f}$, $B^{\Delta CD8}$, and $B^{\Delta T}$ mice were treated with control Ab, anti-PD-1, or anti-CTLA-4 and harvested on day 10 post-tumor transplant to capture immune remodeling events independent of subsequent gross tumor size differences between groups (**Fig. S4A**). Live Thy1.2^{+} CD45^{+} and Thy1.2^{-} CD45^{+} immune cells were sorted and mixed at 60:40 ratio to enhance capture of less frequent lymphoid cells for scRNAseq. While we were able to identify lymphoid and myeloid subpopulations, to further increase lymphocyte resolution by accumulating more lymphocytes, we performed an additional experiment under the same treatment conditions, this time focusing specifically on Thy1.2^{+} CD45^{+} lymphocytes from $B^{f/f}$ and $B^{\Delta CD8}$ mice (**Fig. S4A**). We then extracted CD4 and CD8 T cells based on gene expression from each experimental dataset and integrated the scRNAseq data from both experiments for downstream analysis of CD4 and CD8 T cells (**Fig. S4B**).

We first focused on comparing CD8 T cells from $B^{f/f}$ mice to $B^{\Delta CD8}$ mice. While anti-CTLA-4 increased the overall frequency of CD8 T cells in $B^{f/f}$ mice, no significant changes were observed across other conditions (**Fig. S4C**). However, both anti-PD-1 and anti-CTLA-4 increased the frequency of tumor-specific CD8 T cells recognizing mutant Psmd6, an MHC class I (MHC-I) mutant NeoAg in the 1956 tumor[38] (**Fig. 2D**). Notably, anti-CTLA-4 drove this increase regardless of CD8 T cell-intrinsic Bhlhe40, whereas anti-PD-1 only increased Psmd6-specific CD8 T cells in $B^{f/f}$ control mice, but not in $B^{\Delta CD8}$ mice. Continuing our focus on CD8 T cells, we performed unsupervised clustering of *Cd3e*$^{+}$ *Cd8a*$^{+}$ cells from our scRNAseq experiment and identified seven

CD8 T cell clusters (plus two small clusters of non-CD8 T cells). These spanned a range of states and included effector or exhausted (PD1^{hi}_Eff_Ex; Nr4a1^{hi}_Eff_Ex; Cd39^{+} Eff_Ex; Tox^{hi}_Eff_Ex), cycling/proliferating cells (Eff_Cycling), progenitor exhausted (Pex)-like/interferon-stimulated cells (Pexlike_Ifn-Stim), and naïve/memory-like populations (Naïve_Mem) based on functional marker transcript expression and comparisons to published datasets[34,42-45] (**Figs. 2E-2H, S4D, S4E,** and **S5**).

Treatment with ICT reshaped the CD8 T cell compartment in a manner that was genotype-dependent and in some cases dependent on whether mice were treated with anti-PD-1 or anti-CTLA-4 **(Fig. S4F)**. We first noted that, as expected, clusters PD1^{hi}_Eff_Ex, Nr4a1^{hi}_Eff_Ex, and Tox^{hi}_Eff_Ex expressed the highest levels of *Bhlhe40* in B$^{f/f}$ mice (**Figs. 2F, 2G, S4D,** and **S4E**). In addition to Bhlhe40, PD1^{hi}_Eff_Ex expressed relatively high levels of inhibitory receptor transcripts [*Pdcd1* (PD-1), *Lag3*, *Havcr2* (TIM-3)], which are induced upon TCR activation but become hallmarks of exhausted and/or dysfunctional CD8 T cells[46], especially when their expression is high and sustained[47-50], as well as key effector molecules (*Ifng*, *Gzmb*, *Prf1*) (**Figs. S4D, S4E,** and **S5**). In B$^{f/f}$ mice, anti-PD-1 or anti-CTLA-4 expanded PD1^{hi}_Eff_Ex (**Fig. S4F**). Anti-PD-1 still drove expansion of this cluster even in the absence of *Bhlhe40* in CD8 T cells (B$^{\Delta CD8}$ mice), as did anti-CTLA-4, though to a lesser extent in B$^{\Delta CD8}$ mice. Cluster Nr4a1^{hi}_Eff_Ex was noted for its expression of *Nr4a1* (Nur77), an early gene upregulated proportionally to TCR signaling strength[51,52] (**Figs. 2F, S4D,** and **S5**). Cluster Nr4a1^{hi}_Eff_Ex also expressed *Pdcd1* and *Lag3* but to less of an extent compared to PD1^{hi}_Eff_Ex and expressed higher levels of *Havcr2, Ifng, Gzmb,* and *Cd69* (**Figs. 2F, S4D, S4E,** and **S5**). Neither anti-PD-1 nor anti-CTLA-4 had notable effects on the frequency of Nr4a1^{hi}_Eff_Ex in both B$^{f/f}$ and B$^{\Delta CD8}$ mice, albeit anti-CTLA-4 slightly increased this population in B$^{f/f}$ mice (**Fig. S4F**). Tox^{hi}_Eff_Ex was the smallest CD8 T cell cluster that, in addition to high levels of *Tox* and *Havcr2*, expressed *Pdcd1*, *Lag3*, and *Entpd1* (CD39) as well as *Tcf7* and *Slamf6* (Ly108), although expression of the latter two transcripts

occurred within a subset of cells within this cluster and was partially exclusive of *Tox* expression (**Figs. 2E, 2F, S4D, S4E, S4G,** and **S5**). TOX is a transcription factor essential for enforcing exhausted/dysfunctional T cell states[53-56], whereas TCF-1 (Tcf7) promotes stem-like Pex T cells, which are critical for sustaining responses under anti-PD-1 and promoting anti-CTLA-4-driven T cell memory[17,43,57-62]. This cluster saw minor increases in frequency with anti-PD-1 and minor decreases with anti-CTLA-4 that was independent of Bhlhe40 expression in CD8 T cells (**Fig. S4F**).

Clusters Eff_Cycling and Cd39^{+} Eff_Ex expressed *Bhlhe40* at moderate levels, whereas cluster Pex-like_Ifn-stim expressed lower levels of Bhlhe40 (**Figs. 2F, 2G, S4D,** and **S4E**). The proportion of cells within Eff_Cycling was reduced with anti-PD-1, independent of Bhlhe40 presence or absence in CD8 T cells (**Fig. S4F**). This cluster was also reduced with anti-CTLA-4 but less so in B$^{\Delta CD8}$ mice as compared to B$^{f/f}$ mice. Cd39^{+} Eff_Ex was a small cluster of CD8 T cells that only displayed subtle proportional changes with anti-CTLA-4. Cluster Pex-like_Ifn-stim displayed upregulation of interferon (IFN)-stimulated transcripts (e.g., *Usp18*, *Ifit2*), high *Gzmk* expression, and also expressed *Cd69*, *Tcf7*, and *Slamf6*—transcripts also expressed by Pex CD8 T cells—and represented about 15% of CD8 T cells in B$^{f/f}$ mice, with anti-PD-1-treated B$^{f/f}$ and B$^{\Delta CD8}$ mice displaying similar frequencies (**2F, S4D, S4E,** and **S5**). The frequency of cells within this cluster increased with anti-CTLA-4 in B$^{f/f}$ but not B$^{\Delta CD8}$ mice (**Fig. S4F**). In control Ab-treated tumors, Pex-like_Ifn-stim was dramatically reduced in B$^{\Delta CD8}$ mice (from 14.39% to 8.46%), whereas anti-PD-1 decreased this cluster in both B$^{f/f}$ and B$^{\Delta CD8}$ mice as compared to control Ab-treated B$^{f/f}$ mice. This cluster represented 20.49% of CD8 T cells in anti-CTLA-4-treated B$^{f/f}$ and 14.84% in B$^{\Delta CD8}$ mice (**Fig. S4F**).

We previously found that CD8 T cells from mice lacking Bhlhe40 in both CD4 and CD8 T cells exhibited altered responses to ICT, including defects in IFN-γ expression[29]; however, it was

unclear whether these changes were due to a CD8 T cell-intrinsic requirement for Bhlhe40 or reflected indirect effects stemming from its ablation in CD4 T cells. Our use of $B^{\Delta CD8}$ mice now demonstrates that some of these Bhlhe40-dependent changes, including reduced IFN-γ production by CD8 T cells, are at least partially attributable to CD8 T cell-intrinsic Bhlhe40. Specifically, cluster Nr4a1^{hi}_Eff_Ex, which exhibited the highest levels of *Ifng* among CD8 T cell clusters (**Figs. S4D, S4E,** and **S5**), as well as PD1^{hi}_Eff_Ex, Tox^{hi}_Eff_Ex, and Eff_Cycling clusters, all showed reduced *Ifng* expression in $B^{\Delta CD8}$ mice compared to $B^{f/f}$ mice within the corresponding treatment groups (**Figs. S6A**). Notably, this reduction in *Ifng* was observed not only with anti-PD-1—which fails to induce rejection in $B^{\Delta CD8}$ mice—but also with anti-CTLA-4, despite the latter still leading to tumor rejection in $B^{\Delta CD8}$ mice. While CD8 T cell-intrinsic Bhlhe40 contributes to *Ifng* production by CD8 T cells, the even more pronounced reduction of *Ifng* expression in mice lacking Bhlhe40 in both CD8 and CD4 T cells ($B^{\Delta T}$) suggests that Bhlhe40 expression in CD4 T cells also supports *Ifng* production by CD8 T cells (**Fig. S6A**). At the protein level, although the frequency of IFN-γ-positive cells as a percentage of CD8 T cells did not change significantly between $B^{f/f}$ and $B^{\Delta CD8}$ mice with anti-PD-1 treatment, the expression level of IFN-γ was significantly decreased based on mean fluorescence intensity (MFI) (**Fig. 3A**). Interestingly, CD8 T cells from $B^{\Delta CD8}$ mice treated with anti-CTLA-4 also displayed defects in IFN-γ production as compared to $B^{f/f}$ mice (**Fig. 3A**). Further, a significant decrease in IFN-γ^+ TNF-α^+ CD8 T cells was observed in $B^{\Delta CD8}$ mice compared to $B^{f/f}$ mice within the corresponding treatment groups (**Fig. 3A**). In addition to alterations in *Ifng*, which is known to be transcriptionally enhanced by Bhlhe40[25], *Il10* expression was increased in the PD1^{hi}_Eff/Ex and Nr4a1^{hi}_Eff/Ex clusters in $B^{\Delta CD8}$ mice (**Fig. S6B**), consistent with prior reports that Bhlhe40 acts as a transcriptional repressor of *Il10*[23,24,28].

Gene set enrichment analysis (GSEA) revealed that, under anti-PD-1 treatment, the largest CD8 cluster, PD1^{hi}_Eff/Ex, as well as Pexlike_Ifn-stim and Tox^{hi}_Eff/Ex, from $B^{\Delta CD8}$ mice were

significantly negatively enriched for the Hallmark interferon-gamma (IFN-γ) response gene set compared to $B^{f/f}$ mice, with the Pexlike_Ifn-stim and Tox^{hi}_Eff/Ex additionally showing negative enrichment for the Hallmark interferon-alpha (IFN-α) response gene set (**Figs. 3B** and **S7**). Under anti-CTLA-4 treatment, $PD1^{hi}$_Eff/Ex, Naïve_Mem, and Tox^{hi}_Eff/Ex clusters from $B^{\Delta CD8}$ mice exhibited negative enrichment for IFN-γ response with $Nr4a1^{hi}$_Eff/Ex and Naïve_Mem additionally showing negative enrichment for IFN-α response (**Fig. 3B** and **S8**), despite anti-CTLA-4 treatment being capable of rejecting tumors even without Bhlhe40 in CD8 T cells. Although IFN-γ can be produced by several immune cell types, this reduction is likely attributable, at least in part, to impaired IFN-γ production by Bhlhe40-deficient CD8 T cells. In contrast, IFNα is not typically produced by T cells, suggesting that diminished IFNα response may reflect secondary effects driven by altered CD8 T cell function in the absence of Bhlhe40. Interestingly, although certain CD8 T cell clusters from $B^{\Delta CD8}$ mice displayed significant negative enrichment for IFN-γ response genes under anti-CTLA-4 treatment relative to $B^{f/f}$ controls, these same clusters nevertheless showed relative enrichment of IFN-γ signaling when comparing anti-CTLA-4- versus anti-PD-1-treated $B^{\Delta CD8}$ mice (**Fig. 3C**).

Bhlhe40 Contributes to Transition Toward Effector and Exhausted CD8 T Cell States

We noted that expression of *Pdcd1* and the fractalkine receptor gene *Cx3cr1* was notably reduced in $B^{\Delta CD8}$ mice when comparing like treatment conditions in several CD8 T cell clusters (**Fig. S9**). Bhlhe40-deficient CD8 T cells exhibited increased expression of *Gzmb,* as well as *Cd5*, *Cd6*, *Ptprj*, *Pag1*, and *Igfrl1* across several clusters of CD8 T cells from $B^{\Delta CD8}$ mice when compared to $B^{f/f}$ mice across all treatment groups (**Figs. S5** and **S9**). Anti-PD-1 drove an increase in *Tox* expression and, as expected, anti-CTLA-4 reduced *Tox* expression in CD8 T cells when compared to control treatment in $B^{f/f}$ mice (**Fig. 3D**). However, expression of *Tox* was less in anti-PD-1-treated $B^{\Delta CD8}$ mice compared to $B^{f/f}$ mice. While some of these findings (such as reduced *Pdcd1, Cx3cr1*, and *Tox*) suggest that CD8 T cells lacking Bhlhe40 may fail to fully acquire a differentiated effector

or exhausted phenotype, others (such as increased expression of *Gzmb, Cd5*, *Cd6, Ptprj, Pag1*, and *Igfrl1*) point to a compensatory or dysregulated activation state, in which CD8 T cells are activated but not properly guided into functional effector or exhausted states.

We further explored the relationship between Bhlhe40 expression and CD8 phenotype-defining programs. Correlation analysis revealed an inverse relationship between *Bhlhe40* and *Tcf7*, *Sell*, *Id3*, *Bcl2*, *Cxcr3* and, to a lesser extent, *Lef1*, *Slamf6*, and *Eomes*, genes associated with naïve, memory-like, and/or Pex-like phenotypes (**Figs. 3E** and **S10**). In contrast, *Bhlhe40* was associated with transcripts linked to T cell activation, effector differentiation, and exhaustion, including *Junb, Jund, Rbpj, Bcl2a1b, Rgs16,* and *Irf8,* as well as genes related to cytotoxicity (*Nkg7*, *Srgn*, *Serpinb9*), costimulatory receptors (*Tnfrsf4* [OX40], *Tnfrsf9* [4-1BB], *Icos*), and inhibitory receptors (*Pdcd1*, *Ctla4, Lag3, Havcr2, Klrc1* [NKG2A]) (**Figs. 3E** and **S10**). *Bhlhe40* expression was positively associated with *Dusp5*, which encodes an ERK1/2-specific phosphatase that regulates CD8 T cell survival and differentiation and controls the balance between short-lived effectors and memory precursor effectors[63,64]. *Bhlhe40* expression also correlated with *Nr4a1* and *Hif1a*, genes encoding TCR-induced transcription factors, the latter of which is further stabilized under hypoxic conditions, along with the HIF1-activated gene *Hilpda*.

It is not unexpected that Bhlhe40 was positively correlated with genes associated with activated, effector, and exhausted phenotypes given that TCR stimulation and CD28 co-stimulation can drive Bhlhe40 expression[29,30]; however, the expression pattern of certain key transcripts in $B^{\Delta CD8}$ mice suggest that Bhlhe40 may be influencing some of the changes associated with differentiation into effector and exhausted CD8 T cells. Cluster naïve/memory expressed the highest levels of *Tcf7* (**Figs. 3F, S5,** and **S11A**), and this cluster was dramatically expanded in control Ab-treated $B^{\Delta CD8}$ mice as compared to control Ab treated $B^{f/f}$ mice (**Fig. S4F**). Further, in several CD8 T cell clusters (including those where only a small percentage of cells expressed *Tcf7*), we noted higher

expression of *Tcf7* was observed in $B^{\Delta CD8}$ mice as compared to $B^{f/f}$ mice, especially in the absence of ICT (**Fig. 3F**). This was particularly noteworthy in the Tox^{hi} cluster, where $B^{\Delta CD8}$ mice not only showed an increased frequency of cells within the cluster but also a marked rise in both the proportion of *Tcf7*-expressing cells and their expression levels (**Figs. 3F** and **S4F**). Notably, in $B^{\Delta CD8}$ mice treated with control Ab, the frequency of intratumoral PD-1^+ TCF-1^+ CD8 T cells, as measured by protein expression, was significantly increased compared to $B^{f/f}$ mice (**Fig. 3G**). A less pronounced but still significant increase in PD-1^+ TCF-1^+ CD8 T cells was also observed in $B^{\Delta CD8}$ mice under anti-PD-1 treatment.

Although the relationship between Bhlhe40 and the aforementioned transcripts and proteins may be indirect, some of the observed changes are likely attributable to Bhlhe40-mediated transcriptional activation or repression of specific target genes. For example, Bhlhe40 has been shown to positively regulate *Ifng* and negatively regulate *Il10*[23,24,28], consistent with our findings. Further, *Tcf7* contains several E-box motifs within its regulatory regions and CUT&RUN experiments demonstrate direct binding of Bhlhe40 to these elements[65,66]. This raises the possibility that Bhlhe40 may not only be co-expressed with markers of activated, effector, or exhausted CD8 T cells due to shared upstream signals such as TCR stimulation, but may also contribute directly to driving CD8 T cell differentiation toward effector and exhausted phenotypes.

To further examine how Bhlhe40 loss influences the balance between effector/exhausted and progenitor-like CD8 T cell phenotypes, we utilized the OT-I TCR transgenic system. OT-I TCR transgenic mice were crossed with Bhlhe40$^{-/-}$ mice to generate Bhlhe40-deficient OT-I ($B^{-/-}$ OT-I) mice. To ensure *in vivo* relevance of this system, we first evaluated whether Bhlhe40 was required for OT-I CD8 T cell-mediated tumor control in an adoptive cell therapy model. Splenocytes from $B^{+/+}$ OT-I and $B^{-/-}$ OT-I mice were stimulated with SIINFEKL peptide, the ovalbumin (OVA)-derived cognate epitope presented by H2-K^b. Stimulated $B^{+/+}$ or $B^{-/-}$ OT-I cells were then isolated and

adoptively transferred into mice bearing B16-OVA melanomas. While transfer of $B^{+/+}$ OT-I CD8 T cells delayed tumor outgrowth, $B^{-/-}$ OT-I CD8 T cells failed to reduce tumor growth (**Fig. S11B**). We then used an *in vitro* culture assay to compare transcript expression of effector and exhaustion markers (*Pdcd1*, *Lag3*, *Havcr2*, *Ifng*) and memory-associated markers (*Tcf7*, *Il7r*) in $B^{+/+}$ and $B^{-/-}$ OT-I T cells under acute and chronic stimulation conditions. As expected, chronic stimulation led to increased *Pdcd1*, *Lag3*, and *Havcr2* expression and reduced *Tcf7* and *Il7r* expression in $B^{+/+}$ OT-I cells compared to acute stimulation (**Fig. 3H**). However, under both stimulation conditions, $B^{-/-}$ OT-I cells exhibited reduced expression of *Pdcd1*, *Lag3*, *Havcr2*, and *Ifng*, while *Tcf7* and *Il7r* expression remained significantly elevated relative to $B^{+/+}$ OT-I cells.

These results indicate that Bhlhe40 is required for the proper transcriptional programming and functional differentiation of effector and exhausted CD8 T cells. Loss of Bhlhe40 impairs upregulation of key activation and exhaustion markers, instead favoring the persistence of a more naïve or progenitor-like phenotype characterized by elevated *Tcf7* and *Il7r* expression. Collectively, our findings support a model in which Bhlhe40 functions as a transcriptional switch that promotes effector and exhausted CD8 T cell fates, at least in part through repression of *Tcf7*.

Bhlhe40 Correlates with Effector and Exhaustion Programs in Human Intratumoral CD8 T Cells

Reanalysis of single-cell RNA-sequencing datasets from human cancer patients revealed expression patterns between BHLHE40 and several transcripts associated with T cell differentiation states and function that were similar to those in mice. First, in the Yost et al. study[33], subsetting of CD8 T cell clusters identified in basal cell carcinoma revealed three distinct CD8 T cell states: activated, exhausted, and memory (**Fig. 4A**). *BHLHE40* expression was highest in the CD8 T cell clusters classified as activated or exhausted, whereas *TCF7* expression was inversely correlated. *TOX* expression was correlated with *BHLHE40*, as confirmed by gene correlation

analysis, which also indicated a relationship between *BHLHE40* and *PDCD1, ENTPD1*, *HAVCR2, LAG3, GZMB*, and *IFNG*. (**Figs. 4B** and **4C**). In triple-negative breast cancer (TNBC), *BHLHE40* was co-expressed with *TOX* and *IFNG* and inversely associated with *TCF7* expression (**Figs. 4D** and **4E**). Similar patterns of *BHLHE40* co-expression with *PDCD1, HAVCR2, LAG3, TOX, GZMB*, and *IFNG* and negative correlation with *TCF7* were observed in CD8 T cells from patients with melanoma (**Fig 4F**). Thus, in mice and across multiple human cancers, Bhlhe40 marks CD8 T cell states characterized by effector activity and exhaustion, suggesting a conserved role in shaping T cell differentiation and function within the TME.

Bhlhe40 Regulates Metabolic Programming in CD8 T Cells in a Context-Dependent Manner

Given that effector differentiation and cytokine production are tightly linked to metabolic rewiring, we next examined whether Bhlhe40 influences the metabolic profile of CD8 T cells within the TME. Correlations in expression of *Bhlhe40* and key glycolytic genes critical for supporting anabolic metabolism and effector function in the TME such as *Aldoa*, *Gapdh*, *Pgk1*, *Pkm, Tpi1, Ldha*, and *Eno1* were noted (**Figs. 3E** and **S10**), consistent with the glycolytic reprogramming characteristic of activated and effector CD8 T cells. Expression of *Aldoa, Gapdh, Eno1, Pgk1, Pfkp*, and *Tpi1*, were markedly reduced in anti-PD-1-treated $B^{\Delta CD8}$ mice compared to $B^{f/f}$ mice, particularly within the $PD1^{hi}$_Eff/Ex, $Nr4a1^{hi}$ _Eff/Ex, and Tox^{hi}_Eff/Ex CD8 T cell clusters that also display the highest *Bhlhe40* expression (**Figs. 5A, S4D, S4E, S5,** and **S12A**). Anti-CTLA-4-treated $B^{\Delta CD8}$ mice also exhibited reductions in glycolytic transcripts (**Fig. 5A**). Consistent with impaired metabolic activation, GSEA showed negative enrichment of glycolysis-associated gene sets across several effector clusters in $B^{\Delta CD8}$ mice treated with anti-PD-1 or anti-CTLA-4 relative to $B^{f/f}$ counterparts **(Figs. 5B, S7,** and **S8)**. Notably, in $Bhlhe40^{\Delta T}$ mice lacking Bhlhe40 in both CD4 and CD8 T cells, glycolytic gene expression was more severely impaired than in $B^{\Delta CD8}$ mice, suggesting a role for Bhlhe40 in CD4 T cells in facilitating CD8 T cell glycolytic fitness (**Fig. S12B**). Li et al. (2019) previously demonstrated that Bhlhe40 is required to sustain the expression

of transcripts essential for oxidative phosphorylation (OXPHOS), and its absence results in dysregulated OXPHOS[26]. Although we did not observe as extensive a reduction in OXPHOS-related transcripts in Bhlhe40-deficient CD8 T cells (**Fig. S12C**), GSEA revealed significantly decreased enrichment of OXPHOS-associated gene sets in several CD8 T cell clusters from anti-PD-1 and anti-CTLA-4 treated $B^{\Delta CD8}$ mice (**Figs. S7** and **S8**).

To functionally validate these changes, we performed Seahorse extracellular flux analysis using the XF Real-Time ATP Rate Assay on intratumoral CD8 T cells *ex vivo*. Bhlhe40-deficient CD8 T cells from anti-PD-1-treated $B^{\Delta CD8}$ mice exhibited significantly reduced ATP production from both glycolysis and mitochondrial OXPHOS (**Figs. 5C** and **5D**), consistent with broad impairment of energy metabolism. In contrast, CD8 T cells from anti-CTLA-4-treated $B^{\Delta CD8}$ mice showed a significant reduction in glycolytic ATP production while maintaining mitochondrial ATP production, indicating that under anti-CTLA-4, Bhlhe40 is selectively required for sustaining glycolytic output, whereas OXPHOS remains largely preserved. Together, these findings reveal that Bhlhe40 supports both glycolytic and mitochondrial energy production in CD8 T cells, but the relative metabolic dependency differs under distinct ICT regimens.

CD4 T Cell-Intrinsic Bhlhe40 Sustains Anti-CTLA-4-Driven Th1 Responses and Tumor Rejection

Compared to anti-PD-1, anti-CTLA-4 more profoundly affected conventional CD4 T helper cells (CD4 T cells) and regulatory T cells (Tregs) (**Figs. S13A** and **S13B**). These observations are consistent with our prior studies and those of others examining differential effects of anti-PD-1 versus anti-CTLA-4[20,21,29,41]. Whereas anti-PD-1 did not alter the frequency of CD4 T cells in either $B^{f/f}$ mice or $B^{\Delta CD8}$ mice, anti-CTLA-4 increased the frequency in both genotypes (**Fig. S13A**). Further, anti-CTLA-4 reduced Tregs[67], an effect that was independent of Bhlhe40 expression in CD8 T cells (**Fig. S13A)**. Our scRNAseq analysis revealed 5 clusters of

predominantly Tregs and 5 clusters of conventional CD4 T cells **(Fig. 6A)**. Anti-CTLA-4 drove a decrease in several Treg containing clusters (including the largest clusters such as Treg_1 and Cycling_Treg_2) **(Fig. S13B)** and this decrease was largely independent of Bhlhe40 in CD4 or CD8 T cells, since it occurred in $B^{f/f,}$ $B^{\Delta T}$, and $B^{\Delta CD8}$ mice. We noted several clusters of T helper 1 (Th1) cells: ICOS$^{\mathbf{hi}}$Bhlhe40$^{\mathbf{hi}}$_Th1_6, ICOS^{+}Bhlhe40^{+}_Th1_7, and Gzmk^{+}_Th1_8. ICOS$^{\mathbf{hi}}$Bhlhe40$^{\mathbf{hi}}$_Th1_6 expressed the highest levels of *Bhlhe40, Tnf,* and *Ifng* among CD4 T cells, along with *Tbx21* (Tbet), *Icos*, and *Pdcd1* **(Figs. 6B, S13C,** and **S13D)**. Interestingly, this cluster also expressed *Bcl6*, indicating some transcriptional features of T follicular helper cells (Tfh) **(Fig. S13D)**. ICOS^{+}Bhlhe40^{+}_Th1_7 also express high *Bhlhe40*, *Ifng*, *Tbx21*, *Icos,* and *Pdcd1* (**Figs. 6B, S13C,** and **S13D**). Gzmk^{+}_Th1_8 express Th1 markers (e.g., *Tbx21*, *Ifng*) but also displayed high expression of *Gzmk*, along with moderate expression of *Tcf7* and *Slamf6* **(Fig. S13D)**. Comparative analysis with published datasets[45,68] indicated that these Th1 subsets share transcriptional features with cytotoxic or highly activated effector populations in human cancer (**Fig. 6C**).

As expected[20,41,69-71], anti-CTLA-4 promoted expansion of ICOS$^{\mathbf{hi}}$Bhlhe40$^{\mathbf{hi}}$_Th1_6 and ICOS^{+}Bhlhe40^{+}_Th1_7 **(Figs. 6D** and **S13B)**. These Th1 populations expanded not only in $B^{f/f}$ and $B^{\Delta CD8}$ mice, but also in $B^{\Delta T}$ mice, although the magnitude of expansion varied by genotype. Despite this expansion, several transcriptomic alterations were observed in mice with disrupted Bhlhe40 expression in both CD8 and CD4 T cells ($B^{\Delta T}$ mice) **(Figs. S13C** and **S13D)**. Notably, when comparing *Ifng* expression within CD4 T cells across treatments and knockout conditions, two important patterns emerged. First, anti-CTLA-4 induced a higher frequency of Th1 CD4 T cells expressing elevated levels of *Ifng* compared to anti-PD-1, and this increase was observed in both $B^{f/f}$ and $B^{\Delta CD8}$ mice—treatment settings in which anti-CTLA-4-driven tumor rejection occurs (**Figs. 2B, 6D, 6E, S13C,** and **S13D**). Second, in the absence of Bhlhe40 in CD4 T cells ($B^{\Delta T}$ mice), *Ifng* expression was markedly reduced under all treatment conditions, including anti-CTLA-

4, and in these mice, the efficacy of anti-CTLA-4 (as well as anti-PD-1) was lost (**Figs. 2B, 6D, 6E, S13C,** and **S13D**).

Interestingly, we observed a modestly decreased expression of glycolytic transcripts in CD4 effector T cells from $B^{\Delta CD8}$ mice (**Fig. 6F**). In contrast, CD4 T cells from $B^{\Delta T}$ mice, lacking Bhlhe40 in both CD4 and CD8 T cells, displayed striking reductions in glycolytic transcript expression compared to $B^{f/f}$ mice, including in anti-CTLA-4-treated conditions. These findings suggest that CD8 T cell–intrinsic Bhlhe40 contributes indirectly to maintaining glycolytic transcript expression in CD4 effector T cells, whereas loss of Bhlhe40 across all T cell compartments leads to a more profound defects in metabolic transcript expression.

T Cell-Intrinsic Bhlhe40 Coordinates CD4 and CD8 T Cell-Dependent Macrophage Remodeling Following Immune Checkpoint Therapy

We previously demonstrated that anti-PD-1 and anti-CTLA-4 promotes intratumoral macrophage remodeling, shifting from $CX3CR1^+$ macrophages to $iNOS^+$ macrophages, with the induction of $iNOS^+$ macrophages being dependent on ICT-induced IFN-γ production by CD4 and CD8 T cells[21,41,72]. These $CX3CR1^+$ macrophages likely constitute a large fraction of what has historically been referred to as 'M2-like' tumor-associated macrophages, often co-expressing CD206, C1q, ApoE, TREM2, etc., though they are described using somewhat different marker sets across studies[14,19-21], whereas $iNOS^+$ macrophages are consistent with inflammatory M1-like macrophages. Here, we identified by scRNAseq multiple monocyte/macrophage clusters, including $CX3CR1^+$ macrophage clusters expressing *Cx3cr1, Mrc1* (CD206), *Fcrls*, and *Stab1*, as well as distinct clusters expressing *Nos2* (iNOS) (**Fig. 7A**). Both scRNAseq and flow cytometry revealed a marked impairment in ICT-driven macrophage remodeling in $B^{\Delta CD8}$ mice, and an even more pronounced defect in $B^{\Delta T}$ mice lacking Bhlhe40 in both CD4 and CD8 T cells (**Figs. 7B-7D**). Whereas anti-PD-1 or anti-CTLA-4 reduced the frequency of $CX3CR1^+$ macrophages in $B^{f/f}$

mice, this reduction was absent in $B^{\Delta CD8}$ and $B^{\Delta T}$ mice, which instead exhibited elevated frequencies of CX3CR1$^+$ macrophages under both control Ab and ICT conditions (**Figs. 7C** and **7D**). This was also reflected by transcript expression of markers enriched on pro-tumoral macrophages (**Fig. 7B**), including the TREM2 receptor, which we and others have shown is target on immunosuppressive macrophages[41,73,74]. Anti-PD-1 and especially anti-CTLA-4 expanded iNOS$^+$ macrophages in $B^{f/f}$ mice, whereas the frequency of iNOS$^+$ macrophages was severely reduced in $B^{\Delta CD8}$ mice, with an even greater reduction occurring in $B^{\Delta T}$ mice (**Fig. 7D**). The more pronounced defects in macrophage remodeling observed in $B^{\Delta T}$ mice relative to $B^{\Delta CD8}$ mice closely mirrored our prior findings in *Bhlhe40*$^{-/-}$ mice[29]. These findings indicate that Bhlhe40 expression in CD8 T cells, and more critically, in both CD4 and CD8 T cells, is required for effective ICT-induced macrophage remodeling, linking T cell-intrinsic Bhlhe40 to the shift from immunosuppressive CX3CR1$^+$ macrophages to proinflammatory iNOS$^+$ macrophages within the TME. Notably, they also reveal that despite incomplete macrophage remodeling, anti-CTLA-4 can still mediate tumor rejection, as observed in $B^{\Delta CD8}$ mice, suggesting that partial remodeling may be sufficient when CD4 T cell function is intact.

DISCUSSION:

Our study identifies Bhlhe40 as a transcriptional coordinator with distinct, therapy-specific requirements in CD4 and CD8 T cells during ICT. We demonstrate that anti-PD-1 efficacy requires CD8 T cell-intrinsic Bhlhe40 and may also rely on its expression in CD4 T cells, whereas anti-CTLA-4 efficacy is largely dependent on CD4 T cell-intrinsic Bhlhe40 and remains largely intact in the absence of Bhlhe40 in CD8 T cells. These findings establish that the contribution of Bhlhe40 to ICT responses is not uniform across T cell subsets or therapeutic modalities, but instead reflects differential mechanisms engaged by anti-PD-1 versus anti-CTLA-4. Notably, even under anti-CTLA-4 treatment, loss of Bhlhe40 alters tumor immune remodeling, although to less of an extent

as anti-PD-1, yet tumor rejection still occurs, suggesting that anti-CTLA-4 can overcome these deficiencies through dominant CD4 T cell-mediated mechanisms.

Mechanistically, Bhlhe40 promotes the acquisition of effector and exhausted CD8 T cell states and is required to sustain IFN-γ production and expression of effector/exhaustion markers (e.g., PD-1, LAG-3, etc.), while supporting both glycolytic and mitochondrial programs. Loss of Bhlhe40 skews CD8 T cells toward a more naïve or progenitor-like state with elevated TCF-1 and reduced acquisition of terminal effector features, particularly in the absence of ICT. These defects are most pronounced during anti-PD-1 therapy, where CD8 T cell-intrinsic Bhlhe40 appears critical for maintaining metabolic and transcriptional programs needed for durable effector function. Consistent with these findings, Wu et al.[75] recently demonstrated using in vitro chronic stimulation and chronic infection models that Bhlhe40 regulates the differentiation checkpoint between progenitor and intermediate exhausted CD8 T cells. Together, these data highlight a conserved role for Bhlhe40 in coordinating effector programming, metabolic fitness, and effector and exhaustion trajectories in CD8 T cells that are particularly essential for anti-PD-1 efficacy.

We and others previously showed that anti-PD-1 and anti-CTLA-4 each utilize both shared as well as distinct mechanisms[20,21,41]. Anti-PD-1 predominantly expands and sustains effector function from a TCF-1$^+$ progenitor (Tpex) NeoAg-specific CD8 pool, whereas anti-CTLA-4, directly and via CD4 T cell help enhances NeoAg-specific CD8 T cell priming/expansion with more memory-like and less terminally exhausted features (increased TCF-1 and decreased TOX)[11,20,21,58,60,76,77]. These therapies also differ in their capacity to induce memory responses: anti-CTLA-4 generates stronger memory through enhanced expansion, cytokine production, and antitumor activity compared to anti-PD-1, in part by restoring TCF-1$^+$ T cells during priming[62]. In contrast, anti-PD-1 treatment favors the accumulation of TOX$^+$ T cells. These distinctions, together with our findings and those of Wu et al.[75], suggest a basis for why CD8 T cells exhibit differential requirements for Bhlhe40 during anti-PD-1 versus anti-CTLA-4 therapy. Whereas anti-PD-1 efficacy appears to

depend on Bhlhe40 to sustain the transition of progenitor CD8 T cells into metabolically fit effector and exhausted states, anti-CTLA-4 may rely less on CD8-intrinsic Bhlhe40, instead driving CD4 T cell-mediated support and promoting the expansion of CD8 T cells with more memory-like or less terminally exhausted features.

Interestingly, tumor rejection was maintained during anti-CTLA-4 treatment even in the absence of CD8 T cell–intrinsic Bhlhe40, despite phenotypic and functional alterations such as reduced CD8-derived IFN-γ. This observation suggests that the therapeutic efficacy of anti-CTLA-4 is less dependent on CD8 T cell-intrinsic Bhlhe40, potentially due to compensatory mechanisms involving CD4 T cells. Further, we recently found[41] that anti-CTLA-4 robustly expands Th1-like ICOS^{+} CD4 T cell populations[20,70] that highly express Bhlhe40 and produce high levels of IFN-γ and likely contribute to myeloid remodeling and tumor control in settings where CD8 function is compromised. In contrast, in mice lacking Bhlhe40 in both CD4 and CD8 T cells, responses to both ICT modalities were abrogated, highlighting the cooperative roles of these subsets in orchestrating anti-tumor immunity.

Importantly, the phenotypic and functional impairments observed in CD8 T cells lacking Bhlhe40, including reduced IFN-γ production, were accompanied by defects in ICT-driven remodeling of the tumor myeloid compartment. Loss of CD8 T cell-intrinsic Bhlhe40 limited the shift from CX3CR1^{+} macrophages to pro-inflammatory iNOS^{+} macrophages, with a more severe impact on anti-PD-1 than anti-CTLA-4 therapy. Nevertheless, anti-CTLA-4 still promoted greater macrophage reprogramming, and ultimately tumor rejection, under these conditions, likely reflecting compensatory contributions from CD4 T cells. This defect was even more pronounced when Bhlhe40 was absent from both CD4 and CD8 T cells, highlighting the cooperative requirement of both subsets for ICT-driven macrophage remodeling. Notably, the relatively greater macrophage remodeling observed with anti-CTLA-4 in CD8 Bhlhe40-deficient mice may in part

reflect CD4-derived IFN-γ and Th1-like help, whereas combined loss of Bhlhe40 in both CD4 and CD8 T cells crippled macrophage remodeling even under anti-CTLA-4 therapy. While IFN-γ is a pivotal driver of pro-inflammatory macrophage phenotypes, additional Bhlhe40-dependent changes in T cells—such as altered production of TNFα and changes to metabolic fitness may also contribute to the extent and quality of macrophage remodeling

Our data also link Bhlhe40 to metabolic programming in a partially therapy-dependent manner. Under anti-PD-1 treatment, Bhlhe40-deficient CD8 T cells exhibited marked reductions in both glycolytic and OXPHOS capacity, with the latter consistent with prior work implicating Bhlhe40 in sustaining mitochondrial fitness under anti-PD-1 treatment conditions[26]. These metabolic alterations may reflect direct, cell-intrinsic roles of Bhlhe40, but could also be secondary to shifts in cell state in its absence, as effector populations are known to exhibit higher glycolytic activity[78]. Under anti-CTLA-4 treatment, Bhlhe40-deficient CD8 T cells also showed reduced glycolytic activity but maintained OXPHOS, highlighting distinct metabolic alterations associated with each therapy. Interestingly, loss of Bhlhe40 in CD8 T cells also impaired glycolytic programming in CD4 effector T cells, likely reflecting alterations in CD8 T cells that either directly influence CD4 T cells or reshape the TME in ways that secondarily impact CD4 T cell metabolism. In addition, tumor-intrinsic metabolism may further constrain T cell glycolysis, as progressing tumors deplete glucose and release lactate, thereby acidifying the TME[79]. Notably, in $B^{\Delta T}$ mice lacking Bhlhe40 in both CD4 and CD8 T cells, glycolytic transcript expression in CD4 T cells was dramatically reduced across treatment conditions, including under anti-CTLA-4. These findings suggest that CD8-intrinsic Bhlhe40 may indirectly support CD4 metabolic fitness, whereas CD4-intrinsic Bhlhe40 may directly and indirectly sustain glycolytic capacity in CD4 T cells. Overall, both intrinsic regulation by Bhlhe40 and extrinsic cues from the TME likely shape the metabolic fitness of both CD4 and CD8 T cells in a therapy-dependent manner.

These observations align with the well-established requirement for robust glycolytic and mitochondrial programs to support effector cytokine production, cytotoxicity, and persistence of T cells in the TME. In particular, glycolysis has been linked to rapid effector responses, while mitochondrial fitness supports sustained function and long-term survival under conditions of chronic stimulation[78-81]. Thus, the combined impairment of both pathways in Bhlhe40-deficient CD8 T cells, together with diminished CD4 glycolytic capacity under PD-1 blockade, may compromise the ability of T cells to maintain effector activity. By contrast, preserved mitochondrial function in CD8 T cells, along with robust CD4-intrinsic glycolytic programming supported by TME signals, may allow for partial compensation during anti-CTLA-4 therapy. Together, these findings suggest that transcriptional control of metabolic fitness by Bhlhe40 intersects with distinct immune programs engaged by anti-PD-1 versus anti-CTLA-4, and may help explain therapy-specific differences in how T cell subsets contribute to anti-tumor responses. Given the requirement for T cells to upregulate glycolysis upon effector differentiation, it is notable that signals downstream of TCR activation and costimulation, which drive metabolic reprogramming, also can induce Bhlhe40 expression, placing Bhlhe40 at the interface between activation-induced metabolic enhancement and effector programming.

Analysis of human cancer datasets revealed that BHLHE40 is enriched in tumor-reactive and activated/exhausted CD8 T cells across multiple tumor types, inversely correlated with *TCF7*, and positively associated with *TOX* and *IFNG*. Moreover, subsets of CD8 T cells expressed higher levels of BHLHE40 in basal and squamous cell carcinoma responders compared with non-responders. This conserved transcriptional signature reinforces the relevance of our murine findings to human ICT responses and suggests that Bhlhe40 expression could serve as a biomarker for T cell differentiation state and functional competence in the TME.

Collectively, our findings position Bhlhe40 as a subset- and therapy-specific regulator of ICT responses, integrating effector programming, metabolic fitness, and myeloid remodeling. From a translational perspective, these results suggest that strategies to sustain or enhance Bhlhe40 activity—particularly in CD8 T cells during PD-1 blockade—may improve therapeutic efficacy. Conversely, understanding how CD4 T cells compensate for CD8 deficits under anti-CTLA-4 may inform combinatorial approaches that exploit these complementary mechanisms. Further studies dissecting the upstream signals and epigenetic circuits controlling Bhlhe40 expression will be critical for developing interventions that selectively reinforce its beneficial functions in anti-tumor immunity.

MATERIALS AND METHODS:

Mice

All mice used were on a C57BL/6 background. Wild type C57BL/6J, *CD4-Cre* (B6.Cg-Tg(Cd4-cre)1Cwi/BfluJ)[36]: JAX stock #022071, *CD8 E8I-Cre* (B6.Tg(Cd8a-cre)1Itan/J)[37]: JAX stock #008766 mice were purchased from Jackson Labs. All *in vivo* experiments used 8–12-week-old female or male (to match the sex and strain of the tumors), all mice were housed in our specific pathogen-free animal facility. *Bhlhe40*$^{f/f}$ mice have been previously reported[23,24,29,82]. For experiments using conditional Bhlhe40 KO mice, *Bhlhe40*$^{f/f}$ littermates or *CD8 E8I-Cre Bhlhe40*$^{+/+}$ mice were used as controls. All studies were performed in accordance with procedures approved by the AAALAC accredited Animal Studies Committee of The University of Texas MD Anderson Cancer Center.

Tumor lines

MCA-induced sarcomas used in this study were generated in female C57BL/6 strain wild type (1956) mice and were banked as low-passage tumor cells as previously described[83] and were obtained from Robert Schreiber (Washington University in St. Louis School of Medicine). Y1.7LI is a melanoma line derived from the Braf^{V600E} Cdkn2a$^{-/-}$ Pten$^{-/-}$ YUMM1.7 line[40] engineered to

express mLama4, an H2-K^b-restricted MHC class I neoantigen, and mItgb1, an I-A^b-restricted MHC class II neoantigen, as previously described[41]. Tumor lines are tested yearly and at last assessment were found to be free of non-mouse cells as assessed by mouse cell STR profiling of common mouse pathogens and mycoplasma as assessed by IDEXX IMPACT™ I mouse pathogen testing (PCR evaluation for: Corynebacterium bovis, Corynebacterium sp. (HAC2), Ectromelia, EDIM, Hantaan, K virus, LCMV, LDEV, MAV1, MAV2, mCMV, MHV, MNV, MPV, MTV, MVM, Mycoplasma pulmonis, Mycoplasma sp., Polyoma, PVM, REO3, Sendai, TMEV). Tumor lines from the same cryopreserved stocks that were used in this study tested negative for mycoplasma and were authenticated and found to be free of non-mouse cells as assessed by mouse cell STR profiling in December 2021 (IDEXX CellCheck™ mouse 19 plus *Mycoplasma* spp. testing).

Tumor transplantation

1956 MCA sarcoma line and Y1.7LI melanoma cells were from frozen stocks and propagated in R-10 plus BME media [RPMI media (Hyclone) supplemented with 1% L-glutamine, 1% penicillin-streptomycin, 1% Na Pyruvate, 0.5% Na Bicarbonate, 0.1% 2-Mercaptoethanol, and 10% FCS (Hyclone)]. Upon thawing, tumor lines were passaged 3-5 times before experimental use. Prior to injection, cells were washed extensively, resuspended at a concentration of 6.67 x 10^6 cells per ml in endotoxin-free PBS for 1956 and at a concentration of 3.33 x 10^6 cells per ml in endotoxin-free PBS for Y1.7LI and then 150 µl (1 x 10^6 cells per mouse for 1956 and 0.5 x 10^6 cells per mouse for Y1.7LI) injected subcutaneously into the flanks of recipient mice. Tumor cells were >90% viable at the time of injection as assessed by trypan blue exclusion. Tumor growth was quantified by caliper measurements and expressed as the average of two perpendicular diameters.

Tetramer staining

Mutant Psmd6-H-2K^b-PE tetramers (IAPYYEAL) were obtained from the Baylor College of Medicine MHC Tetramer Production Facility. Cells were incubated at room temperature for 5 minutes with 500ng of rat anti-mouse anti-CD16/32 (mouse Fc block; clone 2.4G2, BD

Biosciences) at 1µg/million cells. H-2K^b-PE tetramers conjugated with PE for mutated Psmd6 were added to the cells and incubated for 20 minutes at 37°C. Cells were further stained with an antibody mixture cocktail with anti-PD-1, anti-TIM-3, anti-LAG3 antibodies and live/dead (Zombie NIR) in 100µl FACS buffer for 20 minutes at 4°C.

Immune checkpoint therapy

Mice were treated intraperitoneally with 200 µg of anti-PD-1 or anti-CTLA-4 on days 3, 6, 9 post-tumor transplant for 1956 and on days 7, 10, 13, 16, and 21 for Y1.7LI. For controls, mice were injected with 200 µg of isotype control antibodies.

***In Vivo* antibodies**

Anti-PD-1 (rat IgG2a clone RMP1-14) and anti-CTLA-4 (murine IgG2b clone 9D9) immune checkpoint antibodies were purchased from Leinco Technologies. Isotype control antibodies (rat IgG2a clone 1-1, mouse IgG2a clone OKT3, and rat IgG2b clone 1-2) were purchased from Leinco Technologies. All *in vivo* antibodies purchased from Leinco were "*In vivo* Platinum"-grade and were verified free of mouse pathogens (IDEXX IMPACT^{TM} I mouse pathogen testing).

Tumor harvest

Established tumors were isolated from mice, minced and treated with 1 mg/ml type IA collagenase (Sigma) in HBSS (Hyclone) for 45 minutes at 37 °C. Cells were washed thrice. Red blood cells were lysed using ACK lysis buffer (Gibco). To remove aggregates and clumps, cells were passed through a 40-micron strainer.

Quantitative RT-PCR

RNA was extracted from sorted T cells using RNAeasy Plus Mini Kit (Qiagen). 100 µg of RNA was reverse-transcribed and subjected to qPCR using the SuperScript III Platinum Two-Step qRT-PCR Kit with SYBR Green (Invitrogen). qPCR was performed on the StepOne Real-Time PCR System (Applied Biosystems). Each sample was run in triplicate for each gene and the cDNA from each sample was divided equally per reaction in a 20 µl volume. The qPCR conditions were as follows: 50°C for 2 minutes and 95°C for 2 minutes, followed by 40 cycles of 95°C for 15 seconds

and 60°C for 30 seconds. Melting curve analysis was performed to confirm a single amplicon. Differences in gene expression were determined using the equation $2^{-\Delta\Delta Ct}$, where the Ct value for *Bhlhe40* was subtracted from the Ct value of the *Gapdh* control to yield the ΔCt value. For each sample, the ΔCt value *Bhlhe40* done in triplicate was averaged and compared to give one ΔΔCt value per sample. Mouse quantitative RT-PCR primers for *Bhlhe40* were as follows: forward primer-5' ACGGAGACCTGTCAGGGATG3' and reverse primer-5'GGCAGTTTGTAAGTTTCCTTGC3'. Mouse quantitative RT-PCR primers for *Gapdh* were as follows: forward primer-5'AGGTCGGTGTGAACGGATTTG3' and reverse primer-5'TGTAGACCATGTAGTTGAGGTCA3'.

Single-cell RNA Sequencing

Antibody hashing for multiplexing and single-cell RNA sequencing library preparation

Antibody hashing and multiplexing was utilized for scRNAseq. For the scRNAseq Experiment #1 and Experiment #2, cell labeling was performed according to an adapted BioLegend cell hashing protocol (TotalSeq™-C Antibodies and Cell Hashing with 10x Single Cell 5' Reagent Kit v1.1 Protocol, BioLegend). Single cell suspensions of harvested tumors from treated mice of different groups were resuspended in BioLegend Cell Staining Buffer containing Fc block and then surface stained with an antibody master mix consisting of anti-CD45.2/PE, anti-CD90.2/Thy1.2-PE-Cy7, and live/dead dye (NIR) and then barcoded antibodies with unique hashtags were added according to Supplement Table 1. Hashtag antibodies were used at a concentration of 1 μg per 2 million cells. Cells were then washed 3X with BioLegend Cell Staining Buffer and pooled for single-cell library generation and CITE-seq (cellular indexing of transcriptomes and epitopes by sequencing) through multiplexing. Cells were counted on a Countess 3 FL automated cell counter (Life Technologies) and viabilities were determined using trypan blue exclusion assay. Cell capture processing and gene expression and feature barcode library preparations were performed following 10X Genomics' guidelines for 5' scRNAseq by encapsulating sorted live $CD45^+$ tumor infiltrating cells [CG000330_Chromium Next GEM Single Cell 5' v2 (Dual Index) with Feature Barcode

technology-Rev F]. QC steps after cDNA amplification and library preparation steps were carried out by running ThermoFisher Qubit HS dsDNA Assay along with Agilent (Santa Clara, CA) HS DNA Bioanalyzer for concentration and quality assessments, respectively. Library sample concentrations were verified using qPCR using a KAPA Biosystems KAPA Library Quantification Kit prior to pooling. Libraries were normalized to 5 nM for pooling. The pool was sequenced using a NovaSeq6000 S4-XP, 200-cycle flow cell lane. The run parameters used were 26 cycles for read 1, 90 cycles for read2, 10 cycles for index1, and 10 cycles for index2 as stipulated in the protocol mentioned above.

Single-cell RNA sequencing alignment, barcode assignment, and UMI Counting

The Cell Ranger Single-Cell Software Suite available at https://support.10xgenomics.com/single-cell-gene-expression/software/overview/welcome was used to perform sample demultiplexing, barcode processing and single-cell 5' counting. "Cellranger mkfastq" was used to demultiplex raw base call files from the NovaSeq6000 sequencer, into sample-specific fastq files. Files were demultiplexed with 81.9% to 97.1% perfect barcode match, and 90%+ q30 reads. Afterward, fastq files for each sample were processed with "Cellranger count", which was used to align samples to mm10 genome, filter and quantify. For each sample the recovered-cells parameter was specified as 10,000 cells that we expected to recover for each individual library.

Preprocessing analysis with Seurat package

The Seurat pipeline was applied to each dataset following tutorial specifications from [https://satijalab.org/seurat/articles/archive; version 3.2] and [https://hbctraining.github.io/scRNA-seq_online/]. QC process was performed for each experiment and group separately. Genes that were expressed in less than 3 cells and cells that contained less than 500 transcripts (UMI's), or had less than 250 and more than 6500 genes, or more than 10% of mitochondrial transcripts, were excluded. Data were normalized using LogNormalize method. Potential doublets were removed by using scDblFinder package (1.16.0). For generating integrated CD8 T cell object, we used gene expression: *Cd3e* > *0*, *Cd8a* > 0 & *Cd4*

= 0, similar for generating CD4 T cell object we used: *Cd3e > 0, Cd4* > 0 & *Cd8a* = 0. All Cd8 and Cd4 data from all groups and experiments were integrated into a single CD8 or CD4 Seurat object. Expression matrix from all group were integrated using batch effect correction algorithm implemented in the Seurat V5 pipeline, employing anchor-based reciprocal principal component analysis (RPCA). Briefly, repeatedly variable genes across groups were selected by using 'SelectIntegrationFeatures' function. ScaleData and RunPCA were performed using these genes. Next, anchors were identified with 'FindIntegrationAnchors' and integration was performed using these anchors through 'IntegrateData'. Unsupervised graph-based clustering was then performed on the integrated dataset. A UMAP dimensional reduction was performed on the scaled matrix (with most variable genes only) using first 40 PCA for CD8 and 50 PCA for CD4 components to obtain a two-dimensional representation of the cell states. For clustering, we used the function FindClusters that implements SNN (shared nearest neighbor) modularity optimization-based clustering algorithm.

Identification of cluster-specific genes and marker-based classification

To identify marker genes, the FindAllMarkers function was used with likelihood-ratio test for single cell gene expression. For heatmap representation, average expression of markers inside each cluster was used. To compare gene expression for the clusters inside cohorts (e.g., T cells, macrophages) we used FindMarkers function to calculate average log2 fold change and identify differentially expressed genes between each pair of experimental conditions using a Wilcoxon Rank-Sum test for calculating p-values and Bonferroni correction for adjusted p-values. Gene set enrichment analysis was performed using the fgsea package (version 1.32.0) to assess the enrichment of Hallmark gene sets from the Molecular Signatures Database (MSigDB). Hallmark gene sets were obtained using the msigdbr package (version 7.5.1). Differential gene expression analysis was performed using the FindMarkers function in Seurat (version 5.1.0) with the following parameters: threshold of log2 fold change = 0.2, and minimum percentage of expression

= 0.1. Genes were ranked according to their log2 fold change, and these rankings were used as input for the enrichment analysis using the fgsea package.

Comparison to published datasets

The gene lists defining phenotype of intratumoral T cells were retrieved from published human or mouse scRNAseq datasets[44,84,45,34,42,68](**Tables S2-S5**) to compare the cluster annotation between published study and our current study. The module scores for individual cells were calculated using the "AddModuleScore" function in the Seurat package. The results were visualized using the normalized average module scores for each cluster (**Figs. 3F and S12A**).

Analysis of human datasets

The human scRNAseq data were collected from previously published datasets. Read count matrix was downloaded and metadata generated in Yost et al manuscript[33] (GSE123813). For Bassez et al[85] read count matrix and metadata are downloaded through VIB-Ku LEUVEN center for cancer biology (https://lambrechtslab.sites.vib.be/en/single-cell). Read count matrix from Sade-Feldman et al.[42] dataset was downloaded through GSE120575. Seurat objects then were generated and processed with Seurat pipeline. Seurat object of CD8 T cells in the paper from Minowa et al.[86] were download from Zenodo (https://doi.org/10.5281/zenodo.12761836). For volcano plot from Oliveira et al[34], DEG list provided in the Oliveira et al. paper were used. For volcano plot from Minowa et al, DEGs were identified by using FindMarkers function. For cell-type specific co-expression, inference from scRNAseq data, CS-CORE package was utilized to create the co-expression heatmap[87].

Ex Vivo T Cell Stimulation

For PMA/ionomycin T cell stimulation, cells from tumors were enriched for CD8 T cells using Miltenyi mouse $CD8^+$ T cell enrichment from TIL kit by following manufacturer's protocol. Cells were then incubated with 10 ng/ml of PMA and 1 μg/ml of ionomycin in the presence of BD GolgiPlug (BD Bioscience) for 6 hours at 37 °C. and stained for IFN-γ and TNFα.

For longitudinal monitoring of *Bhlhe40* expression in TCR transgenic CD4 and CD8 splenic T cells upon antigen-specific activation, CD8 T cells from spleens of naive 8-week-old female OT-I mice and $CD4^+$ T cells from spleens of naive 8-week-old female OT-II mice were enriched using Miltenyi mouse $CD4^+$ enrichment kit and mouse $CD8^+$ T cell enrichment kit by following manufacturer's protocol. Splenocytes from naive 8-week-old female C57BL/6J mice were pulsed for 2 hours at 37 °C with 1 μM of OVA-I-SIINFEKL or OVA-II (ISQAVHAAHAEINEAGR) peptide and then washed twice with R10 + BME media. Enriched $CD8^+$ OT-I or $CD4^+$ OT-II T cells were co-cultured with OVA-I-SIINFEKL or OVA-II-pulsed splenocytes, respectively. Individual wells were harvested at 24, 48, 72, and 96 hours post-stimulation for mRNA analysis.

Tetramer staining

Mutant Psmd6-H-$2K^b$-PE tetramers (IAPYYEAL) were obtained from the Baylor College of Medicine MHC Tetramer Production Facility. Cells were incubated at room temperature for 5 minutes with 500ng of rat anti-mouse anti-CD16/32 (mouse Fc block; clone 2.4G2, BD Biosciences) at 1μg/million cells. Peptide-H-$2K^b$ tetramers conjugated with PE for mutated Psmd6 (1:500 dilution) were added to the cells and incubated for 20 minutes at 37°C. Cells were further stained with an antibody mixture cocktail: anti-mouse CD45 BV605 (clone 30-F11) BioLegend (1:800 dilution), anti-mouse Thy1.2-PECy7 (clone 30-H12) BioLegend (1:500 dilution), anti-mouse CD4-BV711 (clone RM4-5) (1:200 dilution) BioLegend, anti-mouse CD8a-BV786 (clone 53-6.7) BioLegend (1:200 dilution), and live/dead (Zombie NIR) in 100μl FACS buffer for 20 minutes at 4°C.

Flow cytometry

For flow cytometry, cells were stained for 5 minutes at room temperature with Fc block (anti-CD16/32) clone 2.4G2 (BD Bioscience) at 1 μg/million cells and then surfaced stained for 20 minutes at 4 °C. Surface antibodies were diluted in FACS staining buffer (PBS with 2% FCS, 2 mM EDTA, and 0.05% NaN_3 (Sigma)). Anti-mouse CD45 BV605 (clone 30-F11) BioLegend (1:800 dilution), anti-mouse CD3e-APC (clone 145-2C11) BioLegend (1:200 dilution), anti-

mouse CD4-BV711 (clone RM4-5) (1:200 dilution) BioLegend, anti-mouse CD8a-BV786 (clone 53-6.7) BioLegend (1:200 dilution), anti-mouse CX3CR1-FITC (clone SA011F11) BioLegend (1:1000), anti-mouse I-A/I-E-BV650 (clone M5/114.15.2) BioLegend (1:3000 dilution), anti-mouse CD24-BV711 (clone M1/69) BD Bioscience, anti-mouse CD11c-BV786 (clone HL3) BD Bioscience (1:400 dilution), anti-mouse F4/80-BUV395 (clone T45-2342) BD Bioscience (1:400 dilution), anti-mouse CD64-BV421 (clone X54-5/7.1) BioLegend (1:400 dilution), anti-mouse Ly6G-Alexa Fluor 700 (clone 1A8) BD Bioscience (1:400 dilution), and anti-mouse CD11b-APC (clone M1/70) BioLegend (1:400 dilution) were used for surface stain at indicated dilutions. Zombie NIR Viability dye (BioLegend) was added at 1:500 during surface stain. For intracellular staining, surface stained cells were fixed and permeabilized with BD fixation and permeabilization kit (BD Biosciences). Fixed and permeabilized cells were then stained with anti-mouse Mrc1 (CD206)-APC-Cy7 (clone C068C2) BioLegend (1:400 dilution) and anti-mouse iNOS/Nos2-PE (clone CXNFT) Thermo Fisher (1:400 dilution) for 30 minutes at 4 °C. For intracellular cytokine staining of lymphocytes, cells were isolated and then incubated at 37 °C for 6 hours with GolgiStop (BD Bioscience). Cells were then harvested, washed, stained for 5 minutes at room temperature with Fc block (anti-CD16/32) clone 2.4G2 (BD Bioscience) at 1 μg/million cells and then surfaced stained for 20 minutes at 4°C, and then fixed and permeabilized with BD fixation and permeabilization kit (BD Biosciences). Fixed and permeabilized cells were then stained with anti-IFN-γ-APC (XMG1.2) BioLegend (1:200 dilution) and anti-TNF-α-PE-Cy7 (clone MP6-XT22) BioLegend (1:200 dilution) for 30 minutes at 4°C.

Fluorescence-activated cell sorting

For sorting of CD8/CD4 T cells and CD45.2^{+}Thy1.2^{+} cells, intratumoral cells were stained for 5 minutes at room temperature with Fc block (anti-CD16/32) clone 2.4G2 (BD Bioscience) at 1 μg/million cells and then were stained with surface antibodies against CD45, CD90.2/Thy1.2, CD8a, and CD4 for CD4/CD8 sorting and with CD45.2-PE (clone 104) BioLegend (1:1000

dilution) and CD90.2/Thy1.2 for CD45.2$^+$Thy1.2$^+$ sorting along with Zombie NIR Viability dye and incubated for 30 minutes at 4°C. Cells were washed twice with MACS buffer and sorted gating on live CD45$^+$, CD90.2/Thy1.2$^+$, CD8a$^+$, CD4$^+$ or CD45.2$^+$,Thy1.2$^+$. Sorting was performed on a BD FACSAria II (BD Biosciences). CD8/CD4 sorted cells were processed for qPCR and CD45.2$^+$Thy1.2$^+$ sorted cells were processed for scRNA sequencing. The purity of the sorted cells for scRNA sequencing was greater than 97% as assessed during post-sort cellular analysis. All flow cytometry was performed on the LSR Fortessa X-20 (BD Biosciences) and analyzed using FlowJo software (TreeStar).

Magnetic associated cell sorting

Single cell suspension from tumors were resuspended in MACS buffer, along with 10 µl of CD8 (TIL) microbeads per 10^7 total cells and incubated for 15 minutes in 4ºC. After incubation, CD8 T cell fractions were isolated in a magnetic field using MACS separator according to the manufacturer's protocol. Isolated CD8 T cells were processed for Seahorse real-time ATP rate assay.

Seahorse XF Real-Time ATP Rate Assay

The Seahorse XF Real-Time ATP Rate Assay (Agilent, 103592-100) were performed on a Seahorse XFe96 Analyzer (Agilent) according to the manufacturer's protocol. Briefly, 1×10^5 cells/well were seeded in Seahorse XF RPMI-1640 medium (Agilent, 103576-100) supplemented with 1 mM pyruvate (103578-100), 10 mM glucose (103577-100), and 2 mM glutamine (103579-100) in a Cell-Tak–coated Seahorse XF96 cell culture microplate. Cells were centrifuged at 200 × g for 1 minute (no brake) and then incubated in a 37°C non-CO_2 incubator for 30 minutes to allow complete adherence. Pre-hydrated sensor cartridges were loaded with 1.5 µM oligomycin and 0.5 µM rotenone/antimycin, which were sequentially injected during the assay to measure oxygen consumption rate (OCR) and extracellular acidification rate (ECAR) in real time. Data were analyzed using Wave Software (Agilent, v2.6.3.5) to calculate ATP production rates derived from

mitochondrial oxidative phosphorylation (OXPHOS) and glycolysis, and values were normalized to seeded cell numbers.

Statistical analysis

Samples were compared using an unpaired, two-tailed Student's *t*-test, two-way ANOVA, or log-rank (Mantel-Cox) test unless specified otherwise.

Data and Software Availability

Data files for the scRNAseq data reported in this paper will be deposited in the Gene Expression Omnibus (GEO) database and made publicly available at the time of publication. Software used in this study is available online: current version of Cell Ranger: https://support.10xgenomics.com/single-cell-gene-expression/software/downloads/latest; Seurat 4.0: https://satijalab.org/seurat/; ggplot2 3.3.3: https://ggplot2.tidyverse.org/index.html; and ImmGen: https://www.immgen.org.

Author's Contributions

Conceptualization, A.S., T.M, A.S.S., and M.M.G.; data curation, A.S., T.M., A.S.S., A.J.S., S.K., and M.M.G.; investigation, A.S., T.M., A.S.S., S.K., N.N.J., and M.M.G.; visualization, A.S., T.M., A..S.S., S.K., M.M.G.; methodology, A.S., T.M., and M.M.G.; data analysis, A.S., T.M., A.S.S., N.N.J.; formal analysis, A.S., N.N.J., K.E.P., K.H.H., B.T.E., K.C., and M.M.G.; validation, A.S., and M.M.G.; writing – original draft, A.S., and M.M.G.; writing – review & editing, A.S., T.M., K.E.P., K.H.H., B.T.E., K.C., and M.M.G.; resources, B.T.E., K.C., and M.M.G.; supervision, M.M.G.; project administration, M.M.G.

Acknowledgments

M.M.G. was a Cancer Prevention and Research Institute of Texas (CPRIT) Scholar in Cancer Research and an Andrew Sabin Family Foundation Fellow during part of this study. This work was supported by CPRIT (Recruitment of First-Time Tenure-Track Faculty Members;

RR190017), an Andrew Sabin Family Foundation Fellowship, a Parker Institute for Cancer Immunotherapy (PICI) Bridge Scholar Award, a University of Texas (UT) Rising Stars Award, and NCI R01CA282027 to M.M.G. and NCI U01CA247760 to K.C. K.H.H. is a CPRIT Scholar in Cancer Research and a PICI and V Foundation Bridge Scholar. K.E.P. is an Andrew Sabin Family Foundation Fellow at MDACC and has been supported by the Melanoma SPORE Developmental Research Program at MDACC (grant P50CA221703 from NCI) and the Rising Stars Award. The MDACC Flow Cytometry and Cellular Imaging Core Facility and the Advanced Technology Genomics Core (ATGC) are supported by NCI Core grant P30CA016672. We would like to thank David Pollock at ATGC for assistance with scRNA-seq. We would like to thank X. Lily Wang at Baylor College of Medicine MHC Tetramer Core for production of tetramers used in this study. We would like to thank Waikin Chan at MDACC Metabolomics core for assistance with Real-time ATP assays.

Declaration of interests

M.M.G. reports a personal honorarium of US $1,000.00 per year from Springer Nature Ltd (as an associate editor for *Nature Precision Oncology*) and served as a paid consultant for Merck. KEP reports a patent on T cell exhaustion state-specific gene expression regulators and uses thereof (US2021/0309965 A1) that is unrelated to the current work.

REFERENCES:

1 Leach, D. R., Krummel, M. F. & Allison, J. P. Enhancement of antitumor immunity by CTLA-4 blockade. *Science* **271**, 1734-1736, doi:10.1126/science.271.5256.1734 (1996).

2 Kalbasi, A. & Ribas, A. Tumour-intrinsic resistance to immune checkpoint blockade. *Nat Rev Immunol* **20**, 25-39, doi:10.1038/s41577-019-0218-4 (2020).

3 Sharma, P. *et al.* The Next Decade of Immune Checkpoint Therapy. *Cancer Discov* **11**, 838-857, doi:10.1158/2159-8290.CD-20-1680 (2021).

4 Wolchok, J. D. *et al.* Long-Term Outcomes With Nivolumab Plus Ipilimumab or Nivolumab Alone Versus Ipilimumab in Patients With Advanced Melanoma. *J Clin Oncol* **40**, 127-137, doi:10.1200/JCO.21.02229 (2022).

5 Gubin, M. M. & Vesely, M. D. Cancer Immunoediting in the Era of Immuno-oncology. *Clin Cancer Res* **28**, 3917-3928, doi:10.1158/1078-0432.CCR-21-1804 (2022).

6 Sharma, P. *et al.* Immune checkpoint therapy-current perspectives and future directions. *Cell* **186**, 1652-1669, doi:10.1016/j.cell.2023.03.006 (2023).

7 Wolchok, J. D. *et al.* Final, 10-Year Outcomes with Nivolumab plus Ipilimumab in Advanced Melanoma. *N Engl J Med* **392**, 11-22, doi:10.1056/NEJMoa2407417 (2025).

8 Heemskerk, B., Kvistborg, P. & Schumacher, T. N. The cancer antigenome. *The EMBO journal* **32**, 194-203, doi:10.1038/emboj.2012.333 (2013).

9 van Rooij, N. *et al.* Tumor exome analysis reveals neoantigen-specific T-cell reactivity in an ipilimumab-responsive melanoma. *J Clin Oncol* **31**, e439-442, doi:10.1200/JCO.2012.47.7521 (2013).

10 Coulie, P. G., Van den Eynde, B. J., van der Bruggen, P. & Boon, T. Tumour antigens recognized by T lymphocytes: at the core of cancer immunotherapy. *Nat Rev Cancer* **14**, 135-146, doi:10.1038/nrc3670 (2014).

11 Gubin, M. M. *et al.* Checkpoint blockade cancer immunotherapy targets tumour-specific mutant antigens. *Nature* **515**, 577-581, doi:10.1038/nature13988 (2014).

12 Kreiter, S. *et al.* Mutant MHC class II epitopes drive therapeutic immune responses to cancer. *Nature* **520**, 692-696, doi:10.1038/nature14426 (2015).

13 Schumacher, T. N. & Schreiber, R. D. Neoantigens in cancer immunotherapy. *Science* **348**, 69-74, doi:10.1126/science.aaa4971 (2015).

14 Fehlings, M. *et al.* Checkpoint blockade immunotherapy reshapes the high-dimensional phenotypic heterogeneity of murine intratumoural neoantigen-specific CD8(+) T cells. *Nat Commun* **8**, 562, doi:10.1038/s41467-017-00627-z (2017).

15 Brightman, S. E., Naradikian, M. S., Miller, A. M. & Schoenberger, S. P. Harnessing neoantigen specific CD4 T cells for cancer immunotherapy. *J Leukoc Biol* **107**, 625-633, doi:10.1002/JLB.5RI0220-603RR (2020).

16 Cui, C. *et al.* Neoantigen-driven B cell and CD4 T follicular helper cell collaboration promotes anti-tumor CD8 T cell responses. *Cell* **184**, 6101-6118 e6113, doi:10.1016/j.cell.2021.11.007 (2021).

17 Chen, Z. *et al.* TCF-1-Centered Transcriptional Network Drives an Effector versus Exhausted CD8 T Cell-Fate Decision. *Immunity* **51**, 840-855 e845, doi:10.1016/j.immuni.2019.09.013 (2019).

18 Zheng, L. *et al.* Pan-cancer single-cell landscape of tumor-infiltrating T cells. *Science* **374**, abe6474, doi:10.1126/science.abe6474 (2021).

19 Caushi, J. X. *et al.* Transcriptional programs of neoantigen-specific TIL in anti-PD-1-treated lung cancers. *Nature* **596**, 126-132, doi:10.1038/s41586-021-03752-4 (2021).

20 Wei, S. C. *et al.* Distinct Cellular Mechanisms Underlie Anti-CTLA-4 and Anti-PD-1 Checkpoint Blockade. *Cell* **170**, 1120-1133 e1117, doi:10.1016/j.cell.2017.07.024 (2017).

21 Gubin, M. M. *et al.* High-Dimensional Analysis Delineates Myeloid and Lymphoid Compartment Remodeling during Successful Immune-Checkpoint Cancer Therapy. *Cell* **175**, 1014-1030 e1019, doi:10.1016/j.cell.2018.09.030 (2018).

22 Cook, M. E., Jarjour, N. N., Lin, C. C. & Edelson, B. T. Transcription Factor Bhlhe40 in Immunity and Autoimmunity. *Trends Immunol* **41**, 1023-1036, doi:10.1016/j.it.2020.09.002 (2020).

23 Lin, C. C. *et al.* Bhlhe40 controls cytokine production by T cells and is essential for pathogenicity in autoimmune neuroinflammation. *Nat Commun* **5**, 3551, doi:10.1038/ncomms4551 (2014).

24 Huynh, J. P. *et al.* Bhlhe40 is an essential repressor of IL-10 during Mycobacterium tuberculosis infection. *J Exp Med* **215**, 1823-1838, doi:10.1084/jem.20171704 (2018).

25 Kanda, M. *et al.* Transcriptional regulator Bhlhe40 works as a cofactor of T-bet in the regulation of IFN-gamma production in iNKT cells. *Proc Natl Acad Sci U S A* **113**, E3394-3402, doi:10.1073/pnas.1604178113 (2016).

26 Li, C. *et al.* The Transcription Factor Bhlhe40 Programs Mitochondrial Regulation of Resident CD8(+) T Cell Fitness and Functionality. *Immunity* **52**, 201-202, doi:10.1016/j.immuni.2019.12.008 (2020).

27 Lin, C. C. *et al.* IL-1-induced Bhlhe40 identifies pathogenic T helper cells in a model of autoimmune neuroinflammation. *J Exp Med* **213**, 251-271, doi:10.1084/jem.20150568 (2016).

28 Uyeda, M. J. *et al.* BHLHE40 Regulates IL-10 and IFN-gamma Production in T Cells but Does Not Interfere With Human Type 1 Regulatory T Cell Differentiation. *Front Immunol* **12**, 683680, doi:10.3389/fimmu.2021.683680 (2021).

29 Salmon, A. J. *et al.* BHLHE40 Regulates the T-Cell Effector Function Required for Tumor Microenvironment Remodeling and Immune Checkpoint Therapy Efficacy. *Cancer Immunol Res* **10**, 597-611, doi:10.1158/2326-6066.CIR-21-0129 (2022).

30 Martinez-Llordella, M. *et al.* CD28-inducible transcription factor DEC1 is required for efficient autoreactive CD4+ T cell response. *J Exp Med* **210**, 1603-1619, doi:10.1084/jem.20122387 (2013).

31 Cook, M. E. *et al.* BHLHE40 Mediates Cross-Talk between Pathogenic TH17 Cells and Myeloid Cells during Experimental Autoimmune Encephalomyelitis. *Immunohorizons* **7**, 737-746, doi:10.4049/immunohorizons.2300042 (2023).

32 Yu, F. *et al.* The transcription factor Bhlhe40 is a switch of inflammatory versus antiinflammatory Th1 cell fate determination. *J Exp Med* **215**, 1813-1821, doi:10.1084/jem.20170155 (2018).

33 Yost, K. E. *et al.* Clonal replacement of tumor-specific T cells following PD-1 blockade. *Nat Med* **25**, 1251-1259, doi:10.1038/s41591-019-0522-3 (2019).

34 Oliveira, G. *et al.* Phenotype, specificity and avidity of antitumour CD8(+) T cells in melanoma. *Nature* **596**, 119-125, doi:10.1038/s41586-021-03704-y (2021).

35 Lowery, F. J. *et al.* Molecular signatures of antitumor neoantigen-reactive T cells from metastatic human cancers. *Science* **375**, 877-884, doi:10.1126/science.abl5447 (2022).

36 Lee, P. P. *et al.* A critical role for Dnmt1 and DNA methylation in T cell development, function, and survival. *Immunity* **15**, 763-774, doi:10.1016/s1074-7613(01)00227-8 (2001).

37 Maekawa, Y. *et al.* Notch2 integrates signaling by the transcription factors RBP-J and CREB1 to promote T cell cytotoxicity. *Nat Immunol* **9**, 1140-1147, doi:10.1038/ni.1649 (2008).

38 Meng, W. *et al.* Improvement of Tumor Neoantigen Detection by High-Field Asymmetric Waveform Ion Mobility Mass Spectrometry. *Cancer Immunol Res* **12**, 988-1006, doi:10.1158/2326-6066.CIR-23-0900 (2024).

39 Sultan, H. *et al.* Neoantigen-specific cytotoxic Tr1 CD4 T cells suppress cancer immunotherapy. *Nature* **632**, 182-191, doi:10.1038/s41586-024-07752-y (2024).

40 Meeth, K., Wang, J. X., Micevic, G., Damsky, W. & Bosenberg, M. W. The YUMM lines: a series of congenic mouse melanoma cell lines with defined genetic alterations. *Pigment Cell Melanoma Res* **29**, 590-597, doi:10.1111/pcmr.12498 (2016).

41 Keshari, S. *et al.* Comparing neoantigen cancer vaccines and immune checkpoint therapy unveils an effective vaccine and anti-TREM2 macrophage-targeting dual therapy. *Cell Rep* **43**, 114875, doi:10.1016/j.celrep.2024.114875 (2024).

42 Sade-Feldman, M. *et al.* Defining T Cell States Associated with Response to Checkpoint Immunotherapy in Melanoma. *Cell* **175**, 998-1013 e1020, doi:10.1016/j.cell.2018.10.038 (2018).

43 Miller, B. C. *et al.* Subsets of exhausted CD8(+) T cells differentially mediate tumor control and respond to checkpoint blockade. *Nat Immunol* **20**, 326-336, doi:10.1038/s41590-019-0312-6 (2019).

44 Pauken, K. E. *et al.* Single-cell analyses identify circulating anti-tumor CD8 T cells and markers for their enrichment. *J Exp Med* **218**, doi:10.1084/jem.20200920 (2021).

45 Chu, Y. *et al.* Pan-cancer T cell atlas links a cellular stress response state to immunotherapy resistance. *Nat Med* **29**, 1550-1562, doi:10.1038/s41591-023-02371-y (2023).

46 Blank, C. U. *et al.* Defining 'T cell exhaustion'. *Nat Rev Immunol* **19**, 665-674, doi:10.1038/s41577-019-0221-9 (2019).

47 Barber, D. L. *et al.* Restoring function in exhausted CD8 T cells during chronic viral infection. *Nature* **439**, 682-687, doi:10.1038/nature04444 (2006).

48 Pauken, K. E. *et al.* Epigenetic stability of exhausted T cells limits durability of reinvigoration by PD-1 blockade. *Science* **354**, 1160-1165, doi:10.1126/science.aaf2807 (2016).

49 Belk, J. A. *et al.* Genome-wide CRISPR screens of T cell exhaustion identify chromatin remodeling factors that limit T cell persistence. *Cancer Cell* **40**, 768-786 e767, doi:10.1016/j.ccell.2022.06.001 (2022).

50 Giles, J. R., Globig, A. M., Kaech, S. M. & Wherry, E. J. CD8(+) T cells in the cancer-immunity cycle. *Immunity* **56**, 2231-2253, doi:10.1016/j.immuni.2023.09.005 (2023).

51 Jennings, E. *et al.* Nr4a1 and Nr4a3 Reporter Mice Are Differentially Sensitive to T Cell Receptor Signal Strength and Duration. *Cell Rep* **33**, 108328, doi:10.1016/j.celrep.2020.108328 (2020).

52 Hao, J. *et al.* NR4A1 transcriptionally regulates the differentiation of stem-like CD8(+) T cells in the tumor microenvironment. *Cell Rep* **43**, 114301, doi:10.1016/j.celrep.2024.114301 (2024).

53 Scott, A. C. *et al.* TOX is a critical regulator of tumour-specific T cell differentiation. *Nature* **571**, 270-274, doi:10.1038/s41586-019-1324-y (2019).

54 Khan, O. *et al.* TOX transcriptionally and epigenetically programs CD8(+) T cell exhaustion. *Nature* **571**, 211-218, doi:10.1038/s41586-019-1325-x (2019).

55 Alfei, F. *et al.* TOX reinforces the phenotype and longevity of exhausted T cells in chronic viral infection. *Nature* **571**, 265-269, doi:10.1038/s41586-019-1326-9 (2019).

56 Philip, M. & Schietinger, A. CD8(+) T cell differentiation and dysfunction in cancer. *Nat Rev Immunol* **22**, 209-223, doi:10.1038/s41577-021-00574-3 (2022).

57 Utzschneider, D. T. *et al.* T Cell Factor 1-Expressing Memory-like CD8(+) T Cells Sustain the Immune Response to Chronic Viral Infections. *Immunity* **45**, 415-427, doi:10.1016/j.immuni.2016.07.021 (2016).

58 Siddiqui, I. *et al.* Intratumoral Tcf1(+)PD-1(+)CD8(+) T Cells with Stem-like Properties Promote Tumor Control in Response to Vaccination and Checkpoint Blockade Immunotherapy. *Immunity* **50**, 195-211 e110, doi:10.1016/j.immuni.2018.12.021 (2019).

59 Escobar, G., Mangani, D. & Anderson, A. C. T cell factor 1: A master regulator of the T cell response in disease. *Sci Immunol* **5**, doi:10.1126/sciimmunol.abb9726 (2020).

60 Gill, A. L. *et al.* PD-1 blockade increases the self-renewal of stem-like CD8 T cells to compensate for their accelerated differentiation into effectors. *Sci Immunol* **8**, eadg0539, doi:10.1126/sciimmunol.adg0539 (2023).

61 Wang, K. *et al.* Combination anti-PD-1 and anti-CTLA-4 therapy generates waves of clonal responses that include progenitor-exhausted CD8(+) T cells. *Cancer Cell* **42**, 1582-1597 e1510, doi:10.1016/j.ccell.2024.08.007 (2024).

62 Mok, S. *et al.* Anti-CTLA-4 generates greater memory response than anti-PD-1 via TCF-1. *Proc Natl Acad Sci U S A* **122**, e2418985122, doi:10.1073/pnas.2418985122 (2025).

63 Kovanen, P. E. *et al.* T-cell development and function are modulated by dual specificity phosphatase DUSP5. *J Biol Chem* **283**, 17362-17369, doi:10.1074/jbc.M709887200 (2008).

64 Kutty, R. G. *et al.* Dual Specificity Phosphatase 5 Is Essential for T Cell Survival. *PLoS One* **11**, e0167246, doi:10.1371/journal.pone.0167246 (2016).

65 Nguyen, C. *et al.* Bhlhe40 Promotes CD4+ T Helper 1 Cell and Suppresses T Follicular Helper Cell Differentiation during Viral Infection. *J Immunol* **212**, 1829-1842, doi:10.4049/jimmunol.2300355 (2024).

66 Verma, A. *et al.* TCF1 dosage determines cell fate during T cell development. *Sci Adv* **10**, eado5982, doi:10.1126/sciadv.ado5982 (2024).

67 Simpson, T. R. *et al.* Fc-dependent depletion of tumor-infiltrating regulatory T cells co-defines the efficacy of anti-CTLA-4 therapy against melanoma. *J Exp Med* **210**, 1695-1710, doi:10.1084/jem.20130579 (2013).

68 Oliveira, G. *et al.* Landscape of helper and regulatory antitumour CD4(+) T cells in melanoma. *Nature* **605**, 532-538, doi:10.1038/s41586-022-04682-5 (2022).

69 Liakou, C. I. *et al.* CTLA-4 blockade increases IFNgamma-producing CD4+ICOShi cells to shift the ratio of effector to regulatory T cells in cancer patients. *Proc Natl Acad Sci U S A* **105**, 14987-14992, doi:10.1073/pnas.0806075105 (2008).

70 Chen, H. *et al.* Anti-CTLA-4 therapy results in higher CD4+ICOShi T cell frequency and IFN-gamma levels in both nonmalignant and malignant prostate tissues. *Proc Natl Acad Sci U S A* **106**, 2729-2734, doi:10.1073/pnas.0813175106 (2009).

71 Ng Tang, D. *et al.* Increased frequency of ICOS+ CD4 T cells as a pharmacodynamic biomarker for anti-CTLA-4 therapy. *Cancer Immunol Res* **1**, 229-234, doi:10.1158/2326-6066.CIR-13-0020 (2013).

72 Salmon, A. J. *et al.* BHLHE40 Regulates the T-Cell Effector Function Required for Tumor Microenvironment Remodeling and Immune Checkpoint-Therapy Efficacy. *Cancer Immunol Res*, doi:10.1158/2326-6066.CIR-21-0129 (2022).

73 Molgora, M. *et al.* TREM2 Modulation Remodels the Tumor Myeloid Landscape Enhancing Anti-PD-1 Immunotherapy. *Cell* **182**, 886-900 e817, doi:10.1016/j.cell.2020.07.013 (2020).

74 Katzenelenbogen, Y. *et al.* Coupled scRNA-Seq and Intracellular Protein Activity Reveal an Immunosuppressive Role of TREM2 in Cancer. *Cell* **182**, 872-885 e819, doi:10.1016/j.cell.2020.06.032 (2020).

75 Wu, J. E. *et al.* In vitro modeling of CD8(+) T cell exhaustion enables CRISPR screening to reveal a role for BHLHE40. *Sci Immunol* **8**, eade3369, doi:10.1126/sciimmunol.ade3369 (2023).

76 Blackburn, S. D., Shin, H., Freeman, G. J. & Wherry, E. J. Selective expansion of a subset of exhausted CD8 T cells by alphaPD-L1 blockade. *Proc Natl Acad Sci U S A* **105**, 15016-15021, doi:10.1073/pnas.0801497105 (2008).

77 Im, S. J. *et al.* Defining CD8+ T cells that provide the proliferative burst after PD-1 therapy. *Nature* **537**, 417-421, doi:10.1038/nature19330 (2016).

78 Geltink, R. I. K., Kyle, R. L. & Pearce, E. L. Unraveling the Complex Interplay Between T Cell Metabolism and Function. *Annu Rev Immunol* **36**, 461-488, doi:10.1146/annurev-immunol-042617-053019 (2018).

79 Chang, C. H. *et al.* Metabolic Competition in the Tumor Microenvironment Is a Driver of Cancer Progression. *Cell* **162**, 1229-1241, doi:10.1016/j.cell.2015.08.016 (2015).

80 Delgoffe, G. M. & Powell, J. D. Feeding an army: The metabolism of T cells in activation, anergy, and exhaustion. *Mol Immunol* **68**, 492-496, doi:10.1016/j.molimm.2015.07.026 (2015).

81 Wilfahrt, D. & Delgoffe, G. M. Metabolic waypoints during T cell differentiation. *Nat Immunol* **25**, 206-217, doi:10.1038/s41590-023-01733-5 (2024).

82 Sun, H., Lu, B., Li, R. Q., Flavell, R. A. & Taneja, R. Defective T cell activation and autoimmune disorder in Stra13-deficient mice. *Nat Immunol* **2**, 1040-1047, doi:10.1038/ni721 (2001).

83 Shankaran, V. *et al.* IFNgamma and lymphocytes prevent primary tumour development and shape tumour immunogenicity. *Nature* **410**, 1107-1111, doi:10.1038/35074122 (2001).

84 Miller, B. C. *et al.* Author Correction: Subsets of exhausted CD8(+) T cells differentially mediate tumor control and respond to checkpoint blockade. *Nat Immunol* **20**, 1556, doi:10.1038/s41590-019-0528-5 (2019).

85 Bassez, A. *et al.* A single-cell map of intratumoral changes during anti-PD1 treatment of patients with breast cancer. *Nat Med* **27**, 820-832, doi:10.1038/s41591-021-01323-8 (2021).

86 Minowa, T. *et al.* Single-cell profiling of acral melanoma infiltrating lymphocytes reveals a suppressive tumor microenvironment. *Sci Transl Med* **16**, eadk8832, doi:10.1126/scitranslmed.adk8832 (2024).

87 Su, C. *et al.* Cell-type-specific co-expression inference from single cell RNA-sequencing data. *Nat Commun* **14**, 4846, doi:10.1038/s41467-023-40503-7 (2023).

FIGURE LEGENDS:

Figure 1. Bhlhe40 is expressed in tumor-reactive human T cells. (A) *BHLHE40* transcript levels across immune cell types and various tumor types from TCGA datasets analyzed via GEPIA2021 (https://doi.org/10.1093/nar/gkab418). **(B)** Single-cell analysis of CD8 T cells from pre- and post-treatment basal cell carcinoma patients (GSE123814) reveals elevated *BHLHE40* expression in activated and exhausted CD8 T cells, with higher expression in treatment responders. **(C)** Differential gene expression analysis of cutaneous (phs001451.v3.p1) and acral melanoma (GSE242477) datasets demonstrates enrichment of *BHLHE40* in tumor-reactive CD8 T cells compared to non-tumor specific or non-reactive CD8 T cells (as defined by Olivera et al. and Minowa et al.).

Figure 2. CD8 T cell-intrinsic Bhlhe40 is essential for anti-PD-1 but not anti-CTLA-4 efficacy. (A) Bhlhe40 conditional knockout mice bearing 1956 MCA sarcoma were treated with anti-PD-1 or anti-CTLA-4 as indicated. **(B)** Tumor growth curve of 1956 tumors in Bhlhe40$^{fl/fl}$ (B$^{f/f}$) and Bhlhe40$^{\Delta CD8}$ (B$^{\Delta CD8}$) mice treated with control antibody (Ab), anti-PD-1, or anti-CTLA-4. **(C)** Percent tumor rejection of 1956 tumors in B$^{f/f}$ and Bhlhe40$^{\Delta CD8}$ (B$^{\Delta CD8}$) mice treated with control Ab, anti-PD-1, or anti-CTLA-4. **(D)** Flow cytometry plots of mPsmd6-H2-K^{b} peptide-MHC tetramer staining for NeoAg-specific CD8 T cells in B$^{f/f}$ and B$^{\Delta CD8}$ mice treated with control Ab, anti-PD-1, or anti-CTLA-4. Gated on live CD45^{+} cells. **(E)** UMAP generated from integration of CD8 T cells from scRNAseq Experiment #1 and scRNAseq Experiment #2 depicting CD8 T cell clusters named based on phenotypic markers. **(F)** Feature plots displaying expression of select markers. **(G)** Violin plots showing *Bhlhe40* expression in CD8 T cells by cluster and treatment in B$^{f/f}$ mice. **(H)** Heatmaps comparing features (module scores) of CD8 T cell clusters (rows) to published mouse and human CD8 T cell gene signatures (columns) identified/annotated by Miller et al. and Pauken et al. (mouse) and by Chu et al., Oliveira et al., and Sade-Feldman et al. (human). For (**B**) and **(C)**, tumor growth is presented as mean +/- SEM of mean tumor diameter of individual

mice. Tumor rejection graphs display cumulative percentage of mice with complete tumor rejection (∗∗∗p < 0.001; ns, not significant, 2-way ANOVA).

Figure 3. CD8 T cell-intrinsic Bhlhe40 governs effector differentiation and function. (A) Graphs displaying IFN-γ^+ CD8 T cells (as a percentage of CD8 T cells), IFN-γ MFI of IFN-γ^+ CD8 T cells, and IFN-γ^+ TNF-α^+ CD8 T cells (as a percentage of CD8 T cells). **(B)** Heatmap displaying normalized Hallmark IFNγ response GSEA enrichment score (NES) for CD8 T cell clusters in $B^{\Delta CD8}$ versus $B^{f/f}$ mice treated with anti-PD-1 or anti-CTLA-4. **(C)** GSEA plots for the Hallmark IFNγ response in PD1^{hi}_Eff/Ex, Nr4a1^{hi}_Eff/Ex and Eff_Cycling CD8 T clusters in $B^{\Delta CD8}$ mice comparing anti-CTLA-4 vs anti-PD-1 treatment. **(D)** Dot plot showing expression level and percent of cells expressing *Tox* by treatment condition in $B^{f/f}$ vs $B^{\Delta CD8}$ mice in all CD8 clusters. **(E)** Spearman correlation analysis of all CD8 T cell clusters relative to Bhlhe40 compared in $B^{f/f}$ mice. Dot color indicates the p-value. **(F)** Dot plot showing expression level and percent of cells expressing *Tcf7* by treatment condition in $B^{f/f}$ vs $B^{\Delta CD8}$ mice in all CD8 clusters, Naïve_Mem, Pexlike_Ifn-stim, and Tox^{hi} Eff_Ex clusters. **(G)** Graphs displaying PD-1$^+$TCF-1$^+$ CD8 T cells (as a percentage of CD8 T cells). **(H)** Heatmap displaying transcript expression of effector/exhaustion markers (*Pdcd1, Lag3, Havcr2, Ifng*) and memory-associated markers (*Tcf7, Il7r*) in $B^{+/+}$ and $B^{-/-}$ OT-I T cells under *ex vivo* acute and chronic stimulation conditions with cognate SIINFEKL peptide-loaded APCs (see methods). For (**A**), IFN-γ and TNF-α was determined via intracellular cytokine staining of *ex vivo* restimulated CD8 T cells isolated from 1956 tumors on day 10 post-tumor transplant. Bar graphs display the mean ± SEM and are representative of at least three independent experiments (∗∗p < 0.01, ∗∗∗p < 0.001; ns, not significant, unpaired t test). For (**G**), TCF-1 and PD-1 expression was assessed via intracellular/intranuclear staining and flow cytometry of 1956 tumors on day 10 post-tumor transplant. Bar graphs display the mean ± SEM and are representative of two independent experiments (∗p < 0.05; ∗∗p < 0.01, ns, not significant, unpaired t test).

Figure 4. *BHLHE40* expression correlates with effector and exhaustion-associated programs in human intratumoral CD8 T cells. (**A**) Feature plot showing expression of *BHLHE40, TOX, TCF7*, and *IFNG* in CD8 T cell clusters from human basal cell carcinoma as identified and annotated by Yost et al. (left) and UMAP showing clusters positive or negative for *BHLHE40* and *TCF7* (right). **(B)** Dot plot displaying expression of select transcripts in CD8 T cell clusters. **(C)** Gene co-expression heatmap using CS-CORE package. **(D)** Feature plot showing expression of *BHLHE40, TOX, TCF7*, and *IFNG* in CD8 T cell clusters from human triple-negative breast cancer (TNBC) as identified and annotated by Bassez et al. **(E)** Dot plot displaying expression of select transcripts in CD8 T cell clusters. **(F)** Gene co-expression heatmap of human melanoma intratumoral CD8 T cells from Sade-Feldman et al. (left) and Minowa et al. (right). **(A-C)** Reanalysis of scRNAseq data of CD8 T cells from human basal cell carcinoma from Yost et al. (**D-E**) Reanalysis of scRNAseq data of CD8 T cells from TNBC from Bassez et al. (**F**) Reanalysis of scRNAseq data of CD8 T cells from human melanoma from Sade-Feldman et al. and Minowa et al.

Figure 5. Bhlhe40 supports glycolytic and oxidative phosphorylation in CD8 T cells in a therapy-dependent manner. (A) Dot plot showing expression of select glycolytic genes (*Aldoa, Gapdh, Eno1,* etc.) in all CD8 T cell clusters. **(B)** GSEA showing enrichment of Hallmark glycolysis pathway in PD1^{hi}_Eff/Ex and Nr4a1^{hi}_Eff/Ex cluster between B$^{f/f}$ vs B$^{\Delta CD8}$ mice with anti-PD-1 treatment. **(C)** XF real-time ATP production rate comparing glycolytic and mitochondrial ATP on *ex vivo* intratumoral CD8 T cells in B$^{f/f}$ and B$^{\Delta CD8}$ mice treated with control Ab, anti-PD-1, or anti-CTLA-4. **(D)** XF real-time ATP seahorse assay showing ECAR and OCR on *ex vivo* intratumoral CD8 T cells in B$^{f/f}$ and B$^{\Delta CD8}$ mice treated with control Ab, anti-PD-1, or anti-CTLA-4. For **(C)** and **(D)** (∗∗$p < 0.01$; ∗∗∗$p < 0.001$; ∗∗∗∗$p < 0.0001$; ns, not significant, unpaired t test or 2-way ANOVA).

Figure 6. CD4 T cell-intrinsic Bhlhe40 sustains anti-CTLA-4-driven Th1 responses. (A) UMAP generated from integration of CD4 T cells from scRNAseq Experiment #1 and scRNAseq Experiment #2 depicting distinct CD4 T cell and Treg clusters. **(B)** Violin plots showing *Bhlhe40* expression in CD4 T cells by cluster and treatment in $B^{f/f}$ mice. **(C)** Heatmaps comparing features (module scores) of CD4 T cell clusters (rows) to published human CD4 T cell gene signatures (columns) identified/annotated by Chu et al. and Oliveira et al. **(D)** Stacked bar graph showing Th1 clusters as a percentage of CD4 T cells from $B^{f/f}$, $B^{\Delta T}$ and $B^{\Delta CD8}$ mice treated with control Ab, anti-PD-1, or anti-CTLA-4. **(E)** Violin plot showing *Ifng* expression in $ICOS^{hi}Bhlhe40^{hi}$_Th1_6, $ICOS^{+}Bhlhe40^{+}$_Th1_7, and $Gzmk^{+}$_Th1_8 CD4 clusters by treatment in $B^{f/f}$, $B^{\Delta T}$, or $B^{\Delta CD8}$ mice. **(F)** Dot plot displaying select glycolytic transcript expression level and percent of cells in effector CD4 T cell clusters.

Figure 7. Bhlhe40-dependent T cell mediated macrophage remodeling following ICT. (A) UMAP generated from scRNAseq Experiment 1 (scRNA_1) by subclustering only macrophage clusters from $B^{f/f}$, $B^{\Delta T}$, or $B^{\Delta CD8}$ mice. **(B)** Dot plot showing expression level and percent of cells expressing select genes in all macrophage clusters between $B^{f/f}$, $B^{\Delta T}$, or $B^{\Delta CD8}$ mice. **(C)** Stacked bar graph showing clusters as a percentage of total macrophage from $B^{f/f}$, $B^{\Delta T}$ and $B^{\Delta CD8}$ mice treated with control Ab, anti-PD-1, or anti-CTLA-4. **(D)** Representative flow cytometry plots (gated on macrophages) displaying intratumoral $CX3CR1^{+}CD206^{+}$ and $iNOS^{+}$ macrophages from 1956 tumor bearing $B^{f/f}$, $B^{\Delta T}$, or $B^{\Delta CD8}$ mice treated with control Ab, anti-PD-1 or anti-CTLA-4 and harvested on day 10 post-tumor transplant.

FIGURE LEGENDS FOR SUPPLEMENTARY FIGURES:

Figure S1. *BHLHE40* transcript levels across immune cell types and various tumor types from TCGA datasets analyzed via GEPIA2021 (https://doi.org/10.1093/nar/gkab418).

Figure S2. Validation of Bhlhe40 deletion and 1956 tumor growth in $B^{\Delta T}$ and $B^{\Delta CD8}$ mice under anti-PD-1 or anti-CTLA-4 ICT. (A) Bar graph showing relative *Bhlhe40* mRNA expression in CD4 and CD8 T cells from $B^{f/f}$ and $B^{\Delta CD8}$ mice. **(B)** Tumor growth curve of 1956 tumors in Bhlhe40$^{fl/fl}$ ($B^{f/f}$) and Bhlhe40$^{\Delta T}$ ($B^{\Delta T}$) mice treated with control antibody (Ab), anti-PD-1, or anti-CTLA-4. **(C)** Tumor growth of individual 1956 tumor bearing $B^{f/f}$ and $B^{\Delta CD8}$ mice corresponding to Figure 2B. For (**A**), RNA was isolated from intratumoral CD4 and CD8 T cells sorted from 1956 tumors in $B^{f/f}$ and $B^{\Delta CD8}$ treated with control Ab, anti-PD-1, or anti-CTLA-4. Bar graphs display the mean ± SEM and are representative of at least three independent experiments (*$p<0.05$, **$p < 0.01$; ns, not significant, unpaired t test). For **(B)** tumor growth is presented as mean +/- SEM of mean tumor diameter of individual mice and are representative of at least four independent experiments (***$p < 0.001$; ns, not significant, 2-way ANOVA).

Figure S3. Tumor growth in Y1.7LI tumor-bearing $B^{\Delta CD8}$ mice and in 1956 tumor bearing CD8 E8I-Cre Bhlhe40$^{+/+}$ and $B^{f/f}$ mice. **(A)** Bhlhe40 conditional knockout mice bearing Y1.7LI melanoma tumors were treated with anti-PD-1 or anti-CTLA-4 as indicated. **(B)** Tumor growth and percent tumor rejection of Y1.7LI melanoma tumors in $B^{f/f}$ and $B^{\Delta CD8}$ mice treated with control Ab, anti-PD-1, or anti-CTLA-4. **(C)** Tumor growth of individual Y1.7LI tumor bearing $B^{f/f}$ and $B^{\Delta CD8}$ mice corresponding to Figure S3B. **(D)** Tumor growth curve of 1956 tumors between CD8 E8I-Cre Bhlhe40$^{+/+}$ mice and $B^{f/f}$ mice treated with control Ab, anti-PD-1, or anti-CTLA-4. For **(B)** and **(D),** tumor growth is presented as mean +/- SEM of mean tumor diameter of individual mice. Tumor rejection graphs display cumulative percentage of mice with complete tumor

rejection and are representative of at least three independent experiments (∗∗∗p < 0.001; ∗∗∗∗p < 0.0001; ns, not significant, 2-way ANOVA).

Figure S4. Single cell RNAseq integration and analysis of intratumoral CD8 T cells from $B^{f/f}$, $B^{\Delta T}$, and $B^{\Delta CD8}$ mice treated with anti-PD-1 or anti-CTLA-4 ICT. (A) Schematic representation of integration of scRNA Experiment #1 and Experiment #2. **(B)** Workflow to generate integrated datasets. **(C)** Bar graph showing percent of CD8 T cells as determined by flow cytometry staining of intratumoral cells isolated from 1956 tumor bearing $B^{f/f}$ and $B^{\Delta CD8}$ mice treated with control Ab, anti-PD-1, or anti-CTLA-4. **(D)** Violin plots denoting expression levels of select genes in each CD8 clusters. **(E)** Dot plot displaying expression level and percent of cells expressing select genes in CD8 T cell clusters. **(F)** Stacked bar graph showing clusters as a percentage of total CD8 T cells from $B^{f/f}$, $B^{\Delta T}$ and $B^{\Delta CD8}$ mice under different treatment conditions. **(G)** Scatter plot displaying *Tcf7* and *Tox* expression in cells within Tox^{hi}_Eff_Ex cluster and 2x2 contingency table showing number of cells within Tox^{hi}_Eff_Ex expressing *Tcf7* and/or *Tox*. Bar graphs in (**C**) display the mean ± SEM and are representative of at least three independent experiments (∗∗p < 0.01; ns, not significant, unpaired t test).

Figure S5. Heat map displaying normalized expression of select genes by CD8 T cell cluster and condition.

Figure S6. Select gene expression profiles of CD8 T cell clusters from integrated scRNAseq analysis. (A) Dot plot displaying expression level and percent of cells expressing select genes in CD8 T cell clusters. **(B)** Dot plot showing expression of select genes (*Ifng, Prf1,* and *Gzmk*) in $PD1^{hi}$_Eff_Ex, $Nr4a1^{hi}$_Eff_Ex, Eff_Cycling, $Cd39^{+}$_Eff_Ex, and Tox^{hi}_Eff_Ex clusters. **(C)** Dot plot showing *Il-10* expression in clusters $PD1^{hi}$_Eff_Ex and $Nr4a1^{hi}$_Eff_Ex.

Figure S7. GSEA in PD1^{hi}_Eff_Ex, Nr4a1^{hi}_Eff_Ex, Tox^{hi}_Eff_Ex, Cd39^{+}_Eff_Ex, and Pexlike_Ifn-stim CD8 clusters with anti-PD-1 treatment between B$^{f/f}$ and B$^{\Delta CD8}$ mice. White indicates non-significant hallmark pathways; red indicates significantly upregulated hallmark pathways; blue indicates significantly downregulated hallmark pathways).

Figure S8. GSEA in PD1^{hi}_Eff_Ex, Nr4a1^{hi}_Eff_Ex, and Tox^{hi}_Eff_Ex clusters with anti-CTLA-4 treatment between B$^{f/f}$ and B$^{\Delta CD8}$ mice. White indicates non-significant hallmark pathways; red indicates significantly upregulated hallmark pathways; blue indicates significantly downregulated hallmark pathways.

Figure S9. Dot plot showing expression of select genes in PD1^{hi}_Eff_Ex, Nr4a1^{hi}_Eff_Ex, Tox^{hi}_Eff_Ex, and Eff_Cycling CD8 clusters.

Figure S10. Bar plot showing Spearman correlation of all genes with *Bhlhe40* in the CD8 T cell clusters. Red dots indicate genes are positively correlated to Bhlhe40, blue dots indicate negative correlation. Metabolic transcripts are indicated in green dots.

Figure S11. *Tcf7* expression in CD8 T cell clusters and reduced tumor control by Bhlhe40-deficient OT-1 T cells in the B16-OVA model (A) *Tcf7* feature plot of CD8 T cell clusters. **(B)** Tumor growth of B16-OVA tumors in mice adoptively transferred with either PBS, B$^{+/+}$ OT-1 or B$^{-/-}$ OT-1 splenocytes stimulated ex vivo with SIINFEKL peptide. Tumor growth in (**B**) is presented as mean +/- SEM of mean tumor diameter of individual mice and is representative of 2 independent experiments (∗∗∗$p < 0.001$; ∗∗∗∗$p < 0.0001$; ns, not significant, 2-way ANOVA).

Figure S12. Differentially expressed genes and metabolic gene expression in effector/exhausted CD8 T cell clusters following Bhlhe40 deletion. (A) Volcano plot showing differentially expressed genes between B$^{f/f}$ and B$^{\Delta CD8}$ mice treated with anti-PD-1 in PD1^{hi}_Eff_Ex and Nr4a1^{hi}_Eff_Ex clusters. Significantly differentially expressed transcripts (log2FC < -0.5 or

log2FC > 0.5, adjusted P value < 0.05) are shown in red. Statistical analysis was performed using a two-sided nonparametric Wilcoxon rank sum test with Bonferroni's correction. **(B)** Dot plot displaying expression level and percent of cells expressing select glycolytic transcripts in effector/exhausted CD8 T cell clusters. **(C)** Dot plot displaying expression level and percent of cells expressing select OXPHOS transcripts in effector/exhausted CD8 T cell clusters.

Figure S13. CD4 T cell subset composition and transcriptional profiles under ICT in $B^{f/f}$, $B^{\Delta T}$ and $B^{\Delta CD8}$ mice. (A) Bar graph showing percent of conventional CD4 T cells and $Foxp3^{+}$ Tregs from $B^{f/f}$ and $B^{\Delta CD8}$ mice treated with control Ab, anti-PD-1, or anti-CTLA-4. Bar graphs display the mean ± SEM and are representative of at least three independent experiments (*p<0.05, unpaired t test). **(B)** Stacked bar graph showing fraction of the subtypes of CD4. **(C)** Dot plot showing expression level and percent of cells in select genes in $ICOS^{hi}Bhlhe40^{hi}$_Th1_6, $ICOS^{+}Bhlhe40^{+}$_Th1_7, and $Gzmk^{+}$_Th1_8 CD4 clusters. **(D)** Heat map displaying normalized expression of select genes in each CD4 T cell clusters by treatment condition in $B^{f/f}$, $B^{\Delta T}$, and $B^{\Delta CD8}$ mice.

Figure 1

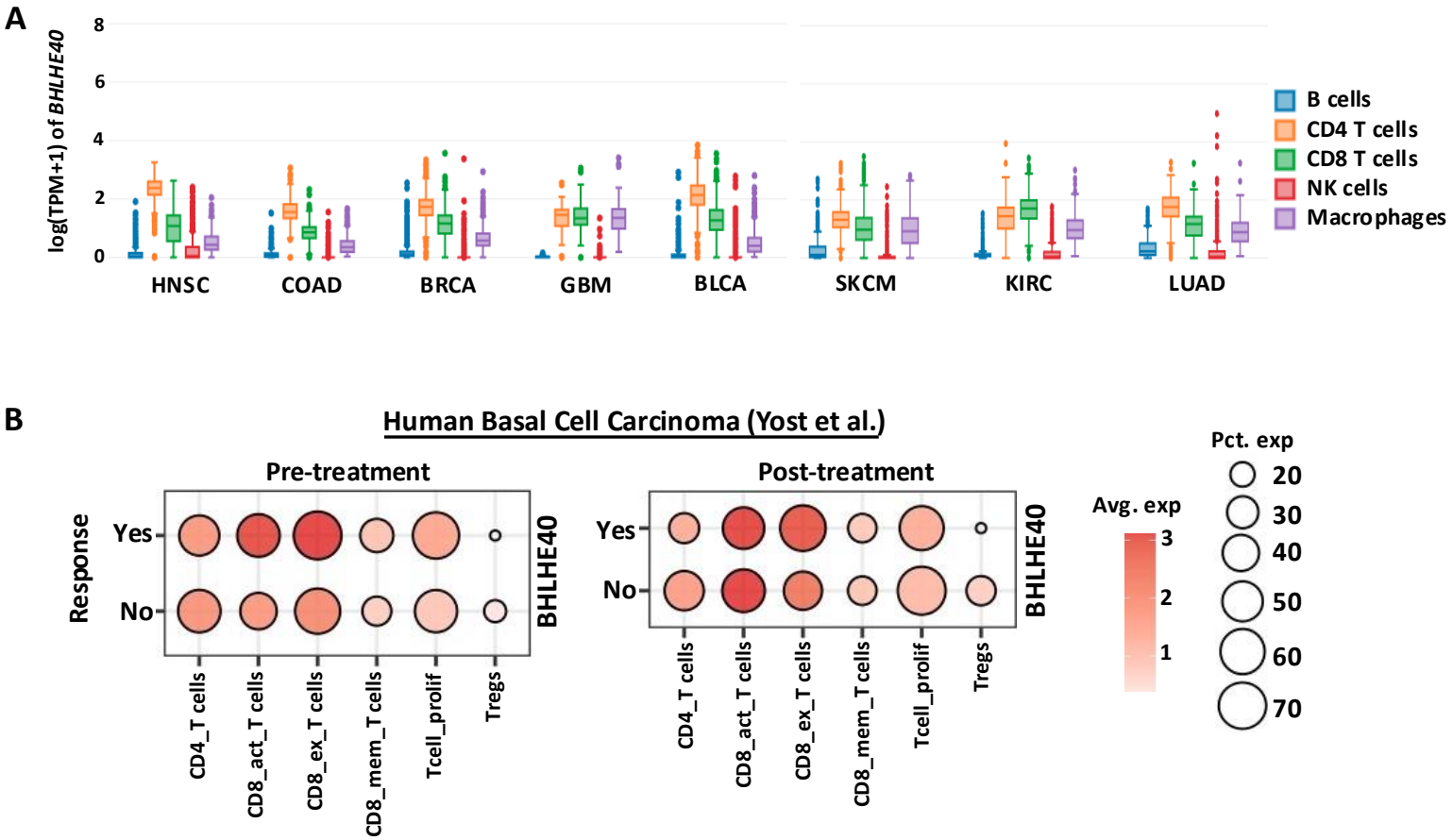
A
log(TPM+1) of BHLHE40
8
6
4
2
0
HNSC
COAD
BRCA
GBM
BLCA
SKCM
KIRC
LUAD
B cells
CD4 T cells
CD8 T cells
NK cells
Macrophages
B
Human Basal Cell Carcinoma (Yost et al.)
Pre-treatment
Post-treatment
Response
Yes
No
BHLHE40
CD4_T cells
CD8_act_T cells
CD8_ex_T cells
CD8_mem_T cells
Tcell_prolif
Tregs
Avg. exp
3
2
1
Pct. exp
20
30
40
50
60
70

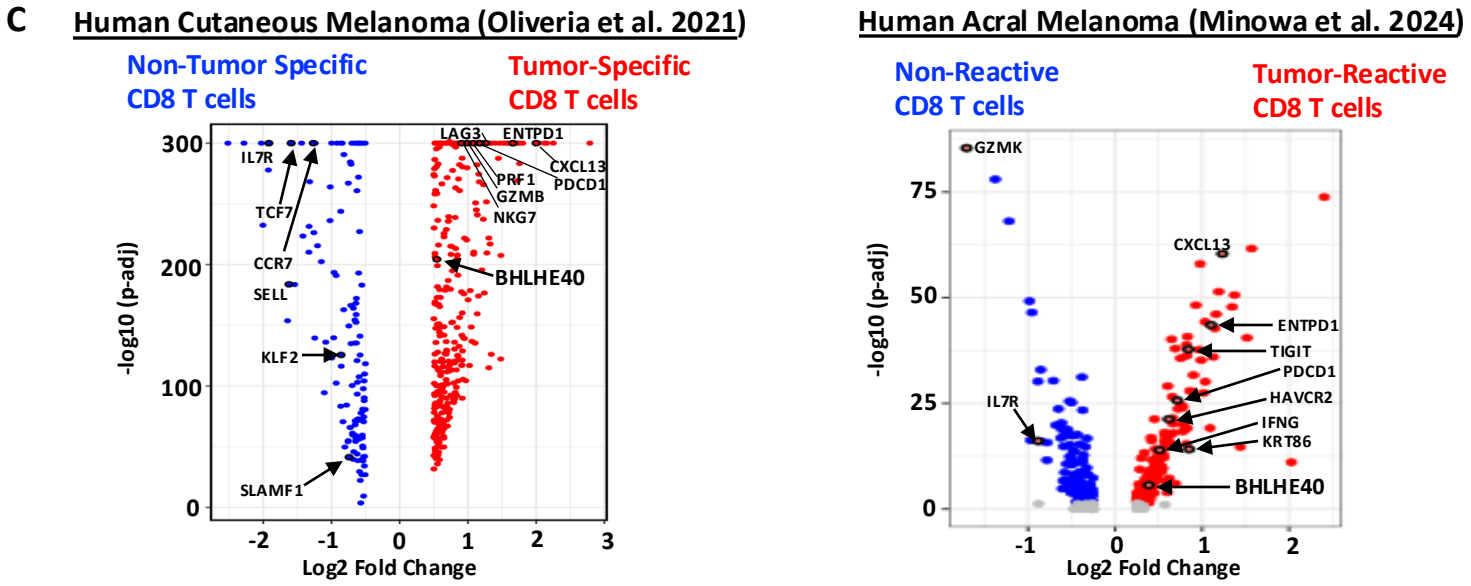
C
Human Cutaneous Melanoma (Oliveria et al. 2021)
Non-Tumor Specific CD8 T cells
Tumor-Specific CD8 T cells
-log10 (p-adj)
Log2 Fold Change
IL7R
TCF7
CCR7
SELL
KLF2
SLAMF1
LAG3
ENTPD1
CXCL13
PDCD1
PRF1
GZMB
NKG7
BHLHE40
Human Acral Melanoma (Minowa et al. 2024)
Non-Reactive CD8 T cells
Tumor-Reactive CD8 T cells
GZMK
CXCL13
ENTPD1
TIGIT
PDCD1
HAVCR2
IFNG
KRT86
IL7R
BHLHE40

Figure 2

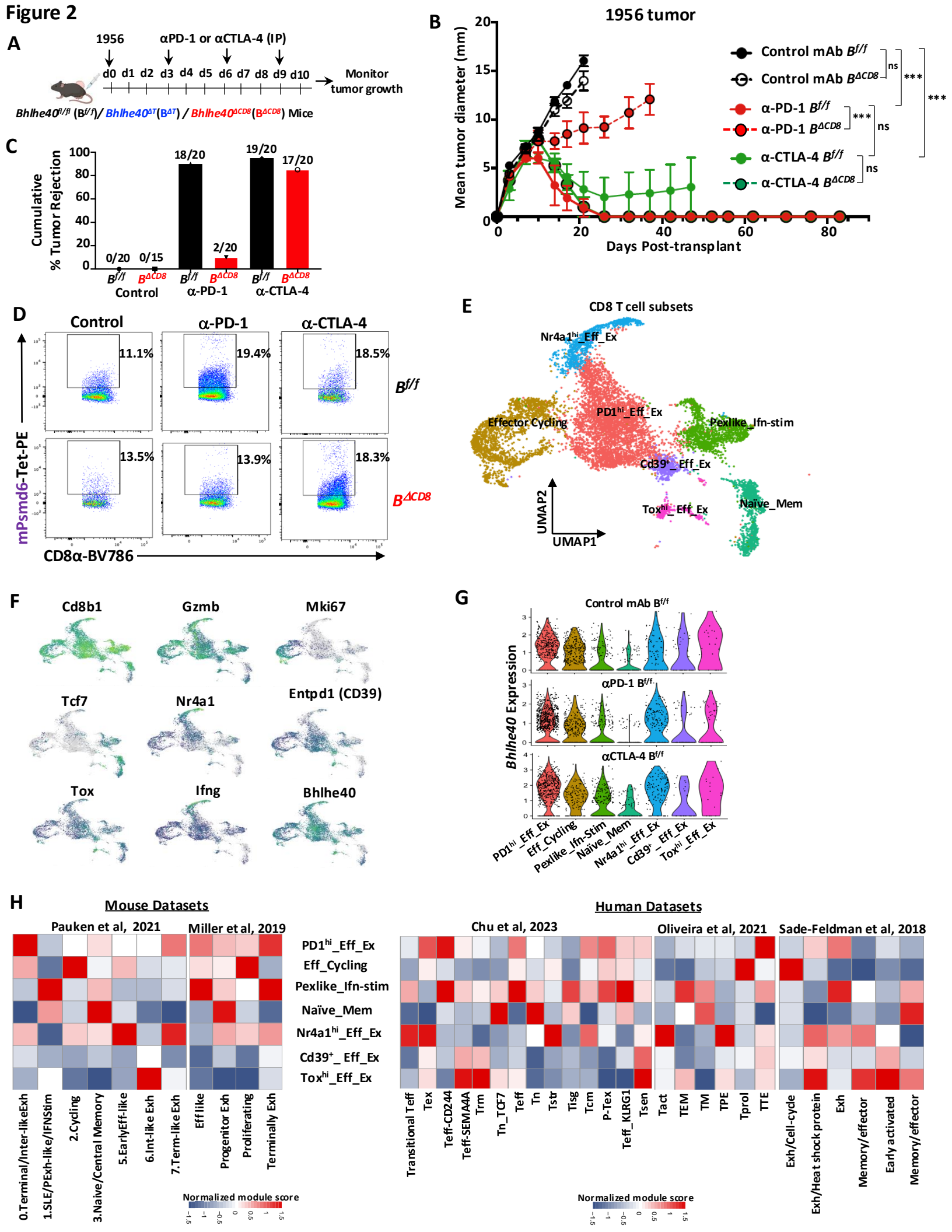
A
1956
αPD-1 or αCTLA-4 (IP)
d0 d1 d2 d3 d4 d5 d6 d7 d8 d9 d10
Monitor tumor growth
Bhlhe40f/fl (Bf/f)/ Bhlhe40ΔT(BΔT) / Bhlhe40ΔCD8(BΔCD8) Mice
B
1956 tumor
Mean tumor diameter (mm)
Days Post-transplant
Control mAb Bf/f
Control mAb BΔCD8
α-PD-1 Bf/f
α-PD-1 BΔCD8
α-CTLA-4 Bf/f
α-CTLA-4 BΔCD8
ns
***
C
Cumulative % Tumor Rejection
0/20
0/15
18/20
2/20
19/20
17/20
Control
α-PD-1
α-CTLA-4
D
Control
α-PD-1
α-CTLA-4
11.1%
19.4%
18.5%
13.5%
13.9%
18.3%
Bf/f
BΔCD8
mPsmd6-Tet-PE
CD8α-BV786
E
CD8 T cell subsets
Nr4a1hi_Eff_Ex
PD1hi_Eff_Ex
Effector Cycling
Pexlike_Ifn-stim
Cd39+_Eff_Ex
Toxhi_Eff_Ex
Naïve_Mem
UMAP2
UMAP1
F
Cd8b1
Gzmb
Mki67
Tcf7
Nr4a1
Entpd1 (CD39)
Tox
Ifng
Bhlhe40
G
Control mAb Bf/f
αPD-1 Bf/f
αCTLA-4 Bf/f
Bhlhe40 Expression
PD1hi_Eff_Ex
Eff_Cycling
Pexlike_Ifn-stim
Naïve_Mem
Nr4a1hi_Eff_Ex
Cd39+_Eff_Ex
Toxhi_Eff_Ex
H
Mouse Datasets
Pauken et al, 2021
Miller et al, 2019
PD1hi_Eff_Ex
Eff_Cycling
Pexlike_Ifn-stim
Naïve_Mem
Nr4a1hi_Eff_Ex
Cd39+_ Eff_Ex
Toxhi_Eff_Ex
0.Terminal/Inter-likeExh
1.SLE/PExh-like/IFNStim
2.Cycling
3.Naive/Central Memory
5.EarlyEff-like
6.Int-like Exh
7.Term-like Exh
Eff like
Progenitor Exh
Proliferating
Terminally Exh
Normalized module score
Human Datasets
Chu et al, 2023
Oliveira et al, 2021
Sade-Feldman et al, 2018
Transitional Teff
Tex
Teff-CD244
Teff-SEMA4A
Trm
Tn_TCF7
Teff
Tn
Tstr
Tisg
Tcm
P-Tex
Teff_KLRG1
Tsen
Tact
TEM
TM
TPE
Tprol
TTE
Exh/Cell-cycle
Exh/Heat shock protein
Exh
Memory/effector
Early activated
Memory/effector
Normalized module score

Figure 3

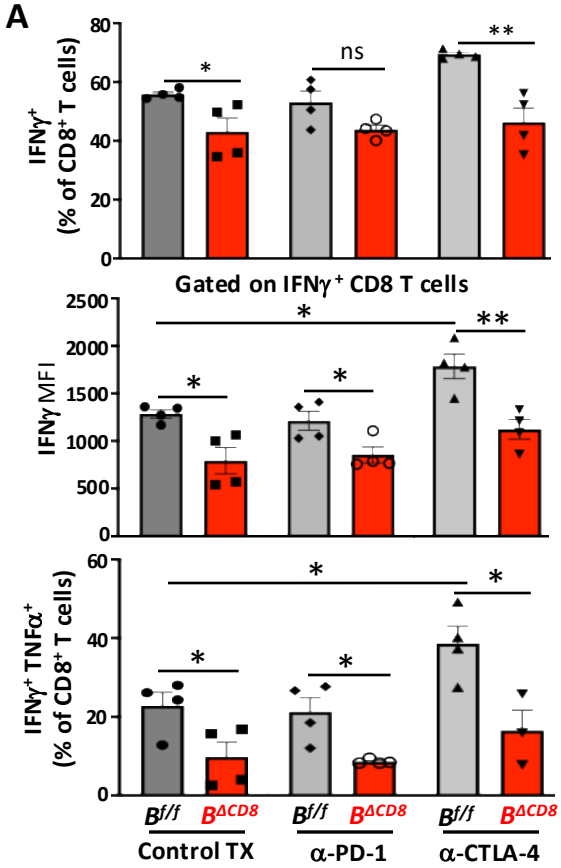
A
IFNγ+ (% of CD8+ T cells)
Gated on IFNγ+ CD8 T cells
IFNγ MFI
IFNγ+ TNFα+ (% of CD8+ T cells)
Bf/f BΔCD8
Control TX
α-PD-1
α-CTLA-4

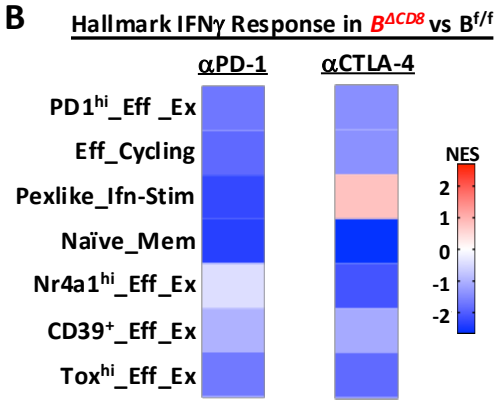
B
Hallmark IFNγ Response in BΔCD8 vs Bf/f
αPD-1
αCTLA-4
PD1hi_Eff _Ex
Eff_Cycling
Pexlike_Ifn-Stim
Naïve_Mem
Nr4a1hi_Eff_Ex
CD39+_Eff_Ex
Toxhi_Eff_Ex
NES

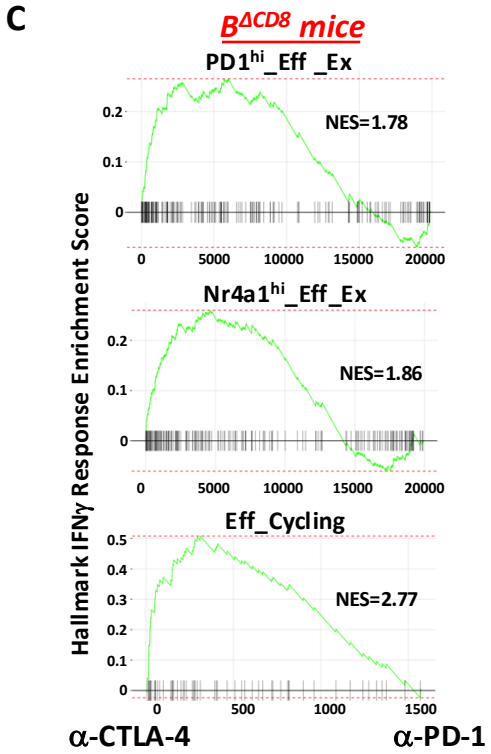
C
BΔCD8 mice
PD1hi_Eff _Ex
NES=1.78
Nr4a1hi_Eff_Ex
NES=1.86
Eff_Cycling
NES=2.77
Hallmark IFNγ Response Enrichment Score
α-CTLA-4
α-PD-1

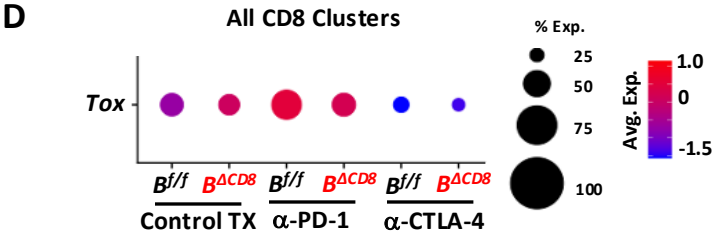
D
All CD8 Clusters
Tox
% Exp.
Avg. Exp.
Bf/f BΔCD8
Control TX
α-PD-1
α-CTLA-4

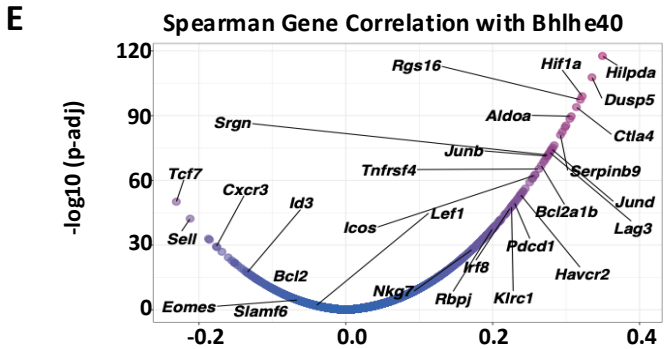
E
Spearman Gene Correlation with Bhlhe40
-log10 (p-adj)
Rgs16
Hif1a
Hilpda
Dusp5
Aldoa
Ctla4
Srgn
Junb
Tnfrsf4
Serpinb9
Tcf7
Cxcr3
Id3
Jund
Bcl2a1b
Lag3
Icos
Lef1
Sell
Pdcd1
Irf8
Havcr2
Bcl2
Nkg7
Rbpj
Klrc1
Eomes
Slamf6

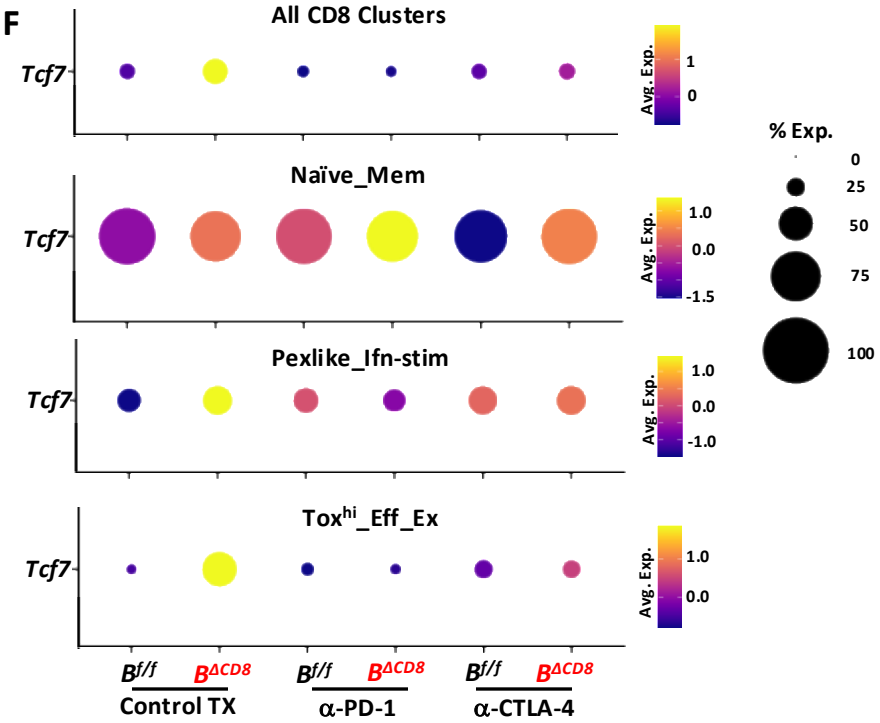
F
All CD8 Clusters
Naïve_Mem
Pexlike_Ifn-stim
Toxhi_Eff_Ex
Tcf7
Avg. Exp.
% Exp.
Bf/f BΔCD8
Control TX
α-PD-1
α-CTLA-4

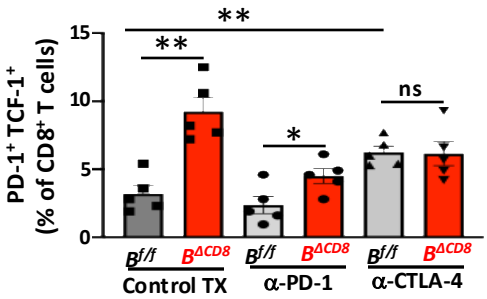
G
PD-1+ TCF-1+ (% of CD8+ T cells)
Bf/f BΔCD8
Control TX
α-PD-1
α-CTLA-4

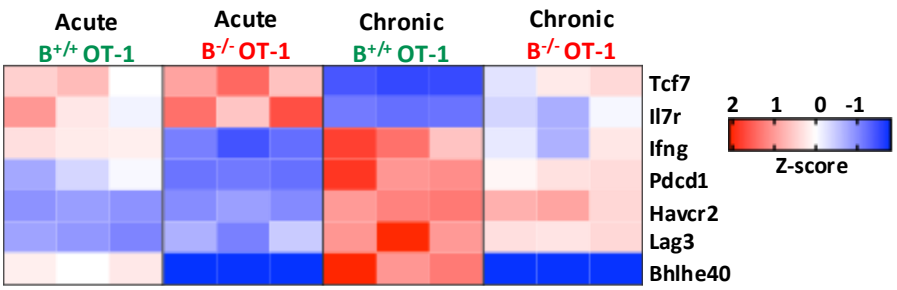
H
Acute B+/+ OT-1
Acute B-/- OT-1
Chronic B+/+ OT-1
Chronic B-/- OT-1
Tcf7
Il7r
Ifng
Pdcd1
Havcr2
Lag3
Bhlhe40
Z-score

Figure 4

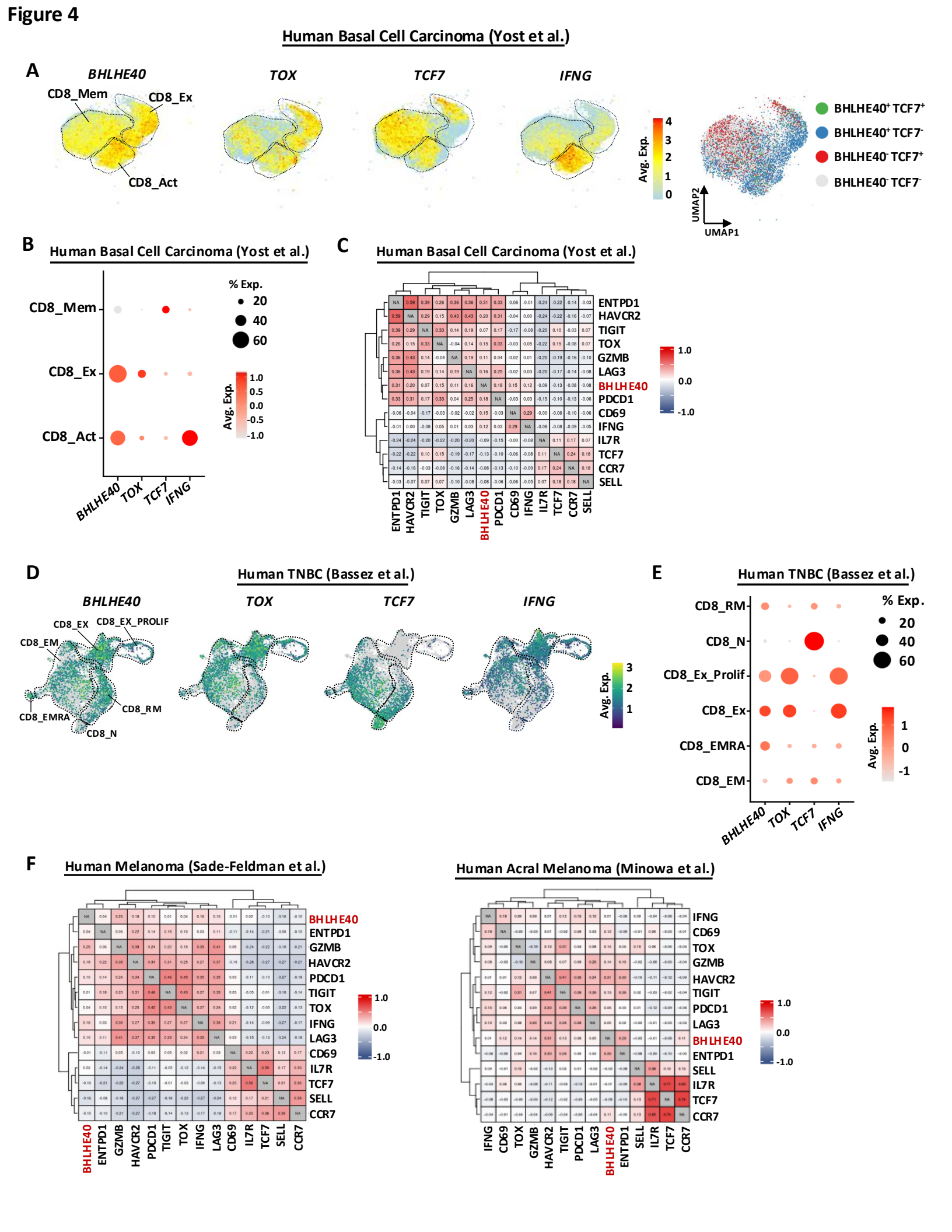
Human Basal Cell Carcinoma (Yost et al.)
A
BHLHE40
TOX
TCF7
IFNG
CD8_Mem
CD8_Ex
CD8_Act
Avg. Exp.
UMAP2
UMAP1
BHLHE40+ TCF7+
BHLHE40+ TCF7-
BHLHE40- TCF7+
BHLHE40- TCF7-
B
Human Basal Cell Carcinoma (Yost et al.)
% Exp.
20
40
60
Avg. Exp.
C
Human Basal Cell Carcinoma (Yost et al.)
ENTPD1
HAVCR2
TIGIT
TOX
GZMB
LAG3
BHLHE40
PDCD1
CD69
IFNG
IL7R
TCF7
CCR7
SELL
D
Human TNBC (Bassez et al.)
CD8_EX
CD8_EX_PROLIF
CD8_EM
CD8_EMRA
CD8_RM
CD8_N
E
Human TNBC (Bassez et al.)
CD8_RM
CD8_N
CD8_Ex_Prolif
CD8_Ex
CD8_EMRA
CD8_EM
F
Human Melanoma (Sade-Feldman et al.)
Human Acral Melanoma (Minowa et al.)

Figure 5

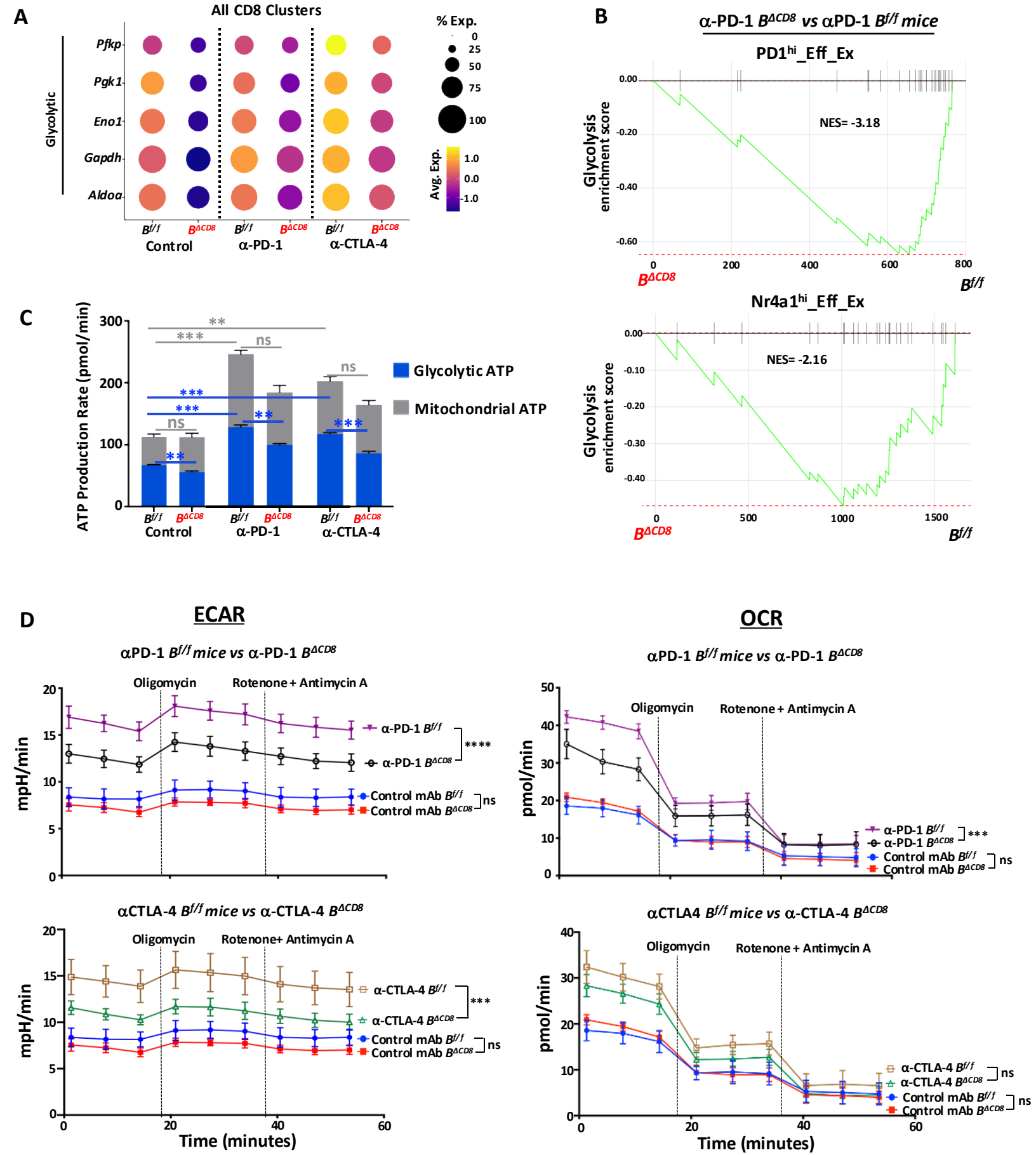
A
All CD8 Clusters
Glycolytic
Pfkp
Pgk1
Eno1
Gapdh
Aldoa
% Exp.
0
25
50
75
100
Avg. Exp.
1.0
0.0
-1.0
Control
α-PD-1
α-CTLA-4
B
α-PD-1 BΔCD8 vs αPD-1 Bf/f mice
PD1hi_Eff_Ex
NES= -3.18
Glycolysis enrichment score
Nr4a1hi_Eff_Ex
NES= -2.16
C
ATP Production Rate (pmol/min)
Glycolytic ATP
Mitochondrial ATP
D
ECAR
OCR
αPD-1 Bf/f mice vs α-PD-1 BΔCD8
Oligomycin
Rotenone + Antimycin A
α-PD-1 Bf/f
α-PD-1 BΔCD8
Control mAb Bf/f
Control mAb BΔCD8
mpH/min
pmol/min
αCTLA-4 Bf/f mice vs α-CTLA-4 BΔCD8
αCTLA4 Bf/f mice vs α-CTLA-4 BΔCD8
Rotenone+ Antimycin A
α-CTLA-4 Bf/f
α-CTLA-4 BΔCD8
Time (minutes)

Figure 6

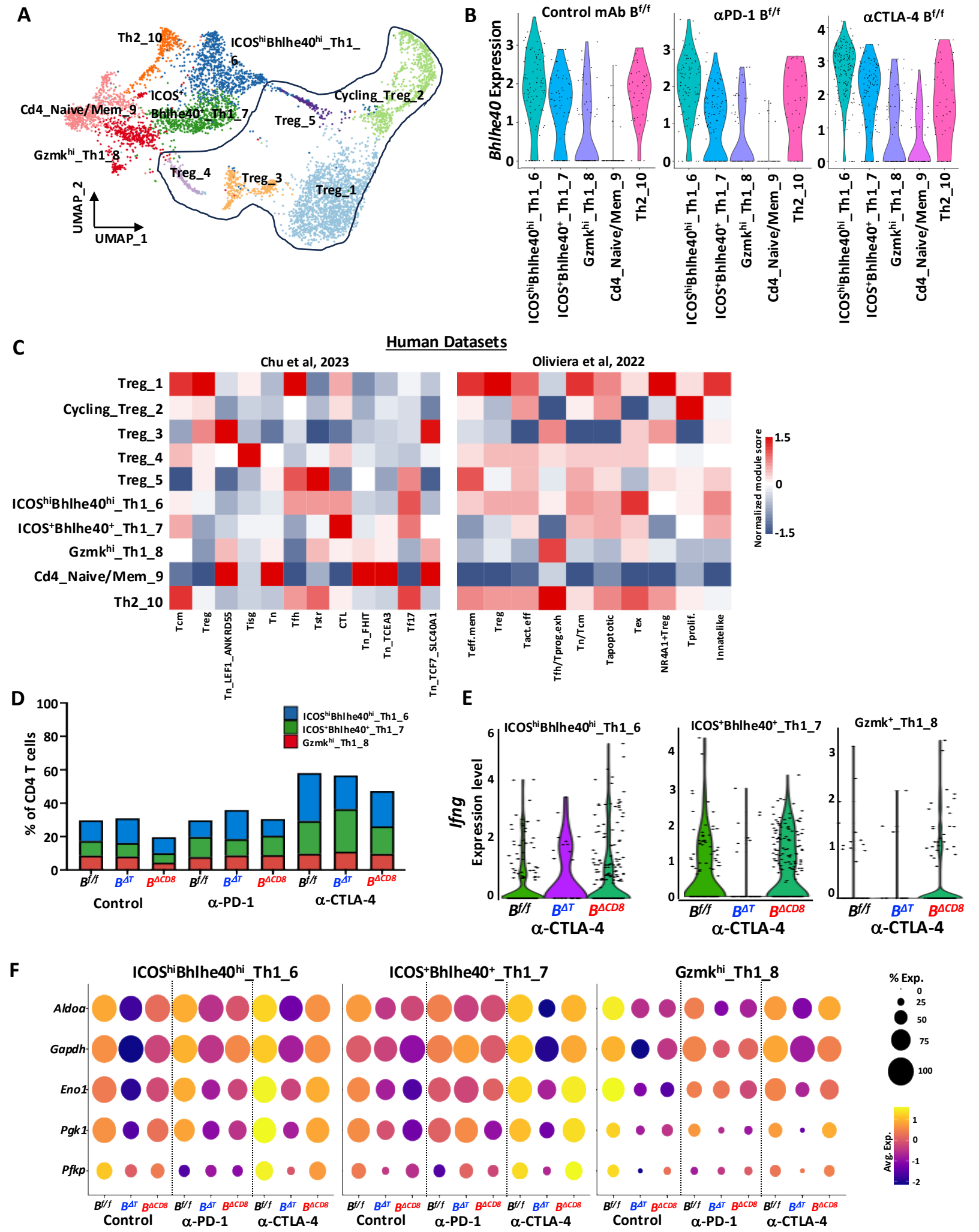
A
Th2_10
ICOS^hiBhlhe40^hi_Th1_6
ICOS+ Bhlhe40+_Th1_7
Cd4_Naive/Mem_9
Gzmk^hi_Th1_8
Cycling_Treg_2
Treg_5
Treg_4
Treg_3
Treg_1
UMAP_2
UMAP_1
B
Control mAb B^f/f
αPD-1 B^f/f
αCTLA-4 B^f/f
Bhlhe40 Expression
ICOS^hiBhlhe40^hi_Th1_6
ICOS+Bhlhe40+_Th1_7
Gzmk^hi_Th1_8
Cd4_Naive/Mem_9
Th2_10
C
Human Datasets
Chu et al, 2023
Oliviera et al, 2022
Treg_1
Cycling_Treg_2
Treg_3
Treg_4
Treg_5
ICOS^hiBhlhe40^hi_Th1_6
ICOS+Bhlhe40+_Th1_7
Gzmk^hi_Th1_8
Cd4_Naive/Mem_9
Th2_10
Tcm
Treg
Tn_LEF1_ANKRD55
Tisg
Tn
Tfh
Tstr
CTL
Tn_FHIT
Tn_TCEA3
Tf17
Tn_TCF7_SLC40A1
Teff.mem
Treg
Tact.eff
Tfh/Tprog.exh
Tn/Tcm
Tapoptotic
Tex
NR4A1+Treg
Tprolif.
Innatelike
Normalized module score
1.5
0
-1.5
D
% of CD4 T cells
ICOS^hiBhlhe40^hi_Th1_6
ICOS+Bhlhe40+_Th1_7
Gzmk^hi_Th1_8
B^f/f
B^ΔT
B^ΔCD8
Control
α-PD-1
α-CTLA-4
E
Ifng Expression level
ICOS^hiBhlhe40^hi_Th1_6
ICOS+Bhlhe40+_Th1_7
Gzmk+_Th1_8
B^f/f
B^ΔT
B^ΔCD8
α-CTLA-4
F
ICOS^hiBhlhe40^hi_Th1_6
ICOS+Bhlhe40+_Th1_7
Gzmk^hi_Th1_8
Aldoa
Gapdh
Eno1
Pgk1
Pfkp
Control
α-PD-1
α-CTLA-4
% Exp.
0
25
50
75
100
Avg. Exp.
1
0
-1
-2

Figure 7

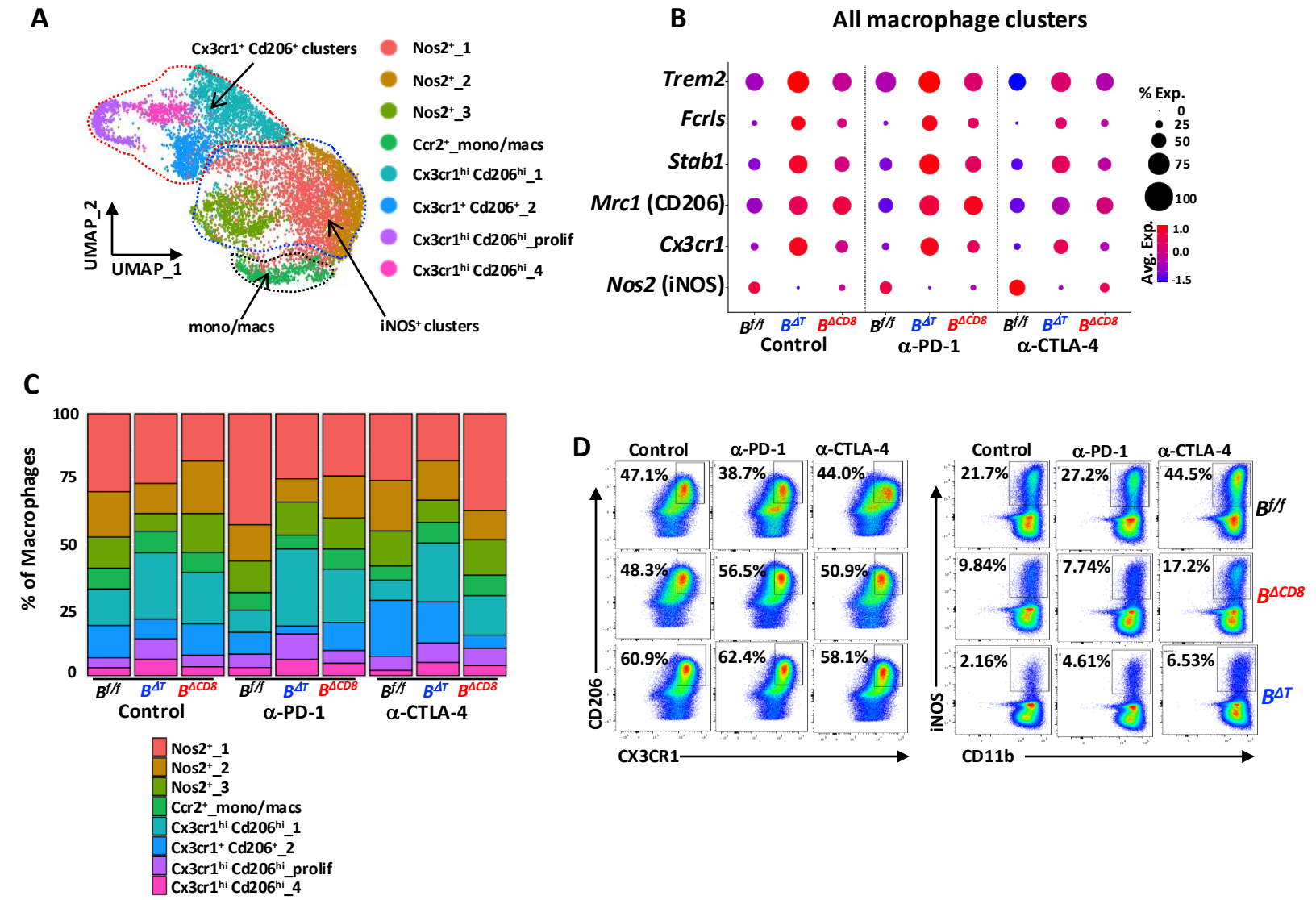
A
Cx3cr1+ Cd206+ clusters
Nos2+_1
Nos2+_2
Nos2+_3
Ccr2+_mono/macs
Cx3cr1hi Cd206hi_1
Cx3cr1+ Cd206+_2
Cx3cr1hi Cd206hi_prolif
Cx3cr1hi Cd206hi_4
UMAP_2
UMAP_1
mono/macs
iNOS+ clusters
B
All macrophage clusters
Trem2
Fcrls
Stab1
Mrc1 (CD206)
Cx3cr1
Nos2 (iNOS)
% Exp.
0
25
50
75
100
Avg. Exp.
1.0
0.0
-1.5
Bf/f
BΔT
BΔCD8
Control
α-PD-1
α-CTLA-4
C
% of Macrophages
100
75
50
25
0
Nos2+_1
Nos2+_2
Nos2+_3
Ccr2+_mono/macs
Cx3cr1hi Cd206hi_1
Cx3cr1+ Cd206+_2
Cx3cr1hi Cd206hi_prolif
Cx3cr1hi Cd206hi_4
D
Control
α-PD-1
α-CTLA-4
47.1%
38.7%
44.0%
48.3%
56.5%
50.9%
60.9%
62.4%
58.1%
21.7%
27.2%
44.5%
9.84%
7.74%
17.2%
2.16%
4.61%
6.53%
CD206
CX3CR1
iNOS
CD11b

Suppl. Figure 1

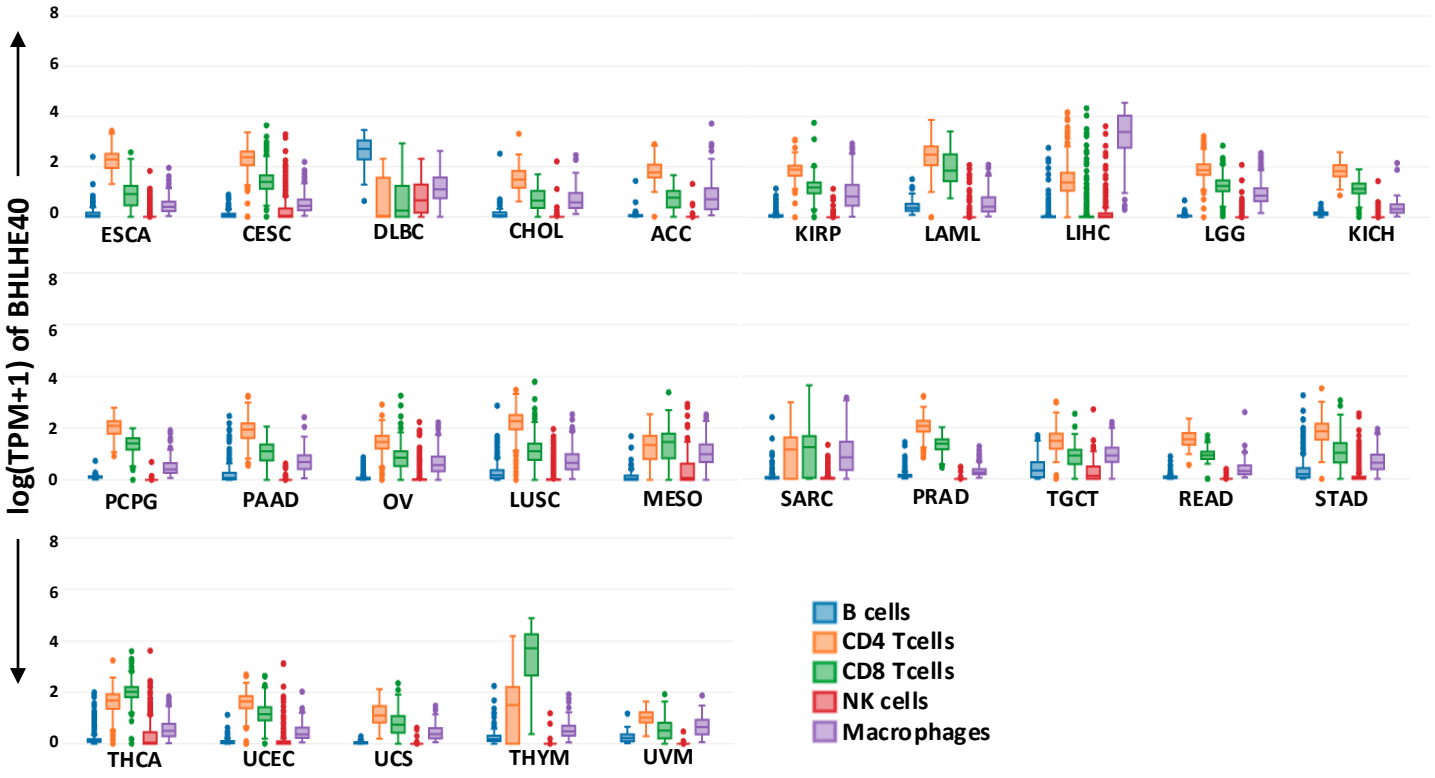

Suppl. Figure 2

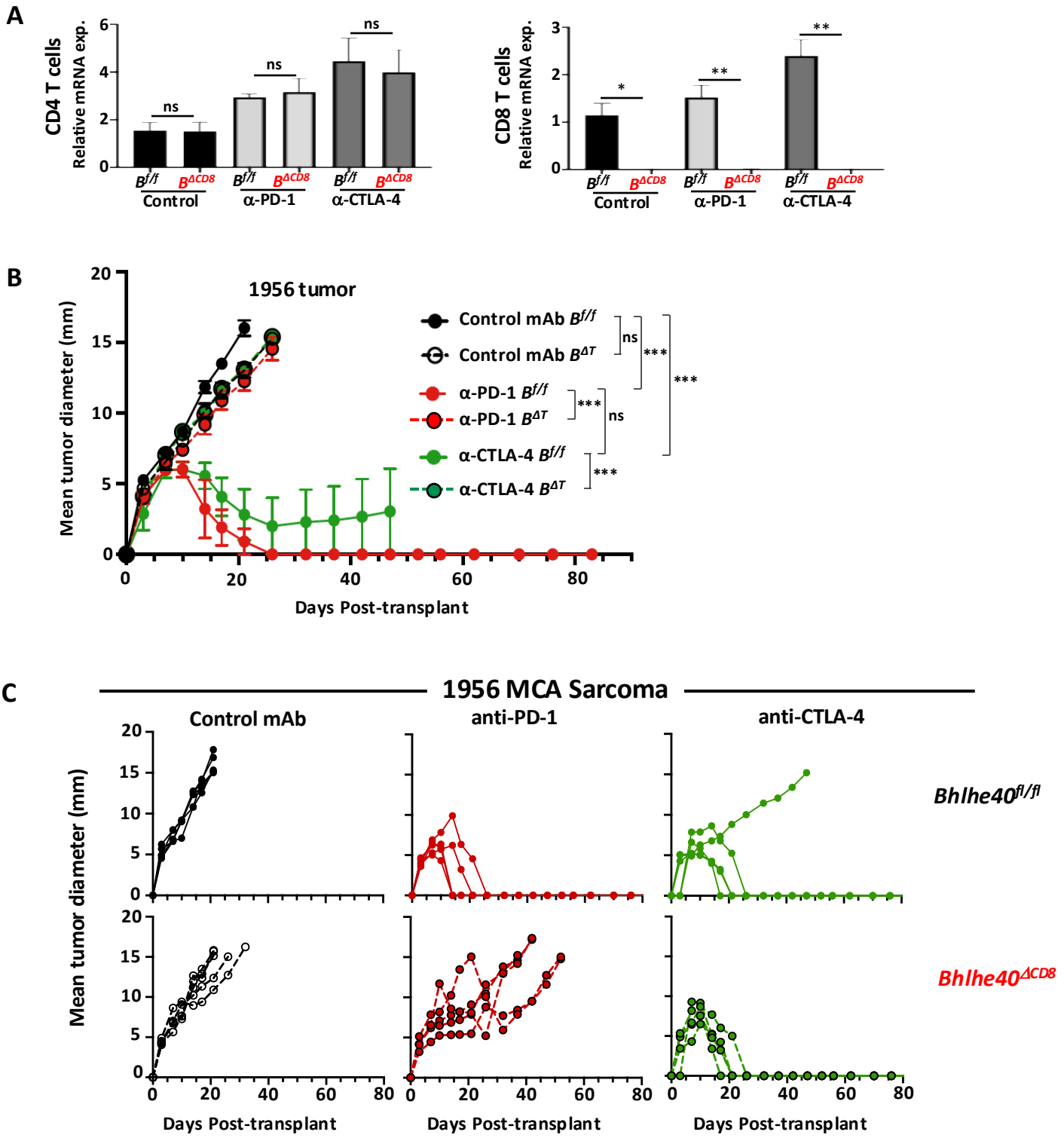

Suppl. Figure 3

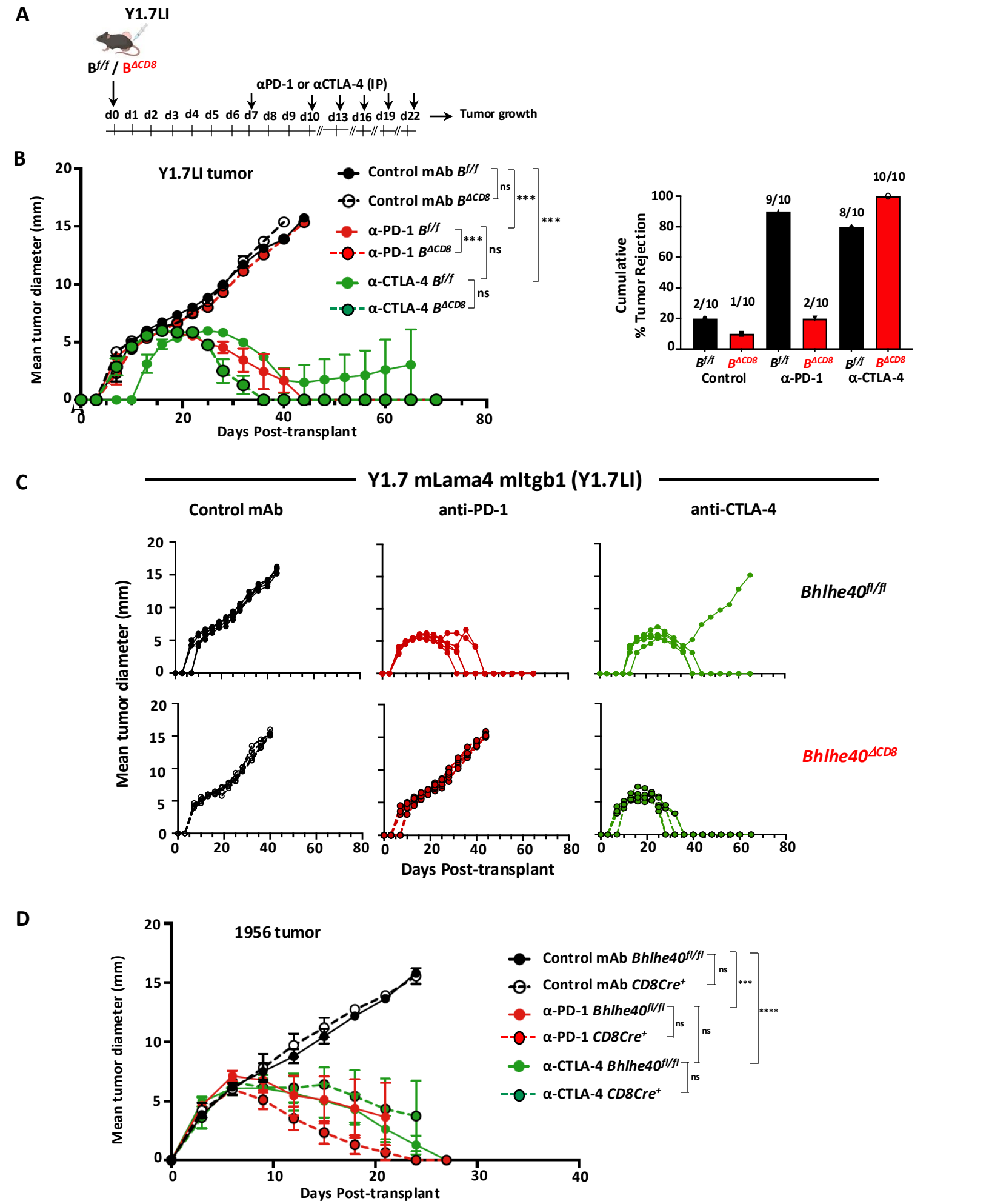

Suppl. Figure 4

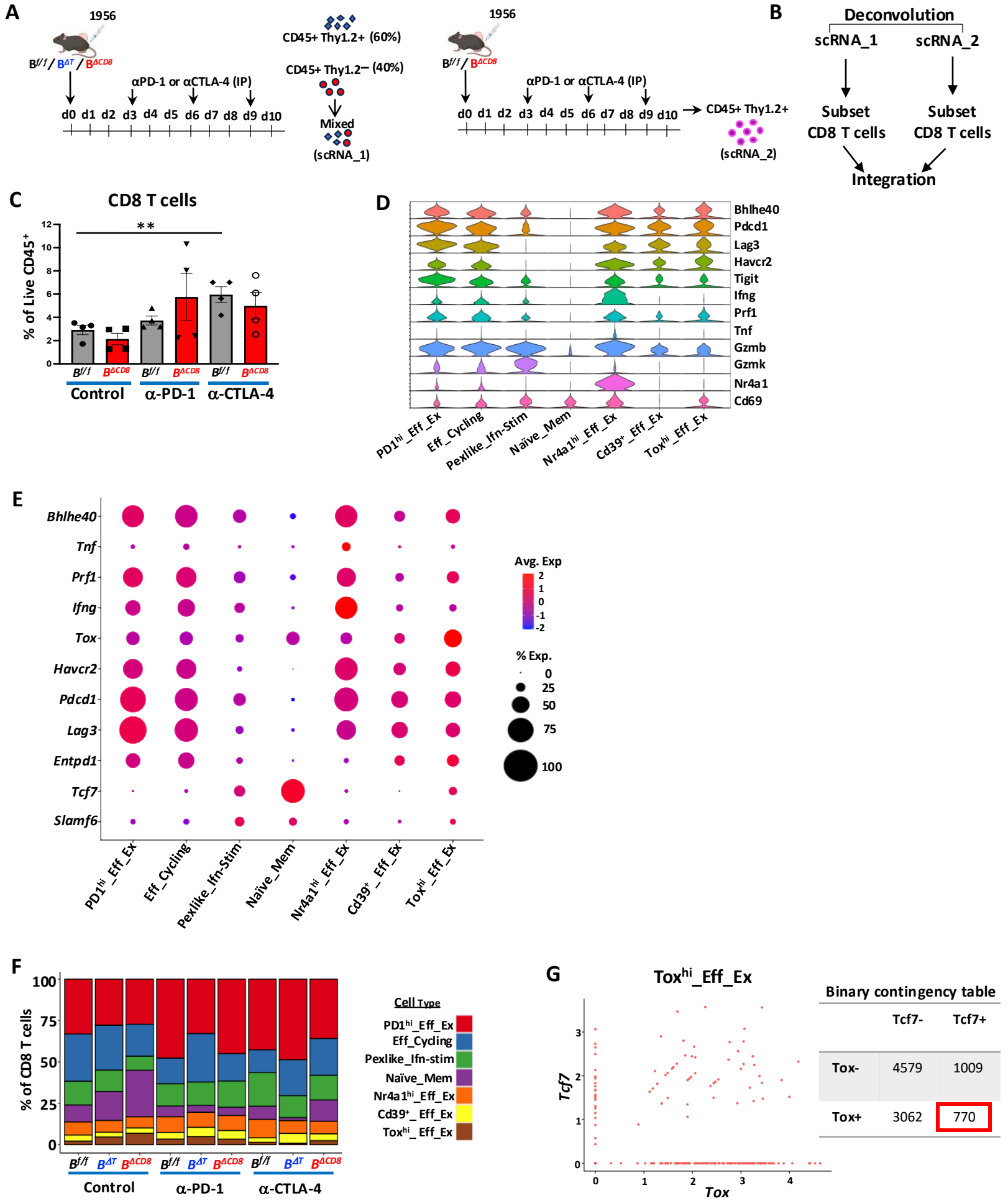

Suppl. Figure 5

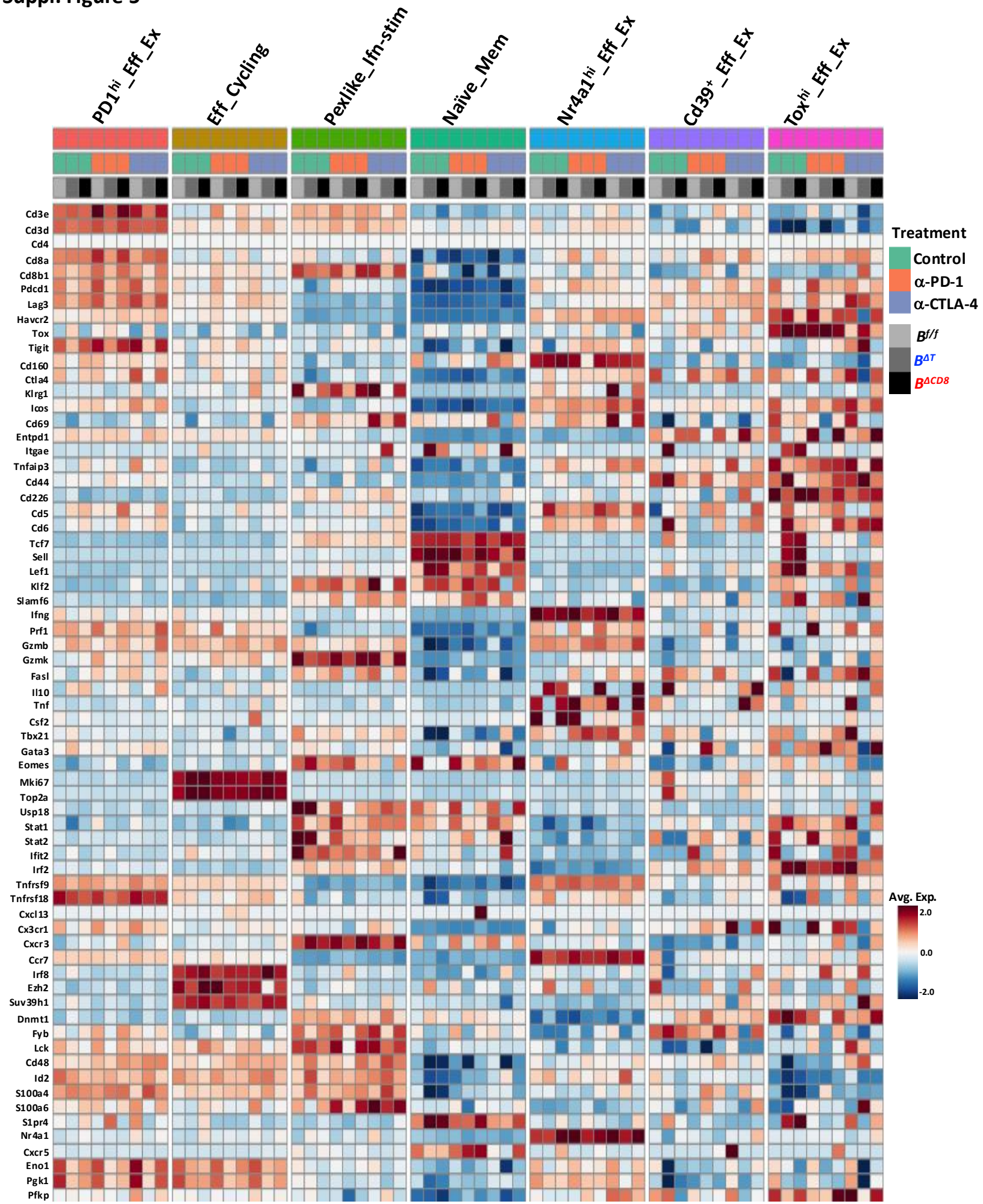

Suppl. Figure 6

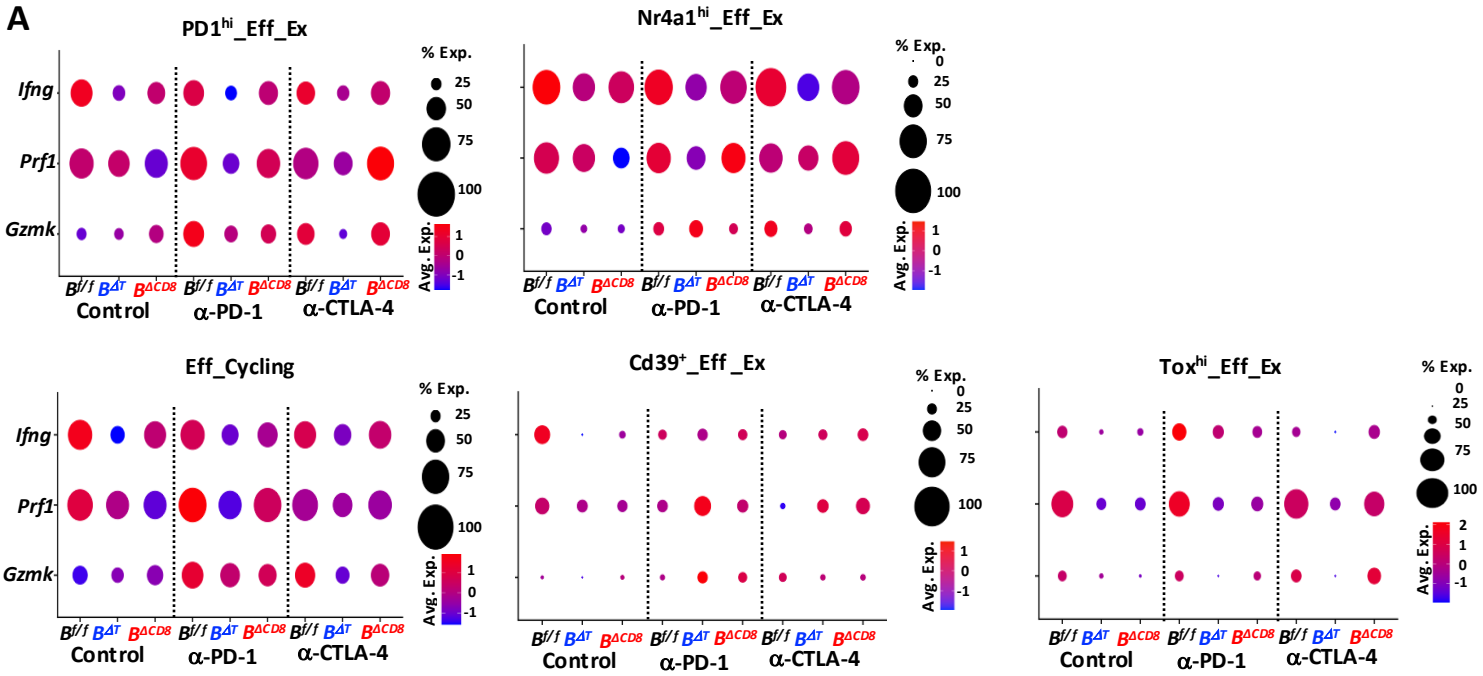

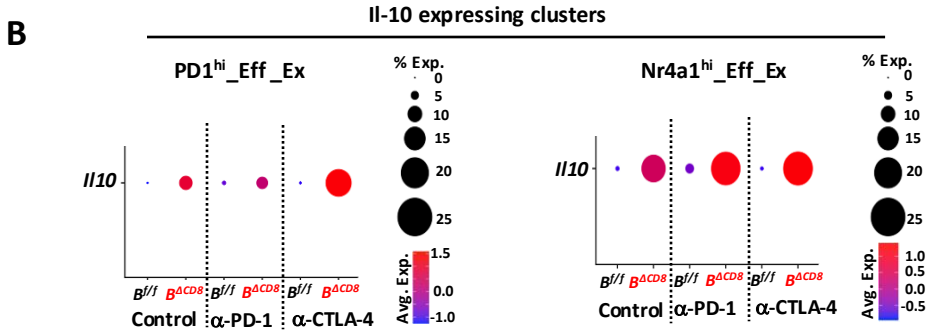

Suppl. Figure 7

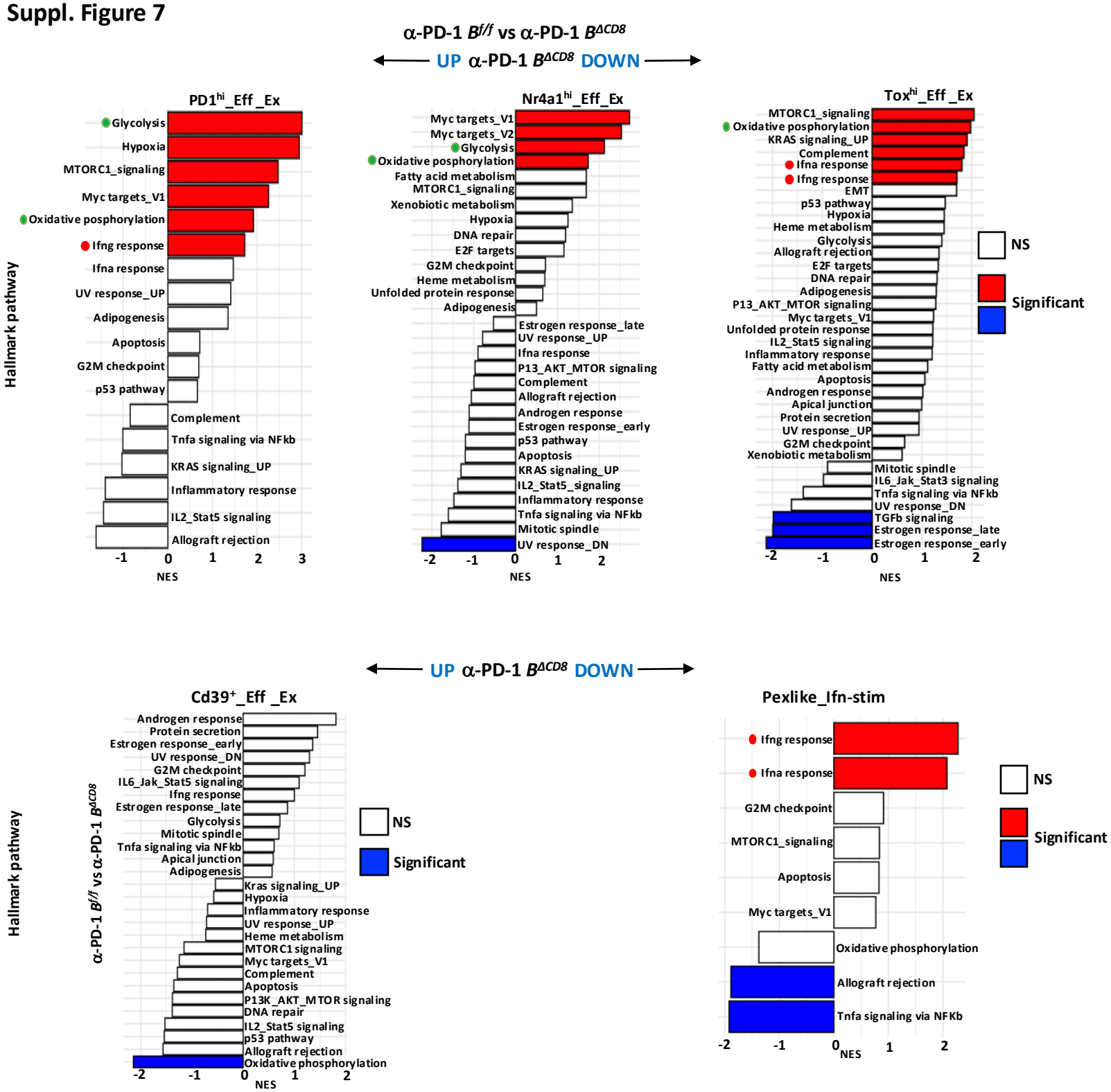

Suppl. Figure 8

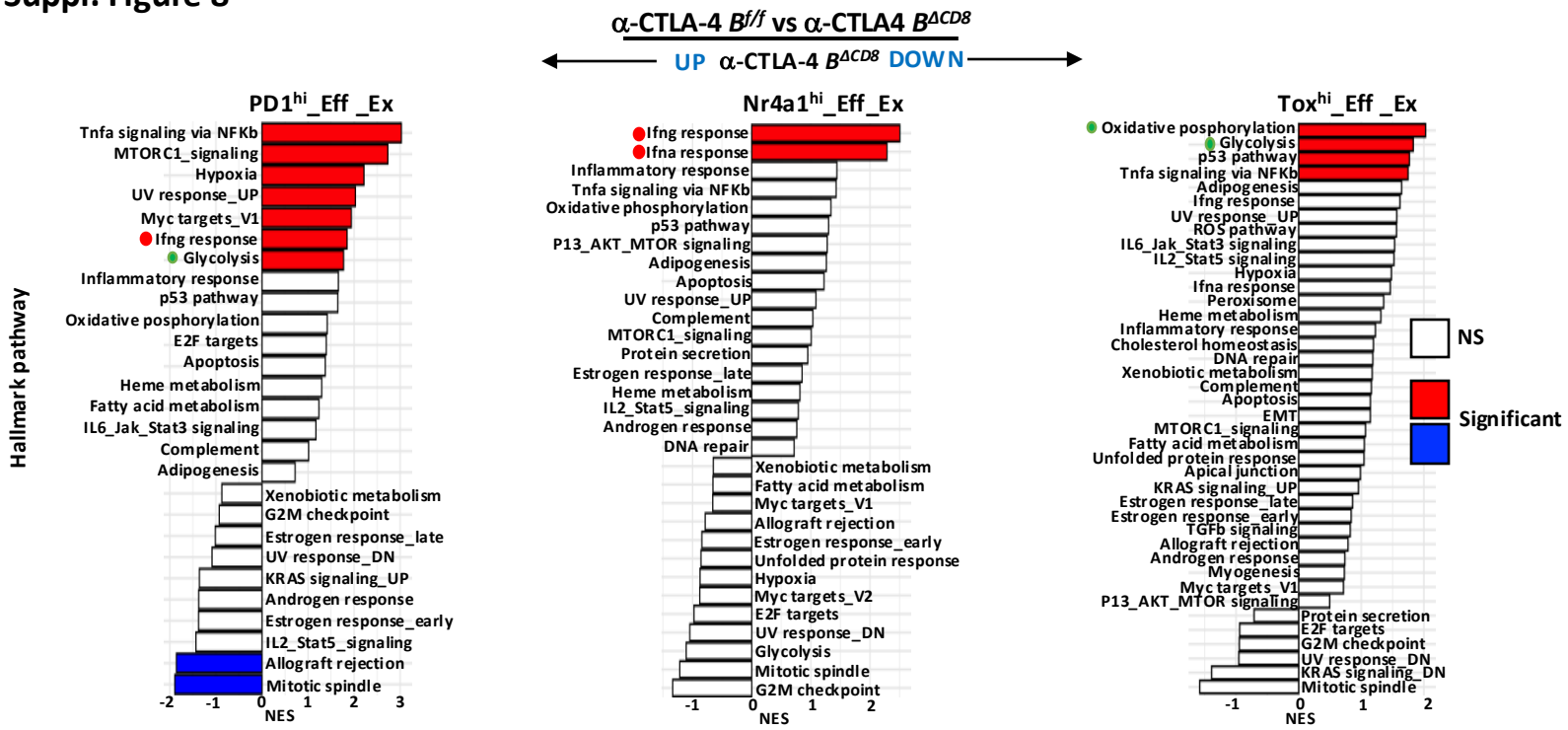

Suppl. Figure 9

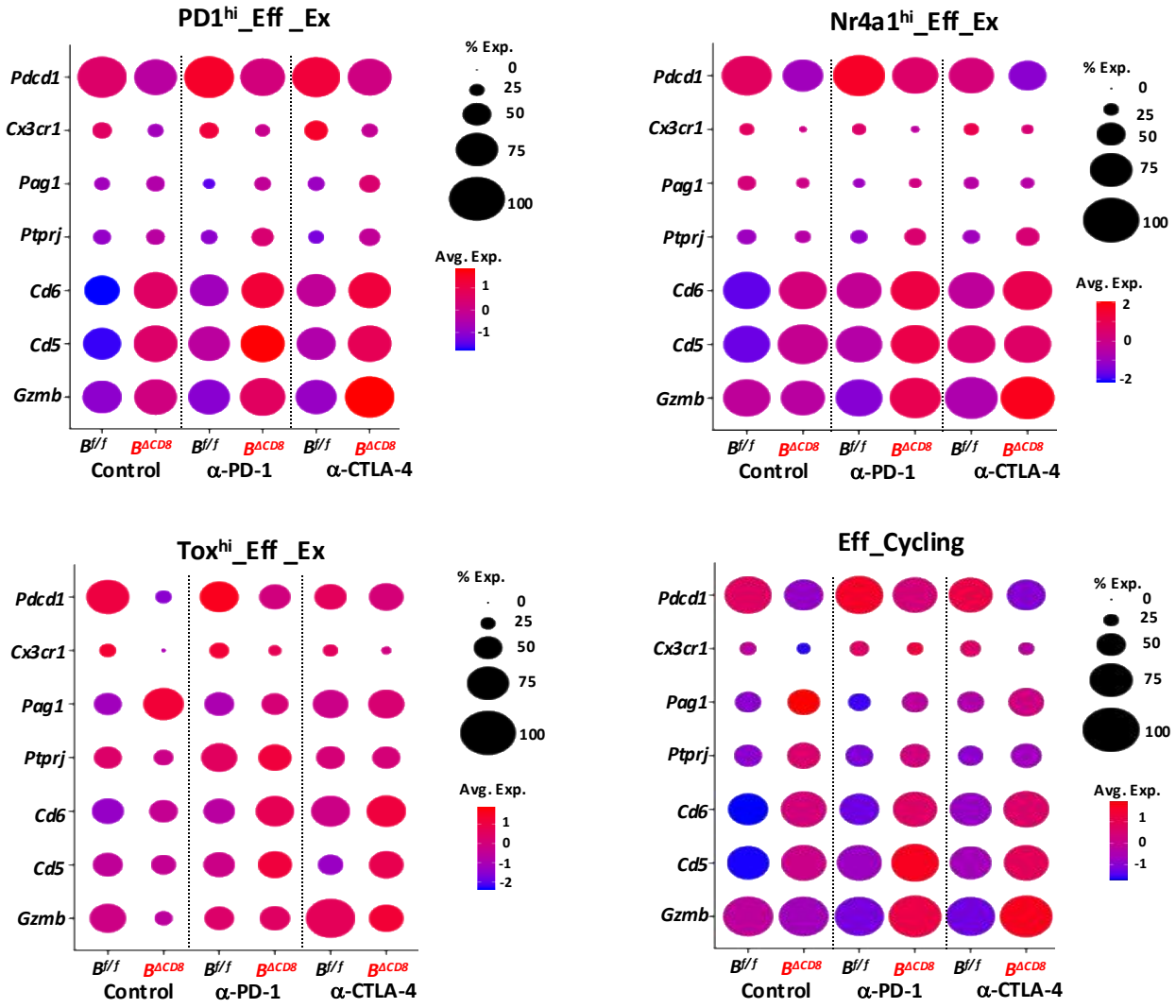

Suppl. Figure 10

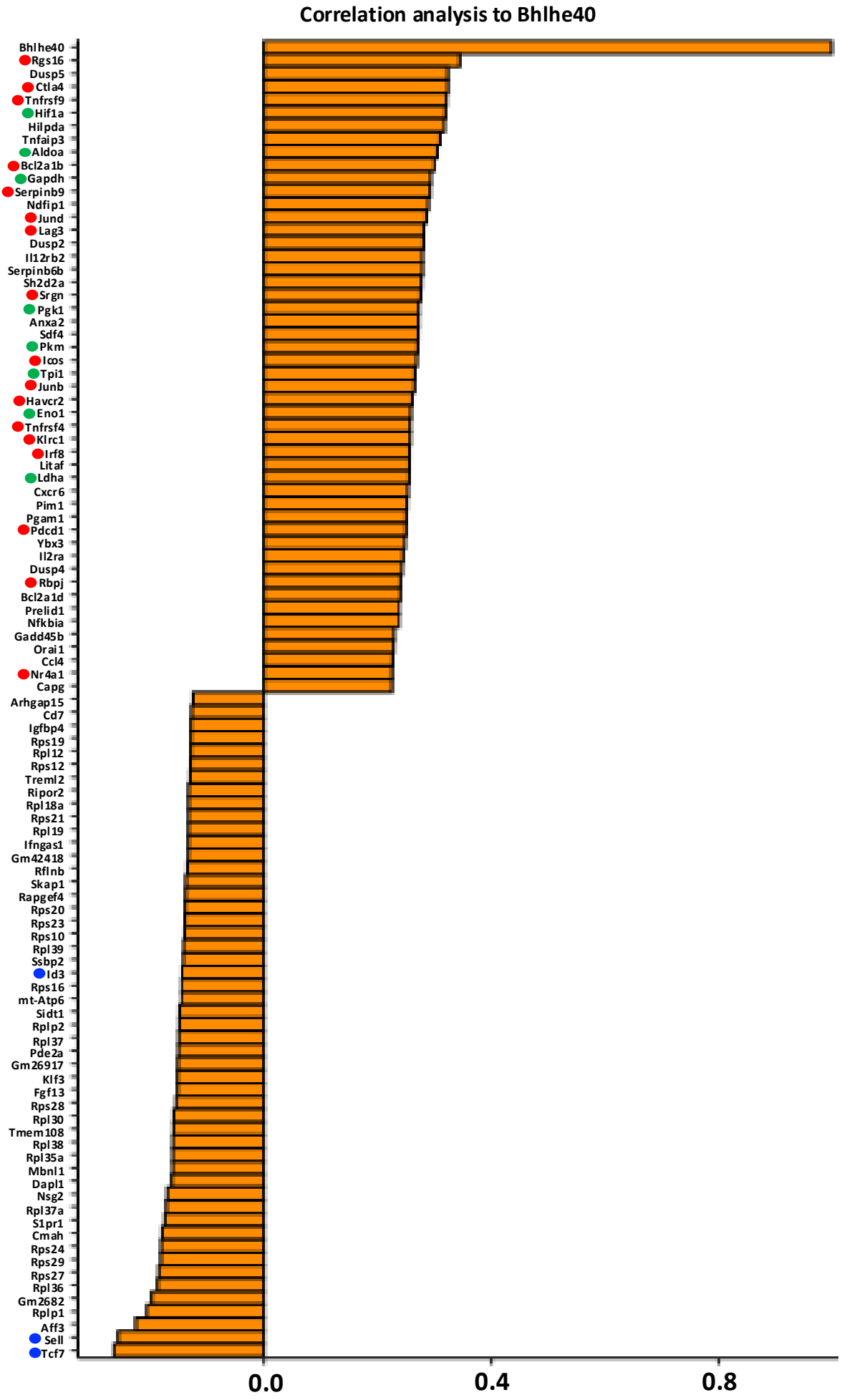

Suppl. Figure 11

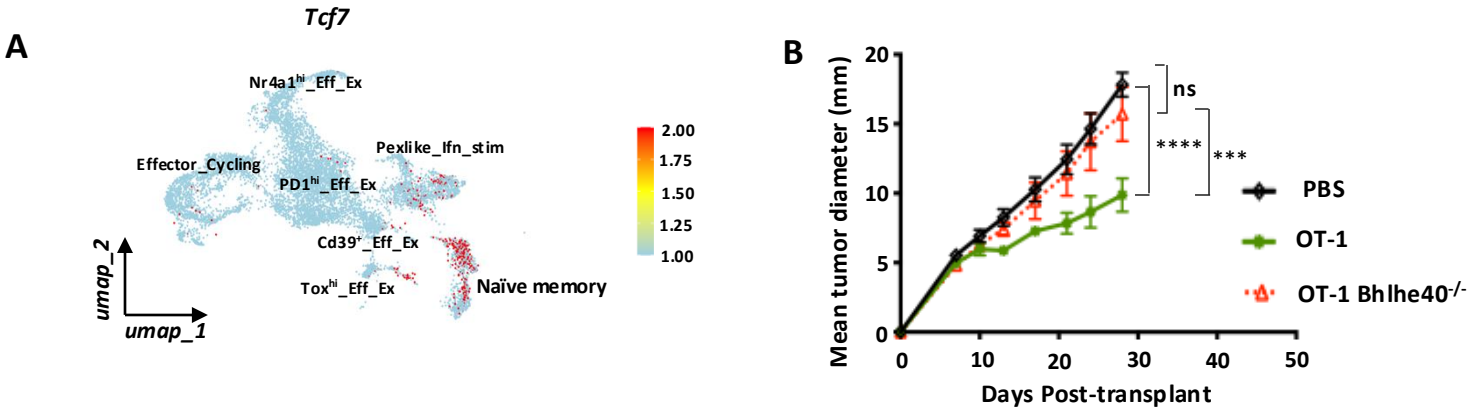

Suppl. Figure 12

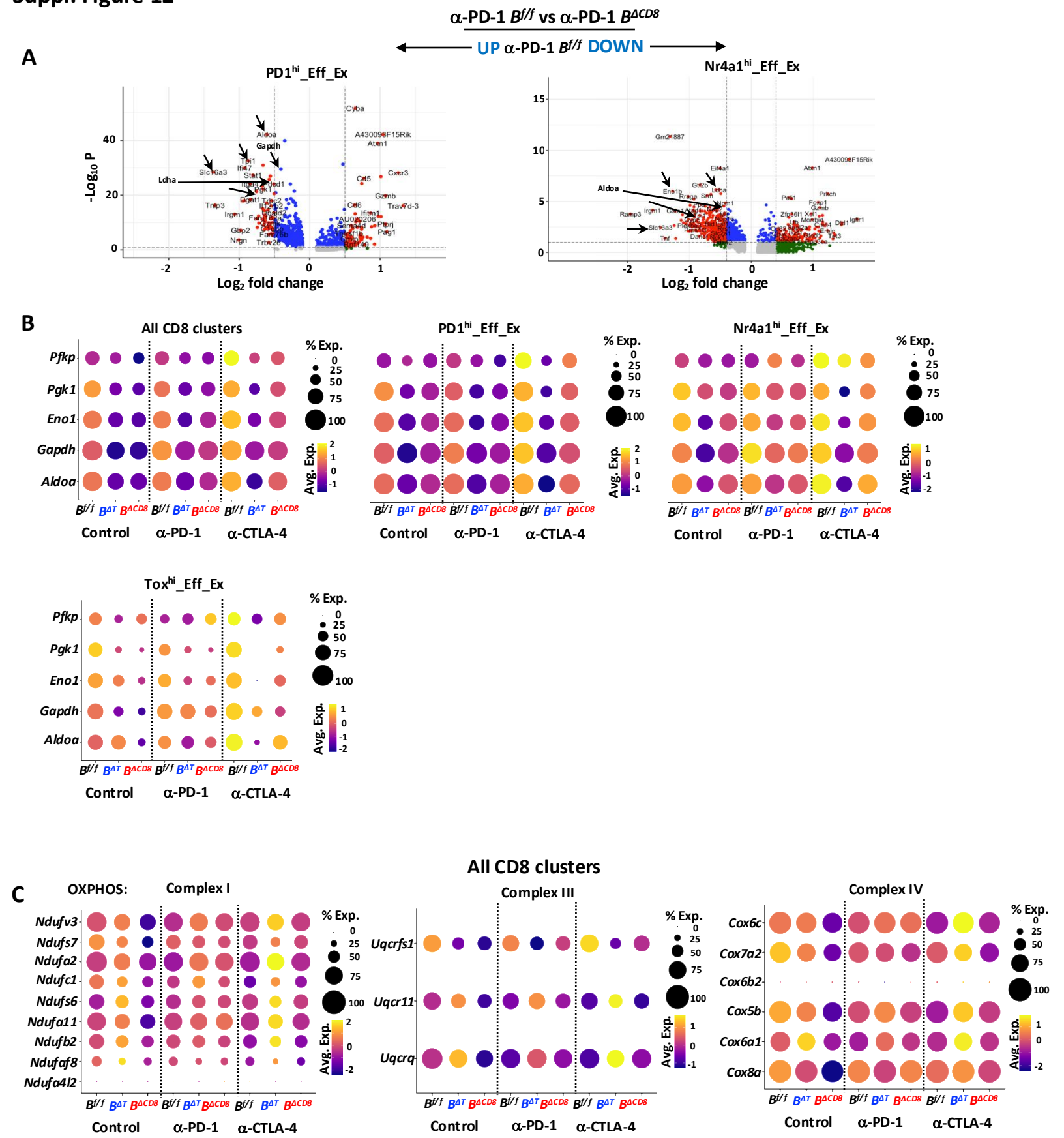

Figure S13

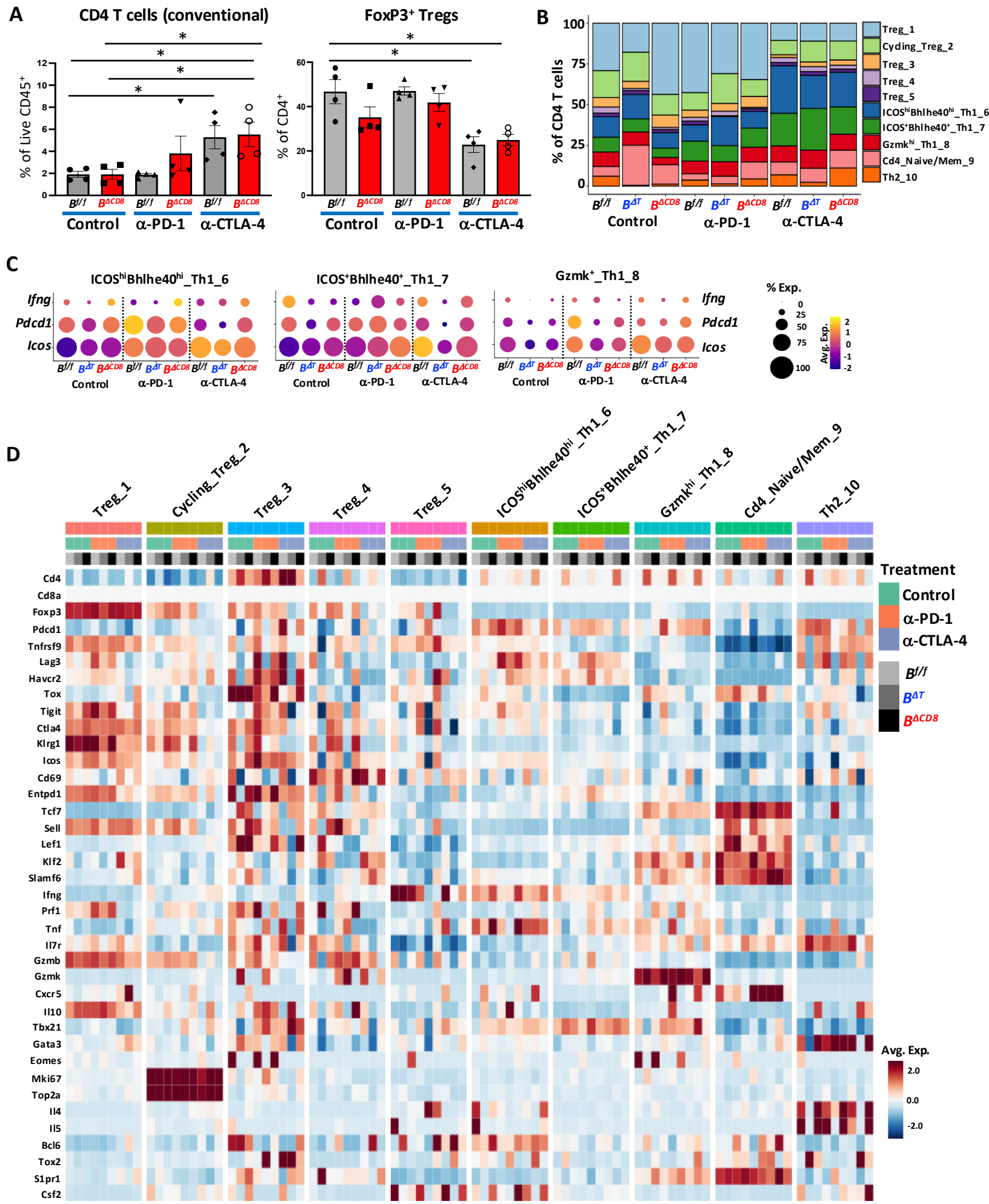
A
CD4 T cells (conventional)
FoxP3+ Tregs
% of Live CD45+
% of CD4+
Control
α-PD-1
α-CTLA-4
B
% of CD4 T cells
Treg_1
Cycling_Treg_2
Treg_3
Treg_4
Treg_5
ICOShiBhlhe40hi_Th1_6
ICOS+Bhlhe40+_Th1_7
Gzmkhi_Th1_8
Cd4_Naive/Mem_9
Th2_10
C
ICOShiBhlhe40hi_Th1_6
ICOS+Bhlhe40+_Th1_7
Gzmk+_Th1_8
Ifng
Pdcd1
Icos
% Exp.
Avg. Exp.
D
Treg_1
Cycling_Treg_2
Treg_3
Treg_4
Treg_5
ICOShiBhlhe40hi_Th1_6
ICOS+Bhlhe40+_Th1_7
Gzmkhi_Th1_8
Cd4_Naive/Mem_9
Th2_10
Cd4
Cd8a
Foxp3
Pdcd1
Tnfrsf9
Lag3
Havcr2
Tox
Tigit
Ctla4
Klrg1
Icos
Cd69
Entpd1
Tcf7
Sell
Lef1
Klf2
Slamf6
Ifng
Prf1
Tnf
Il7r
Gzmb
Gzmk
Cxcr5
Il10
Tbx21
Gata3
Eomes
Mki67
Top2a
Il4
Il5
Bcl6
Tox2
S1pr1
Csf2
Treatment
Control
α-PD-1
α-CTLA-4
Avg. Exp.

Figure 1

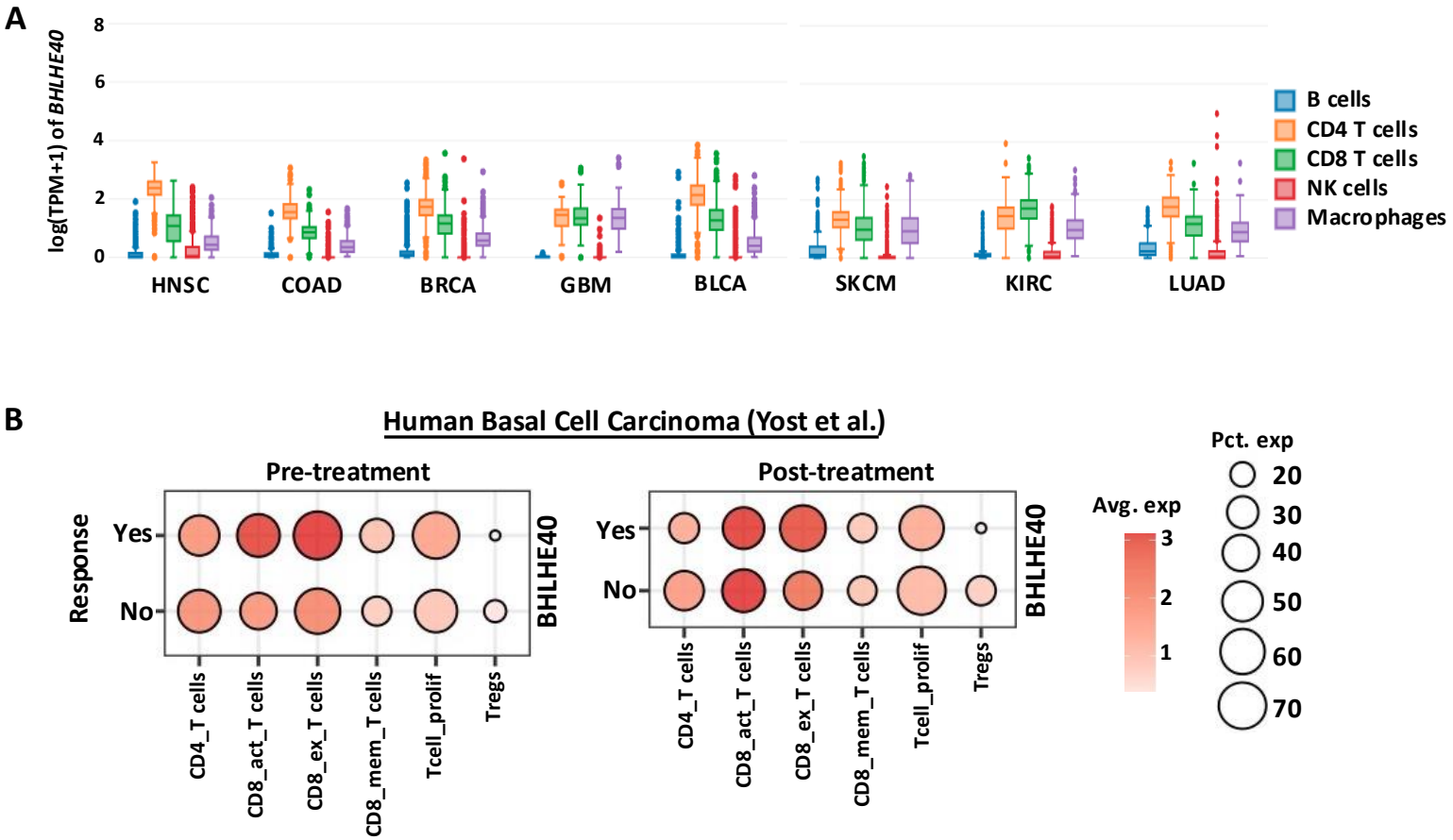
A
log(TPM+1) of BHLHE40
8
6
4
2
0
HNSC
COAD
BRCA
GBM
BLCA
SKCM
KIRC
LUAD
B cells
CD4 T cells
CD8 T cells
NK cells
Macrophages
B
Human Basal Cell Carcinoma (Yost et al.)
Pre-treatment
Post-treatment
Response
Yes
No
BHLHE40
CD4_T cells
CD8_act_T cells
CD8_ex_T cells
CD8_mem_T cells
Tcell_prolif
Tregs
Avg. exp
3
2
1
Pct. exp
20
30
40
50
60
70

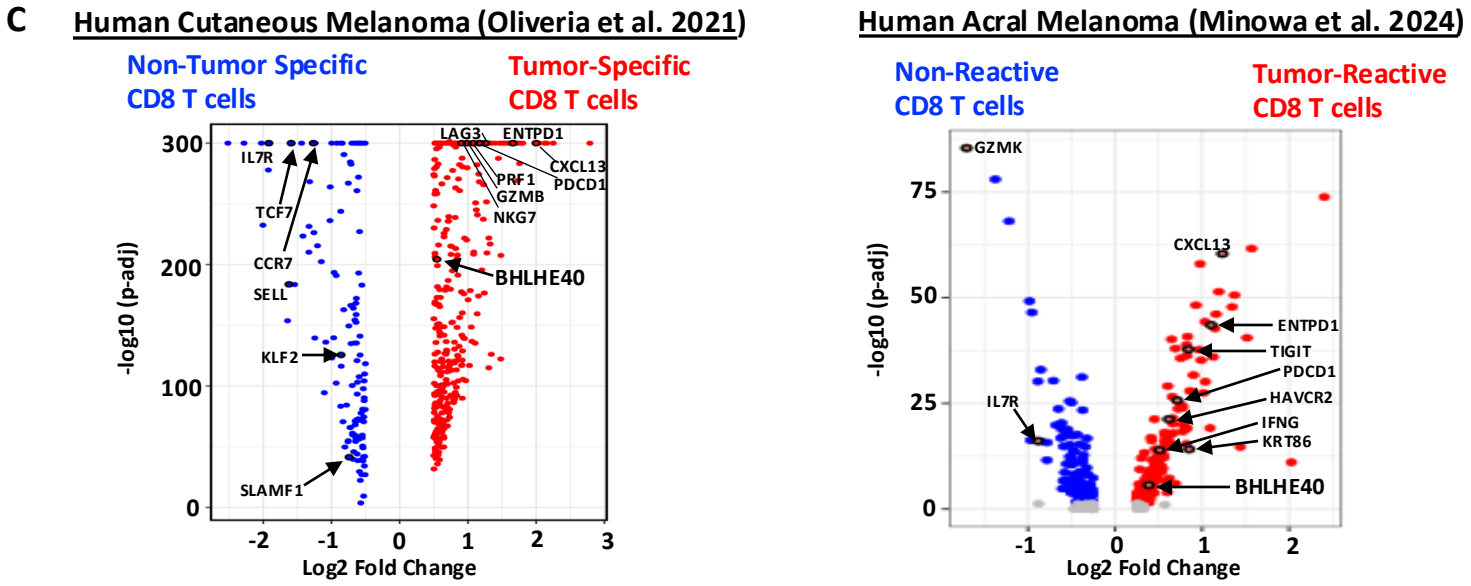
C
Human Cutaneous Melanoma (Oliveria et al. 2021)
Non-Tumor Specific CD8 T cells
Tumor-Specific CD8 T cells
-log10 (p-adj)
Log2 Fold Change
IL7R
TCF7
CCR7
SELL
KLF2
SLAMF1
LAG3
ENTPD1
CXCL13
PDCD1
PRF1
GZMB
NKG7
BHLHE40
Human Acral Melanoma (Minowa et al. 2024)
Non-Reactive CD8 T cells
Tumor-Reactive CD8 T cells
GZMK
CXCL13
ENTPD1
TIGIT
PDCD1
HAVCR2
IFNG
KRT86
IL7R
BHLHE40

Figure 2

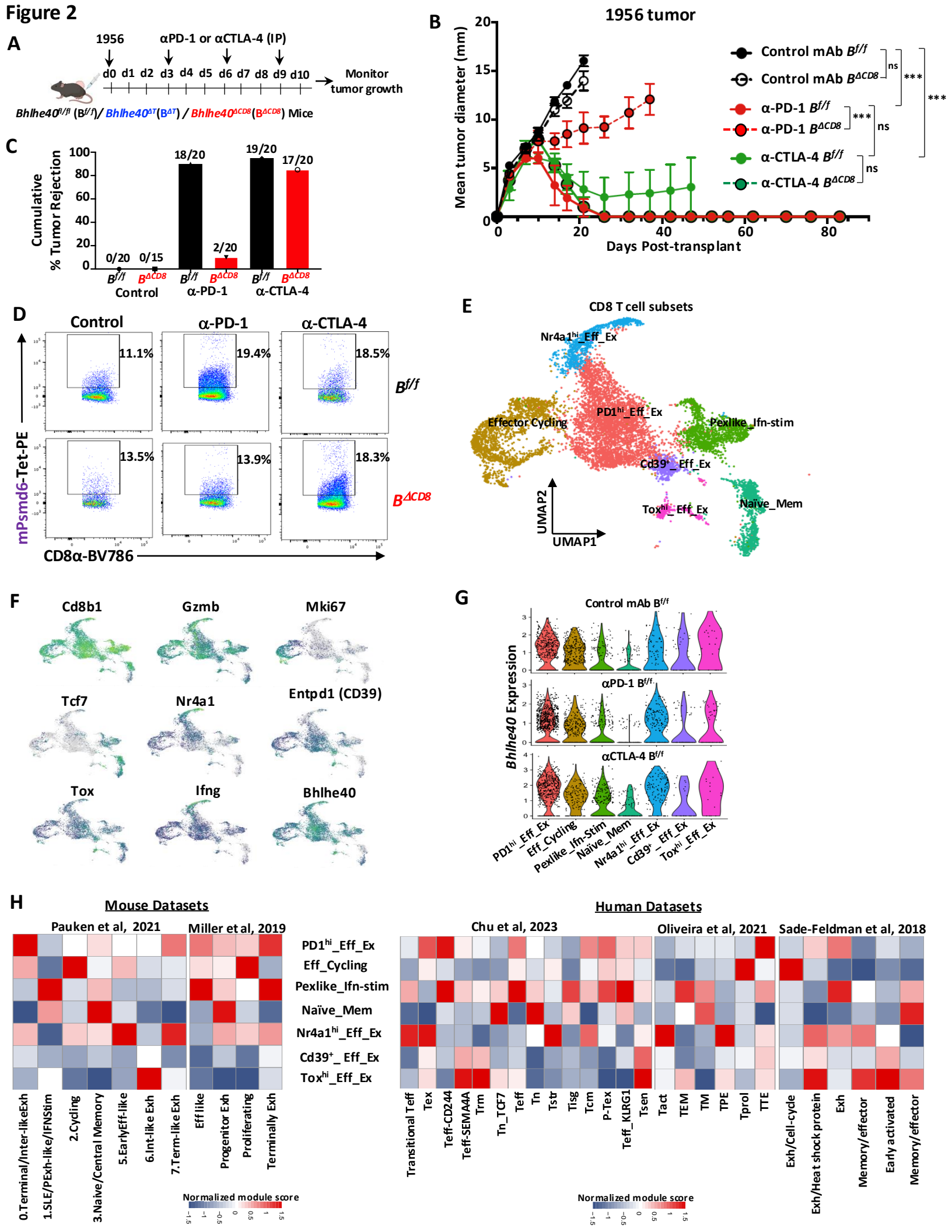
A
1956
αPD-1 or αCTLA-4 (IP)
d0 d1 d2 d3 d4 d5 d6 d7 d8 d9 d10
Monitor tumor growth
Bhlhe40f/fl (Bf/f)/ Bhlhe40ΔT(BΔT) / Bhlhe40ΔCD8(BΔCD8) Mice
B
1956 tumor
Mean tumor diameter (mm)
Days Post-transplant
Control mAb Bf/f
Control mAb BΔCD8
α-PD-1 Bf/f
α-PD-1 BΔCD8
α-CTLA-4 Bf/f
α-CTLA-4 BΔCD8
ns
***
C
Cumulative % Tumor Rejection
0/20
0/15
18/20
2/20
19/20
17/20
Control
α-PD-1
α-CTLA-4
D
Control
α-PD-1
α-CTLA-4
11.1%
19.4%
18.5%
13.5%
13.9%
18.3%
Bf/f
BΔCD8
mPsmd6-Tet-PE
CD8α-BV786
E
CD8 T cell subsets
Nr4a1hi_Eff_Ex
PD1hi_Eff_Ex
Effector Cycling
Pexlike_Ifn-stim
Cd39+_Eff_Ex
Toxhi_Eff_Ex
Naïve_Mem
UMAP2
UMAP1
F
Cd8b1
Gzmb
Mki67
Tcf7
Nr4a1
Entpd1 (CD39)
Tox
Ifng
Bhlhe40
G
Control mAb Bf/f
αPD-1 Bf/f
αCTLA-4 Bf/f
Bhlhe40 Expression
PD1hi_Eff_Ex
Eff_Cycling
Pexlike_Ifn-stim
Naïve_Mem
Nr4a1hi_Eff_Ex
Cd39+_Eff_Ex
Toxhi_Eff_Ex
H
Mouse Datasets
Pauken et al, 2021
Miller et al, 2019
PD1hi_Eff_Ex
Eff_Cycling
Pexlike_Ifn-stim
Naïve_Mem
Nr4a1hi_Eff_Ex
Cd39+_ Eff_Ex
Toxhi_Eff_Ex
0.Terminal/Inter-likeExh
1.SLE/PExh-like/IFNStim
2.Cycling
3.Naive/Central Memory
5.EarlyEff-like
6.Int-like Exh
7.Term-like Exh
Eff like
Progenitor Exh
Proliferating
Terminally Exh
Normalized module score
Human Datasets
Chu et al, 2023
Oliveira et al, 2021
Sade-Feldman et al, 2018
Transitional Teff
Tex
Teff-CD244
Teff-SEMA4A
Trm
Tn_TCF7
Teff
Tn
Tstr
Tisg
Tcm
P-Tex
Teff_KLRG1
Tsen
Tact
TEM
TM
TPE
Tprol
TTE
Exh/Cell-cycle
Exh/Heat shock protein
Exh
Memory/effector
Early activated
Memory/effector
Normalized module score

Figure 3

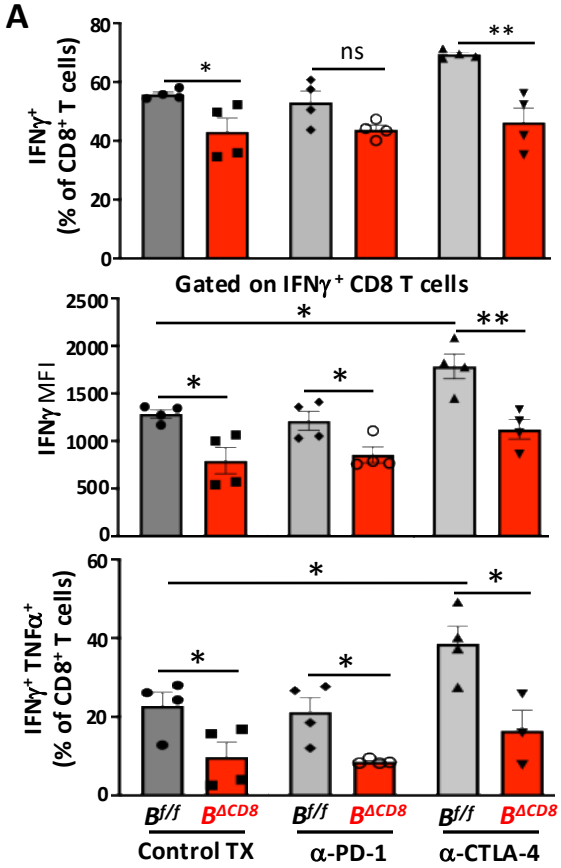
A
IFNγ+ (% of CD8+ T cells)
Gated on IFNγ+ CD8 T cells
IFNγ MFI
IFNγ+ TNFα+ (% of CD8+ T cells)
Bf/f BΔCD8
Control TX
α-PD-1
α-CTLA-4

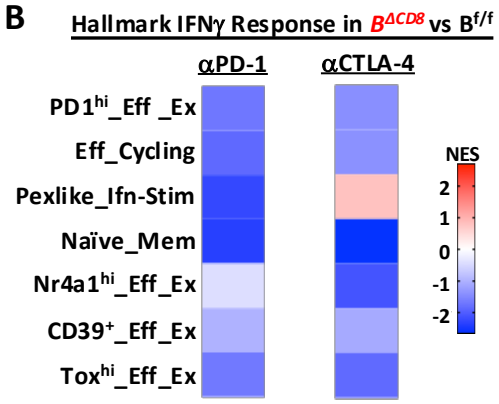
B
Hallmark IFNγ Response in BΔCD8 vs Bf/f
αPD-1
αCTLA-4
PD1hi_Eff _Ex
Eff_Cycling
Pexlike_Ifn-Stim
Naïve_Mem
Nr4a1hi_Eff_Ex
CD39+_Eff_Ex
Toxhi_Eff_Ex
NES

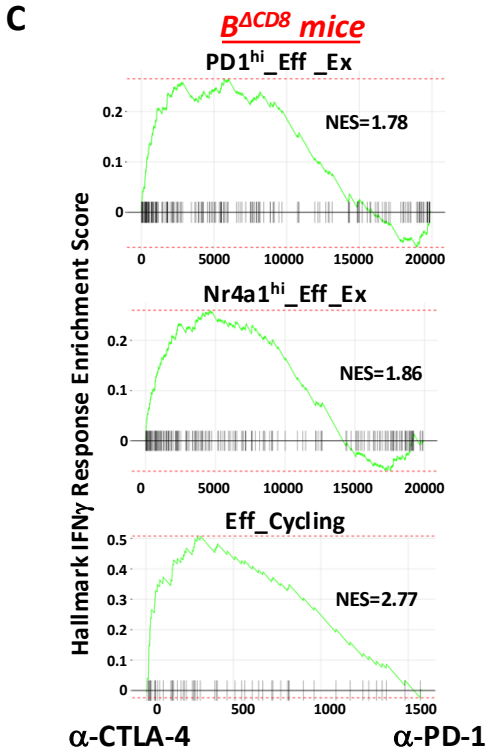
C
BΔCD8 mice
PD1hi_Eff _Ex
NES=1.78
Nr4a1hi_Eff_Ex
NES=1.86
Eff_Cycling
NES=2.77
Hallmark IFNγ Response Enrichment Score
α-CTLA-4
α-PD-1

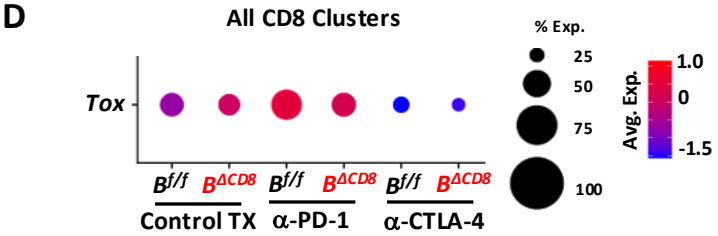
D
All CD8 Clusters
Tox
% Exp.
Avg. Exp.
Bf/f BΔCD8
Control TX
α-PD-1
α-CTLA-4

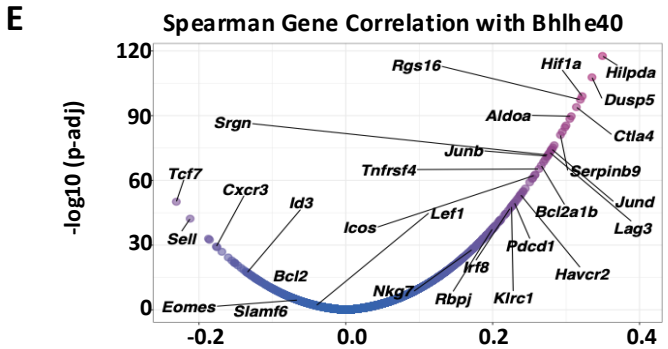
E
Spearman Gene Correlation with Bhlhe40
-log10 (p-adj)
Rgs16
Hif1a
Hilpda
Dusp5
Aldoa
Ctla4
Srgn
Junb
Tnfrsf4
Serpinb9
Tcf7
Cxcr3
Id3
Jund
Bcl2a1b
Lag3
Icos
Lef1
Sell
Pdcd1
Irf8
Havcr2
Bcl2
Nkg7
Rbpj
Klrc1
Eomes
Slamf6

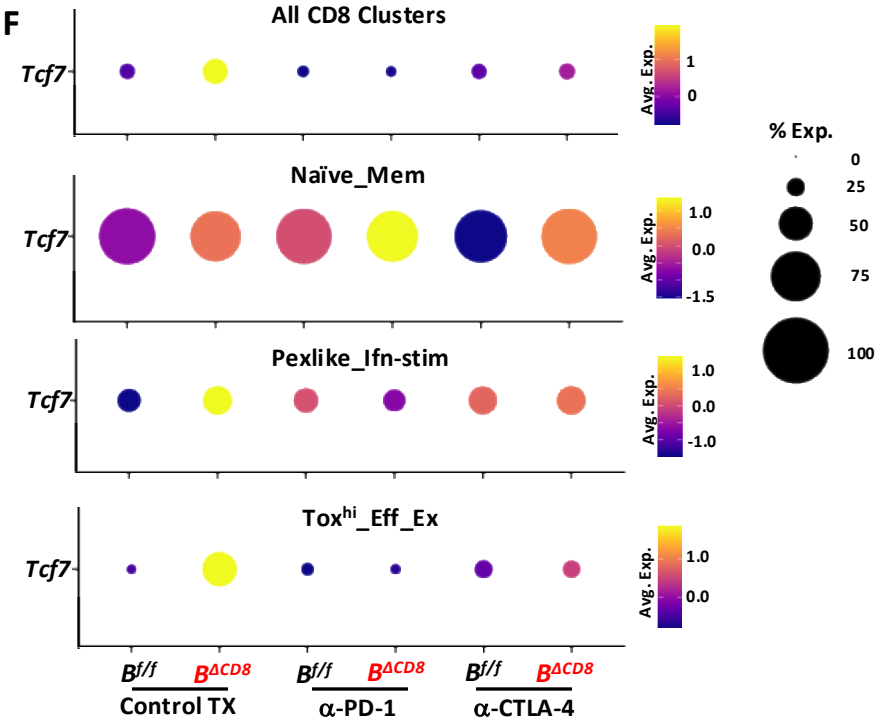
F
All CD8 Clusters
Naïve_Mem
Pexlike_Ifn-stim
Toxhi_Eff_Ex
Tcf7
Avg. Exp.
% Exp.
Bf/f BΔCD8
Control TX
α-PD-1
α-CTLA-4

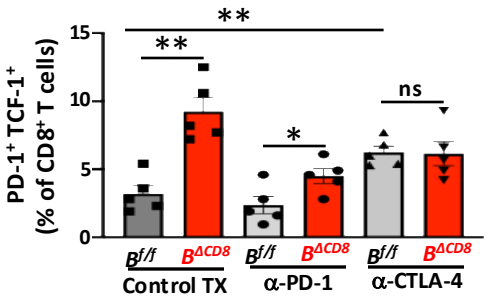
G
PD-1+ TCF-1+ (% of CD8+ T cells)
Bf/f BΔCD8
Control TX
α-PD-1
α-CTLA-4

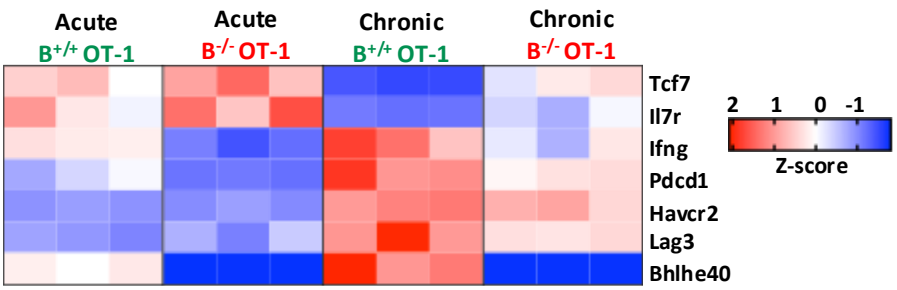
H
Acute B+/+ OT-1
Acute B-/- OT-1
Chronic B+/+ OT-1
Chronic B-/- OT-1
Tcf7
Il7r
Ifng
Pdcd1
Havcr2
Lag3
Bhlhe40
Z-score

Figure 4

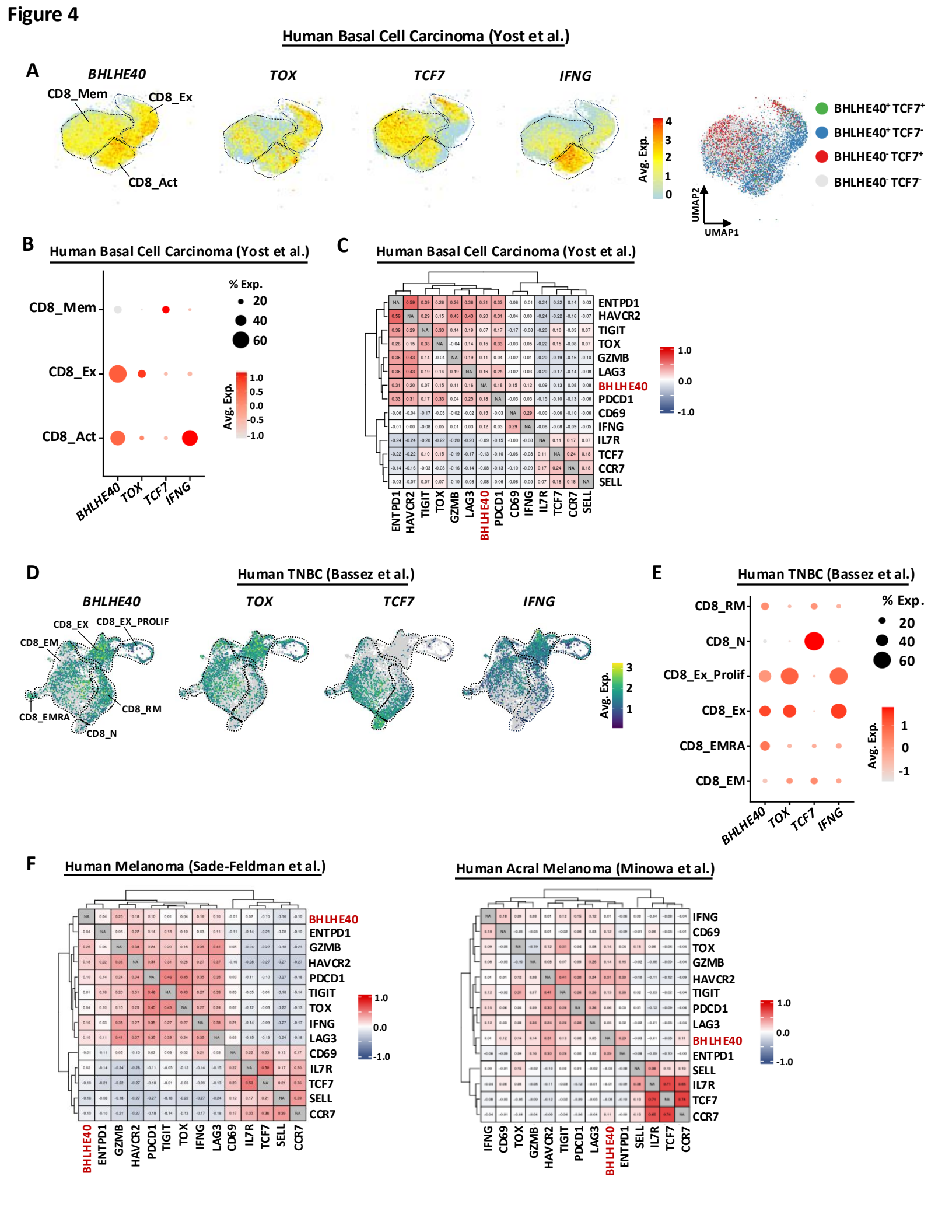
Human Basal Cell Carcinoma (Yost et al.)
A
BHLHE40
TOX
TCF7
IFNG
CD8_Mem
CD8_Ex
CD8_Act
Avg. Exp.
UMAP2
UMAP1
BHLHE40+ TCF7+
BHLHE40+ TCF7-
BHLHE40- TCF7+
BHLHE40- TCF7-
B
Human Basal Cell Carcinoma (Yost et al.)
% Exp.
20
40
60
Avg. Exp.
C
Human Basal Cell Carcinoma (Yost et al.)
ENTPD1
HAVCR2
TIGIT
TOX
GZMB
LAG3
BHLHE40
PDCD1
CD69
IFNG
IL7R
TCF7
CCR7
SELL
D
Human TNBC (Bassez et al.)
CD8_EX
CD8_EX_PROLIF
CD8_EM
CD8_EMRA
CD8_RM
CD8_N
E
Human TNBC (Bassez et al.)
CD8_RM
CD8_N
CD8_Ex_Prolif
CD8_Ex
CD8_EMRA
CD8_EM
F
Human Melanoma (Sade-Feldman et al.)
Human Acral Melanoma (Minowa et al.)

Figure 5

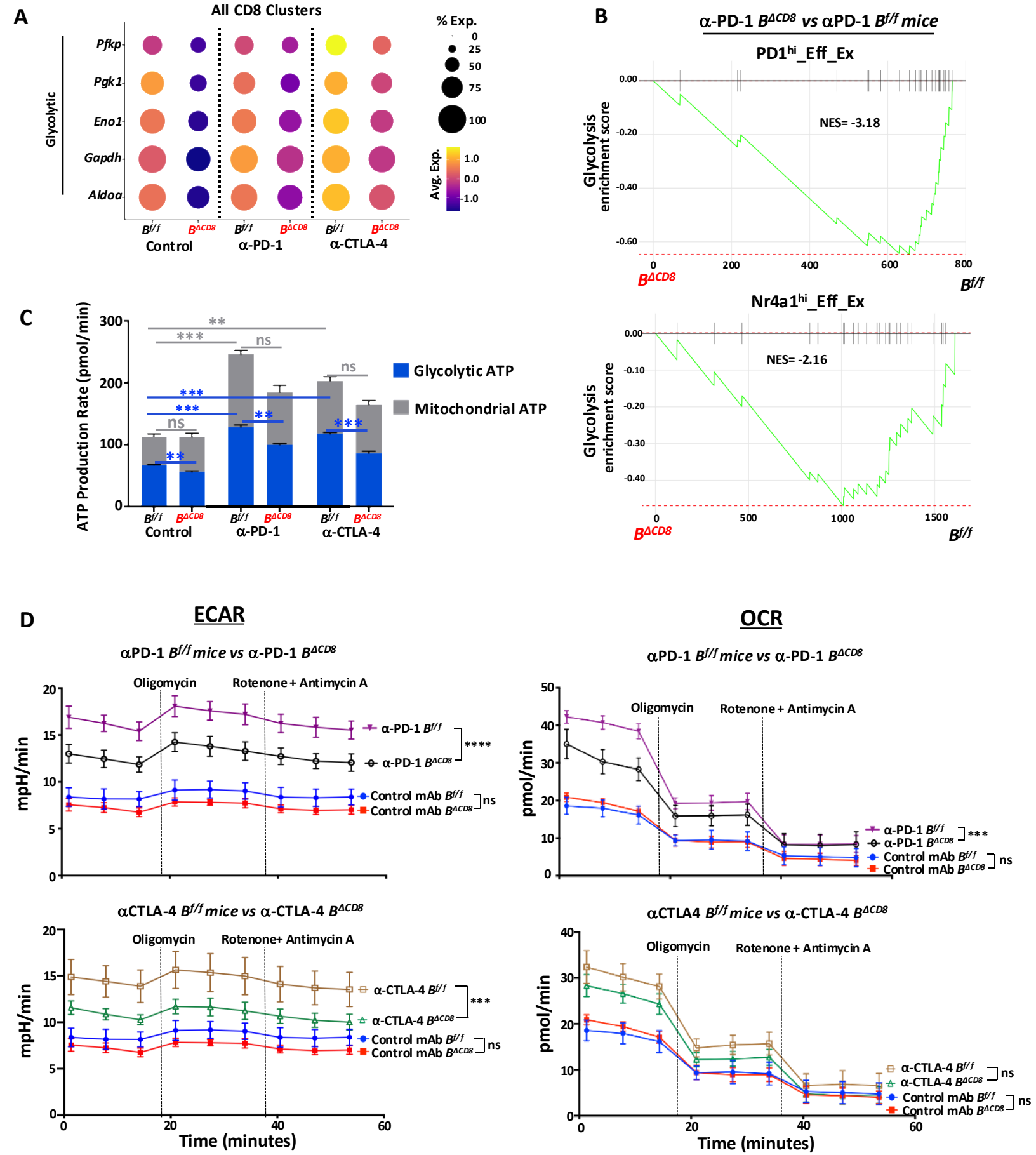
A
All CD8 Clusters
Glycolytic
Pfkp
Pgk1
Eno1
Gapdh
Aldoa
% Exp.
0
25
50
75
100
Avg. Exp.
1.0
0.0
-1.0
Control
α-PD-1
α-CTLA-4
B
α-PD-1 BΔCD8 vs αPD-1 Bf/f mice
PD1hi_Eff_Ex
NES= -3.18
Glycolysis enrichment score
Nr4a1hi_Eff_Ex
NES= -2.16
C
ATP Production Rate (pmol/min)
Glycolytic ATP
Mitochondrial ATP
D
ECAR
OCR
αPD-1 Bf/f mice vs α-PD-1 BΔCD8
Oligomycin
Rotenone + Antimycin A
α-PD-1 Bf/f
α-PD-1 BΔCD8
Control mAb Bf/f
Control mAb BΔCD8
mpH/min
pmol/min
αCTLA-4 Bf/f mice vs α-CTLA-4 BΔCD8
αCTLA4 Bf/f mice vs α-CTLA-4 BΔCD8
Rotenone+ Antimycin A
α-CTLA-4 Bf/f
α-CTLA-4 BΔCD8
Time (minutes)

Figure 6

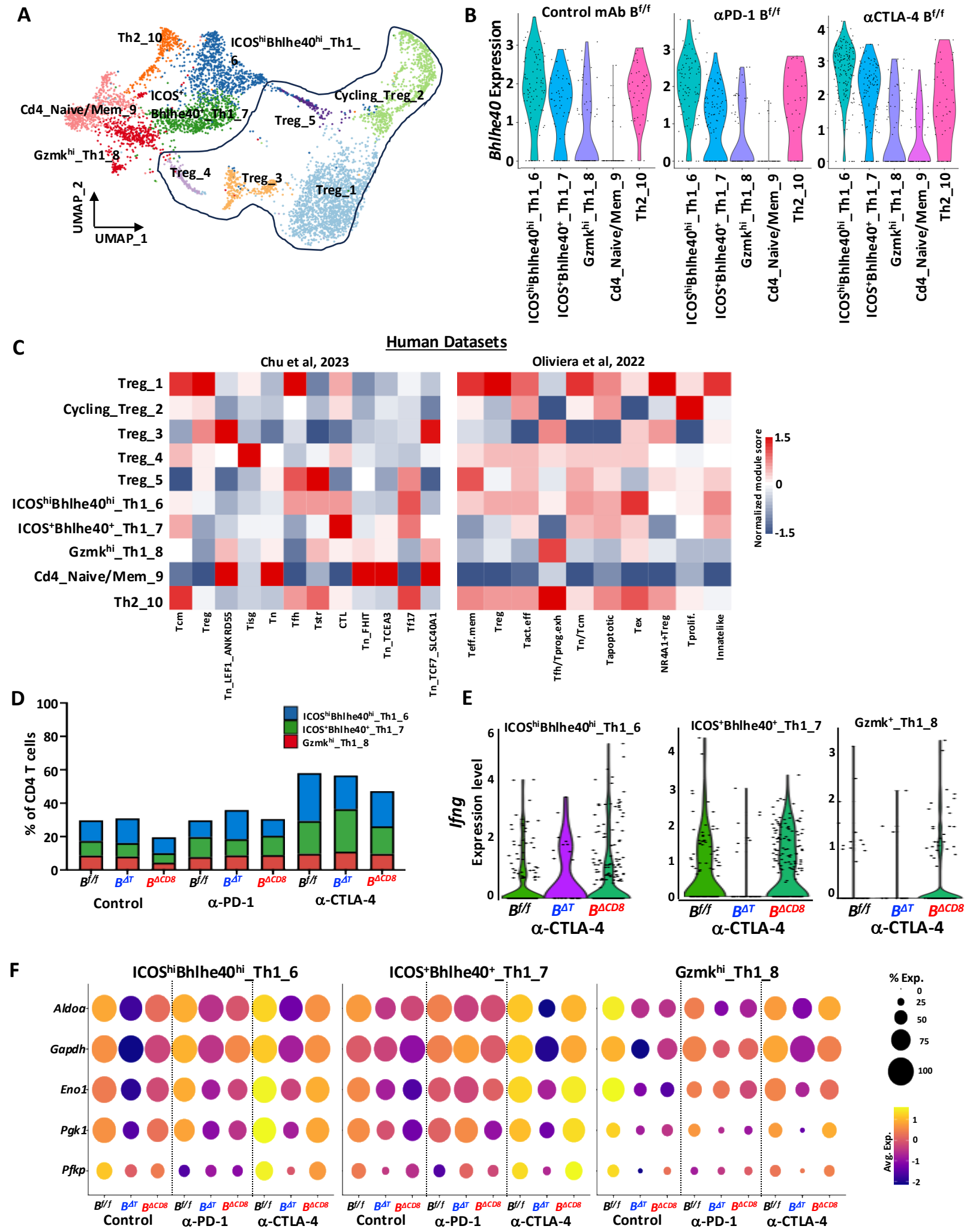
A
Th2_10
ICOS^hiBhlhe40^hi_Th1_6
ICOS+ Bhlhe40+_Th1_7
Cd4_Naive/Mem_9
Gzmk^hi_Th1_8
Cycling_Treg_2
Treg_5
Treg_4
Treg_3
Treg_1
UMAP_2
UMAP_1
B
Control mAb B^f/f
αPD-1 B^f/f
αCTLA-4 B^f/f
Bhlhe40 Expression
ICOS^hiBhlhe40^hi_Th1_6
ICOS+Bhlhe40+_Th1_7
Gzmk^hi_Th1_8
Cd4_Naive/Mem_9
Th2_10
C
Human Datasets
Chu et al, 2023
Oliviera et al, 2022
Treg_1
Cycling_Treg_2
Treg_3
Treg_4
Treg_5
ICOS^hiBhlhe40^hi_Th1_6
ICOS+Bhlhe40+_Th1_7
Gzmk^hi_Th1_8
Cd4_Naive/Mem_9
Th2_10
Tcm
Treg
Tn_LEF1_ANKRD55
Tisg
Tn
Tfh
Tstr
CTL
Tn_FHIT
Tn_TCEA3
Tf17
Tn_TCF7_SLC40A1
Teff.mem
Treg
Tact.eff
Tfh/Tprog.exh
Tn/Tcm
Tapoptotic
Tex
NR4A1+Treg
Tprolif.
Innatelike
Normalized module score
1.5
0
-1.5
D
% of CD4 T cells
ICOS^hiBhlhe40^hi_Th1_6
ICOS+Bhlhe40+_Th1_7
Gzmk^hi_Th1_8
B^f/f
B^ΔT
B^ΔCD8
Control
α-PD-1
α-CTLA-4
E
Ifng Expression level
ICOS^hiBhlhe40^hi_Th1_6
ICOS+Bhlhe40+_Th1_7
Gzmk+_Th1_8
B^f/f
B^ΔT
B^ΔCD8
α-CTLA-4
F
ICOS^hiBhlhe40^hi_Th1_6
ICOS+Bhlhe40+_Th1_7
Gzmk^hi_Th1_8
Aldoa
Gapdh
Eno1
Pgk1
Pfkp
Control
α-PD-1
α-CTLA-4
% Exp.
0
25
50
75
100
Avg. Exp.
1
0
-1
-2

Figure 7

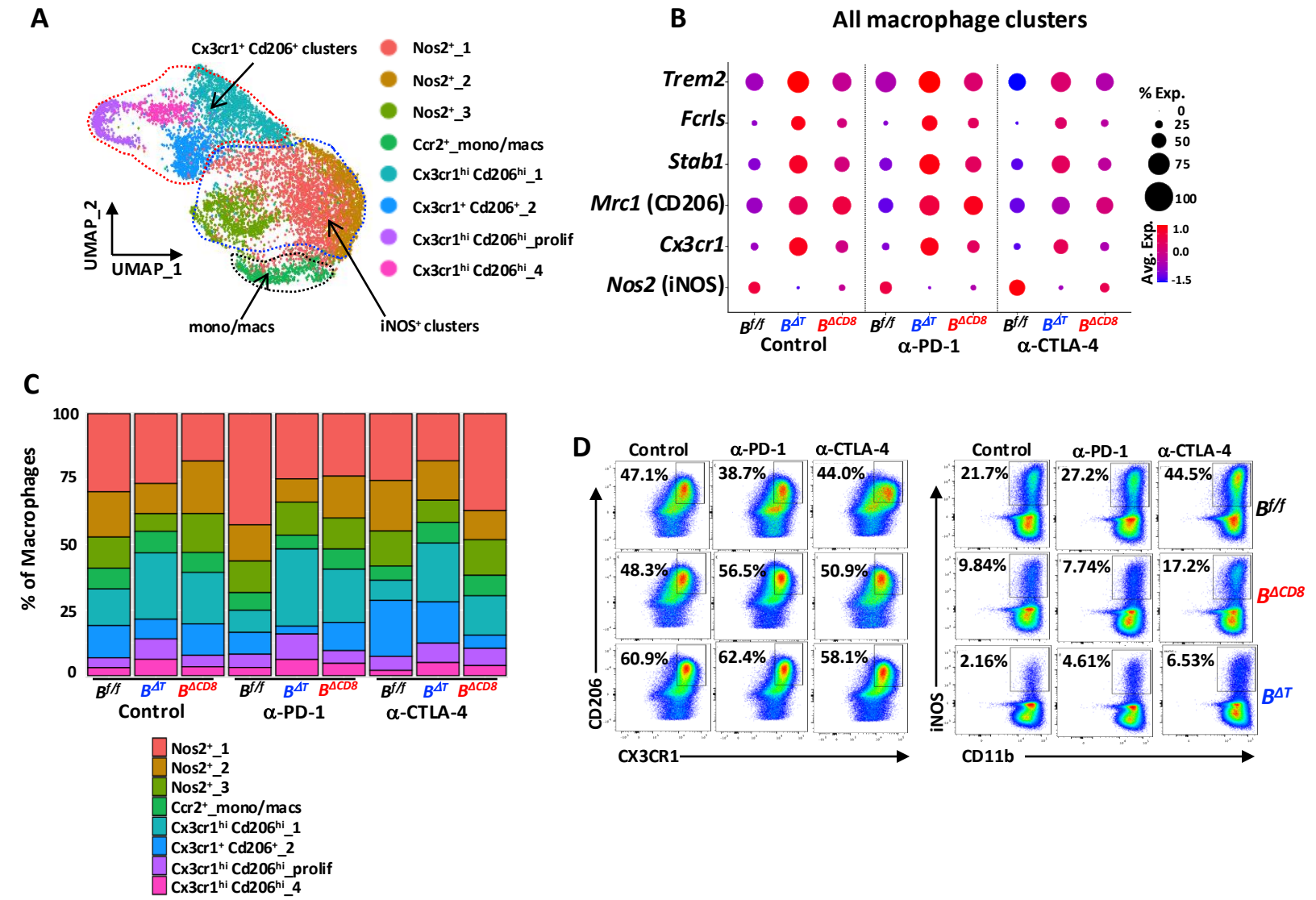
A
Cx3cr1+ Cd206+ clusters
Nos2+_1
Nos2+_2
Nos2+_3
Ccr2+_mono/macs
Cx3cr1hi Cd206hi_1
Cx3cr1+ Cd206+_2
Cx3cr1hi Cd206hi_prolif
Cx3cr1hi Cd206hi_4
UMAP_2
UMAP_1
mono/macs
iNOS+ clusters
B
All macrophage clusters
Trem2
Fcrls
Stab1
Mrc1 (CD206)
Cx3cr1
Nos2 (iNOS)
% Exp.
0
25
50
75
100
Avg. Exp.
1.0
0.0
-1.5
Bf/f
BΔT
BΔCD8
Control
α-PD-1
α-CTLA-4
C
% of Macrophages
100
75
50
25
0
Nos2+_1
Nos2+_2
Nos2+_3
Ccr2+_mono/macs
Cx3cr1hi Cd206hi_1
Cx3cr1+ Cd206+_2
Cx3cr1hi Cd206hi_prolif
Cx3cr1hi Cd206hi_4
D
Control
α-PD-1
α-CTLA-4
47.1%
38.7%
44.0%
48.3%
56.5%
50.9%
60.9%
62.4%
58.1%
21.7%
27.2%
44.5%
9.84%
7.74%
17.2%
2.16%
4.61%
6.53%
CD206
CX3CR1
iNOS
CD11b

Suppl. Figure 1

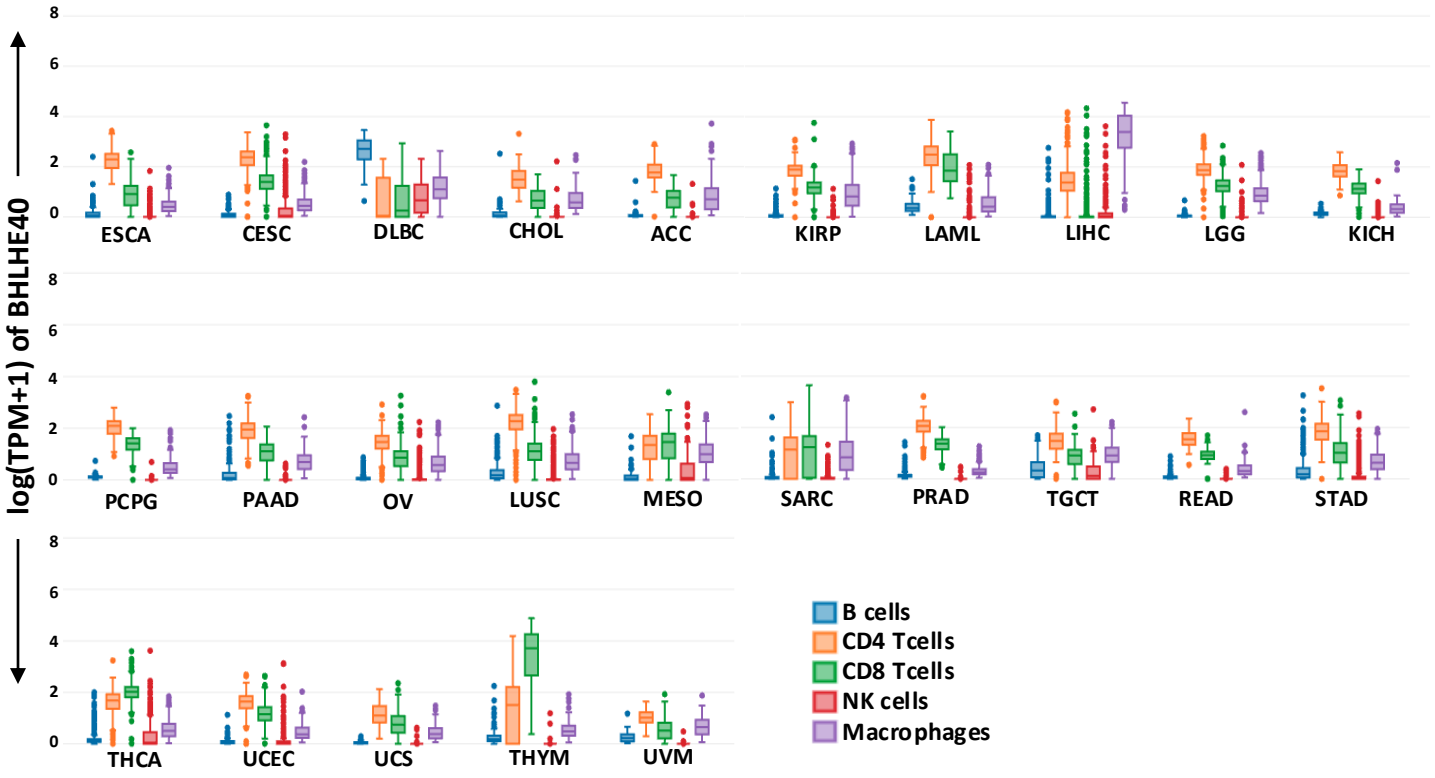

Suppl. Figure 2

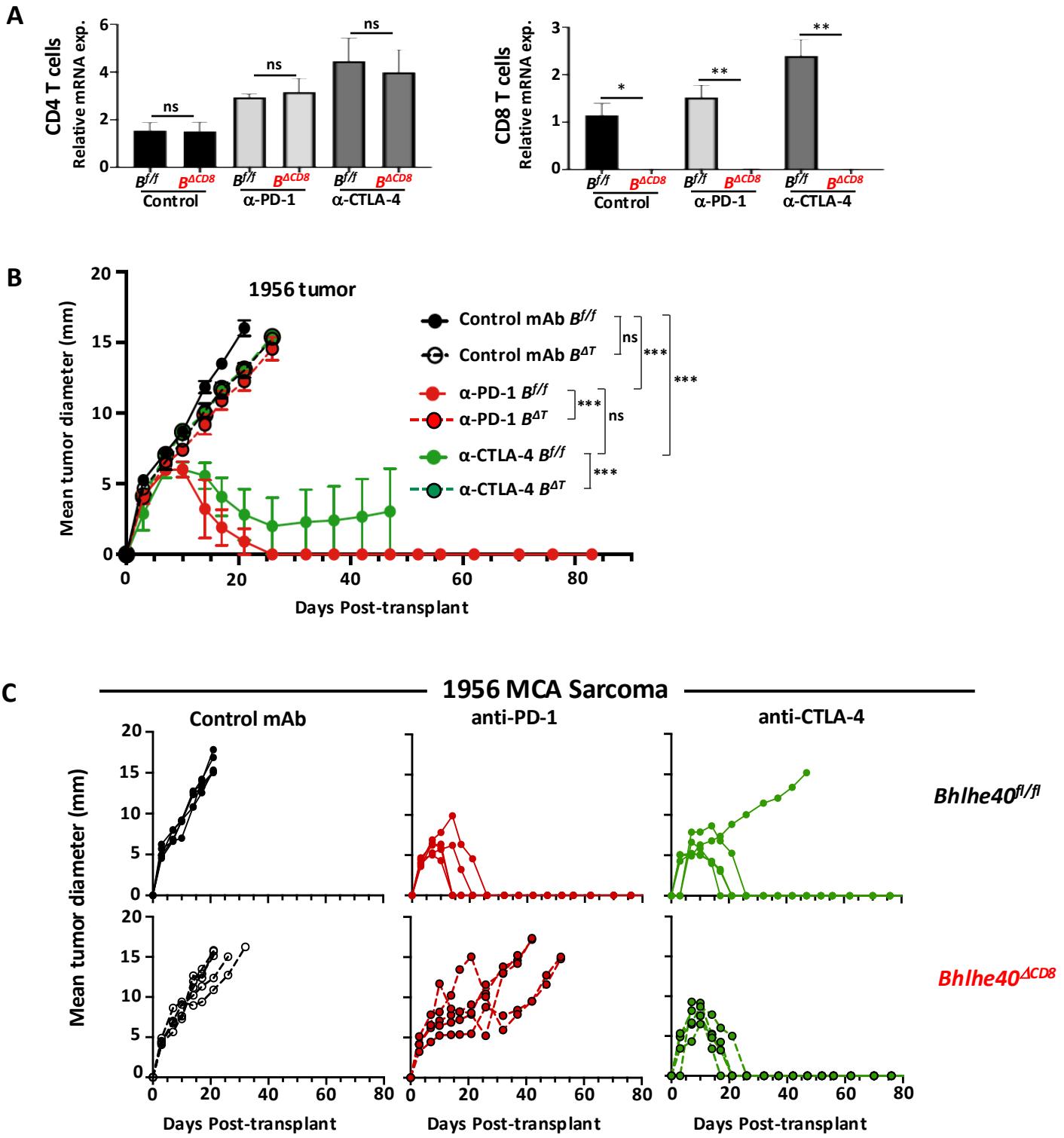

Suppl. Figure 3

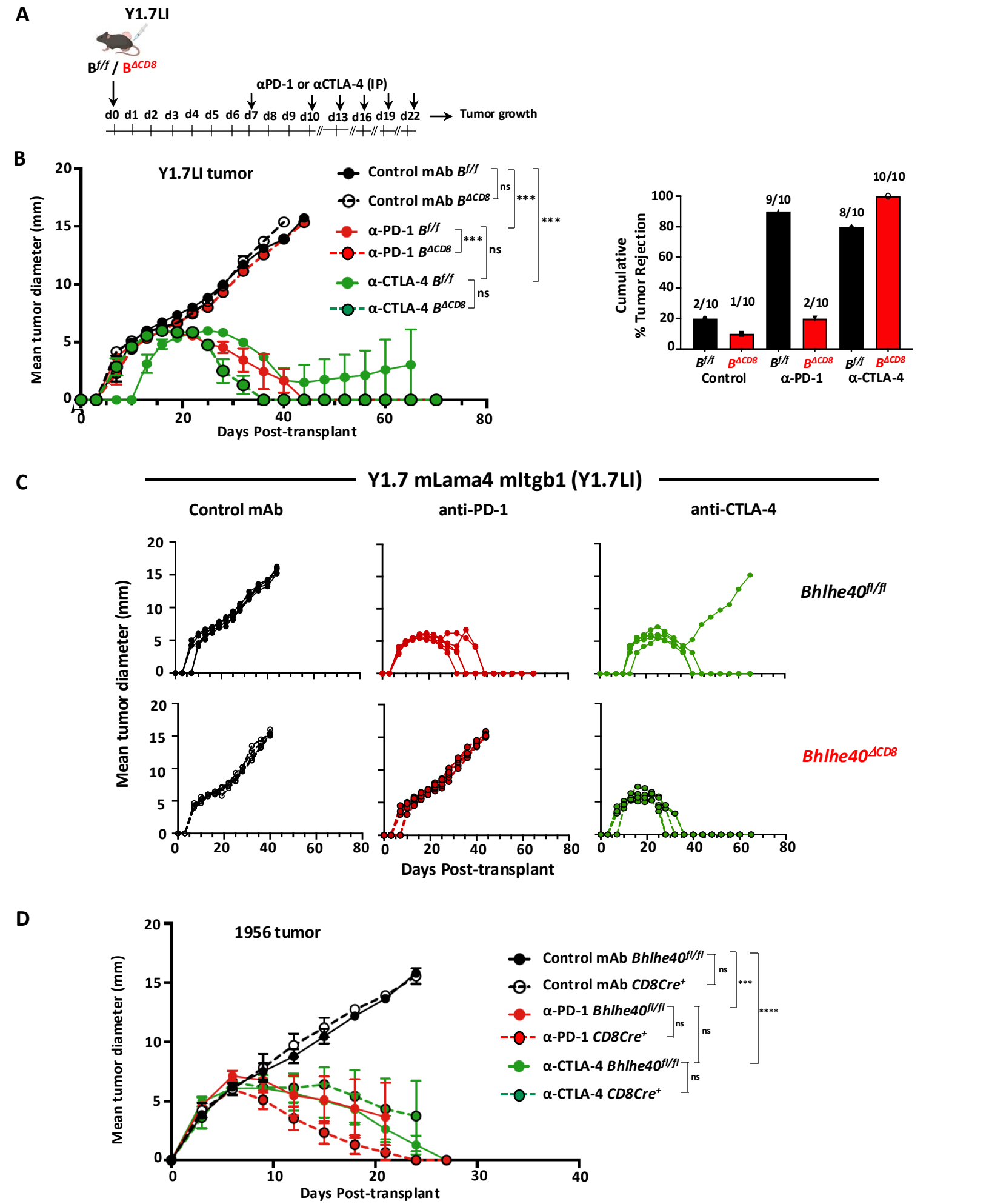

Suppl. Figure 4

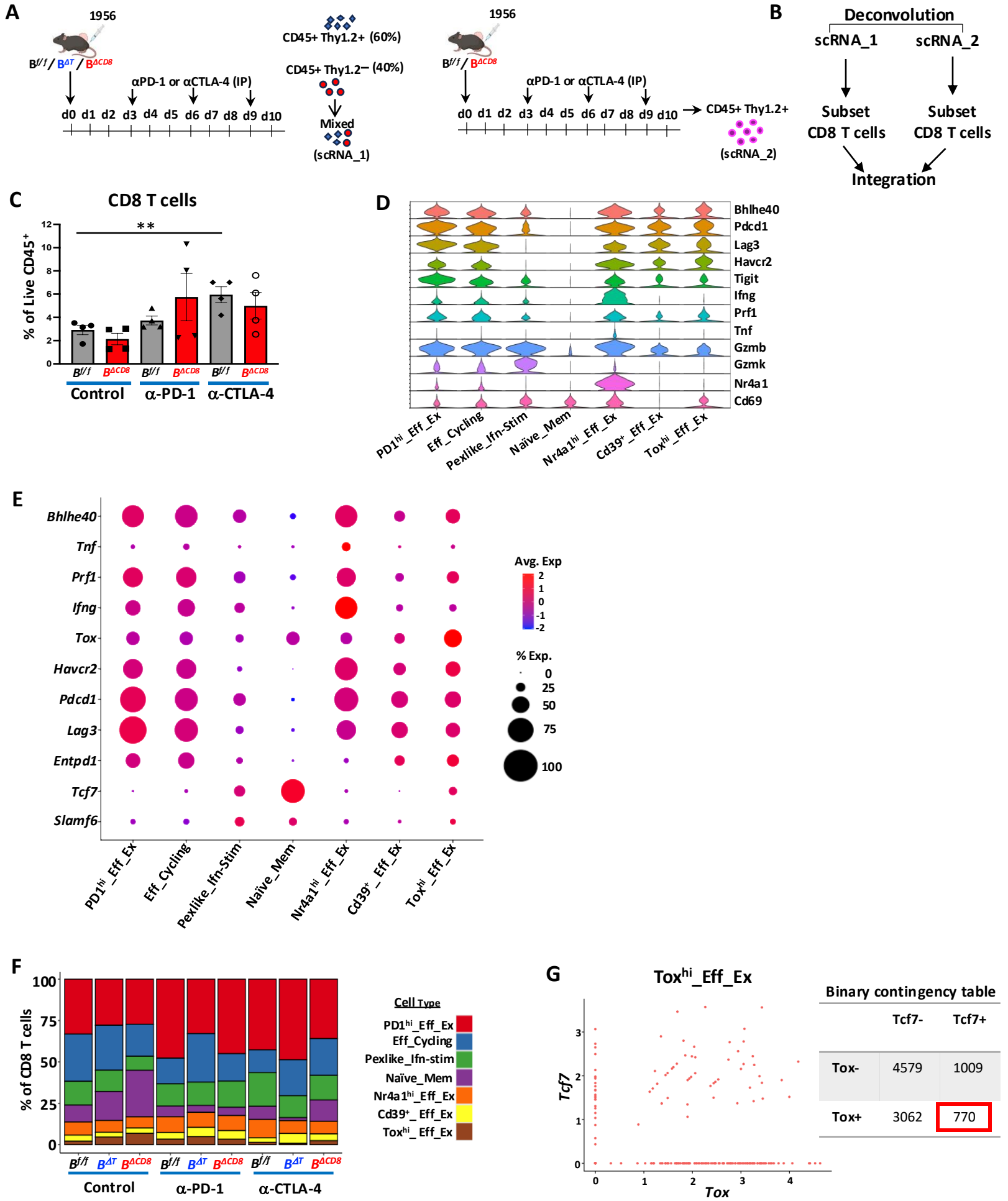

Suppl. Figure 5

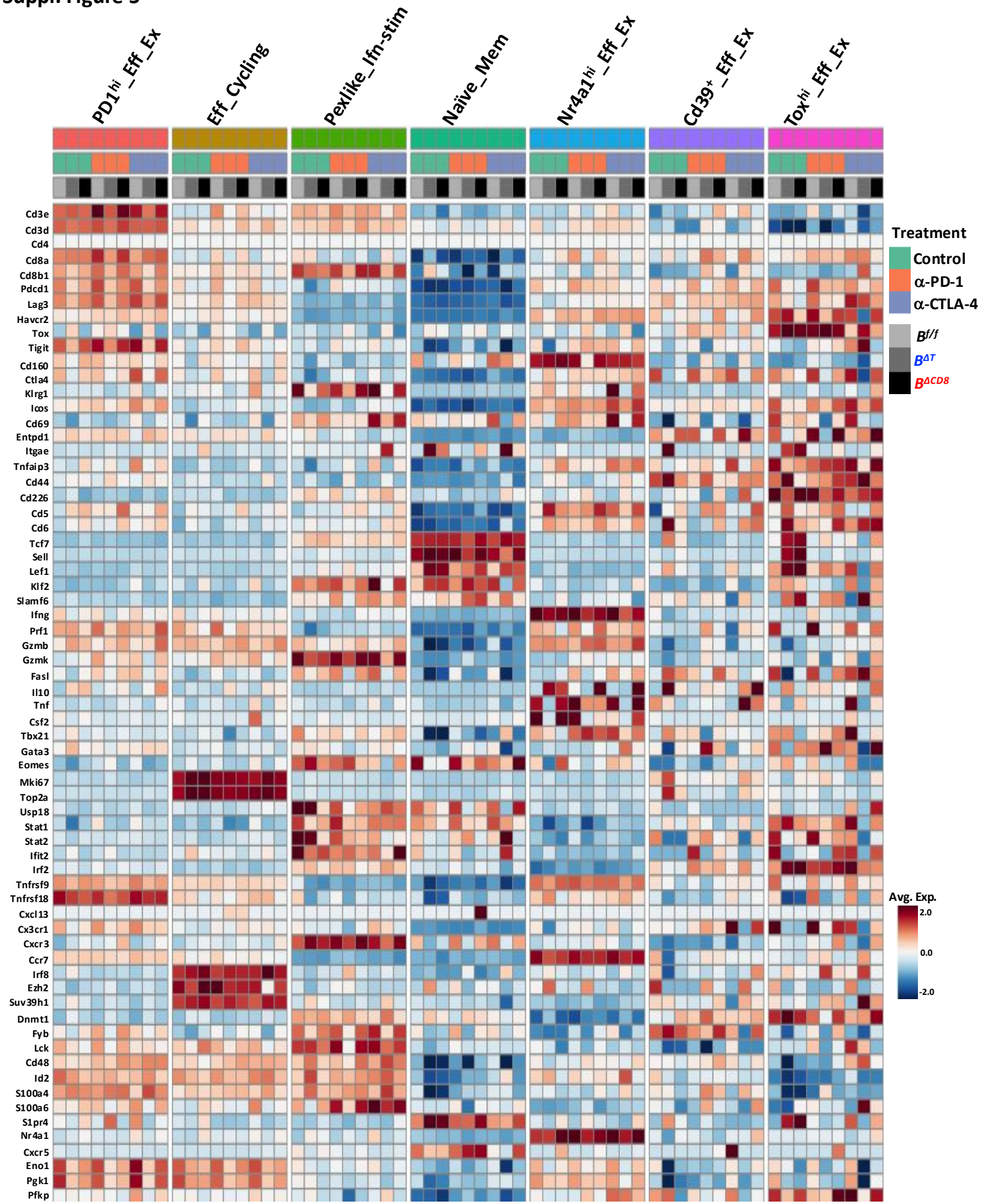

Suppl. Figure 6

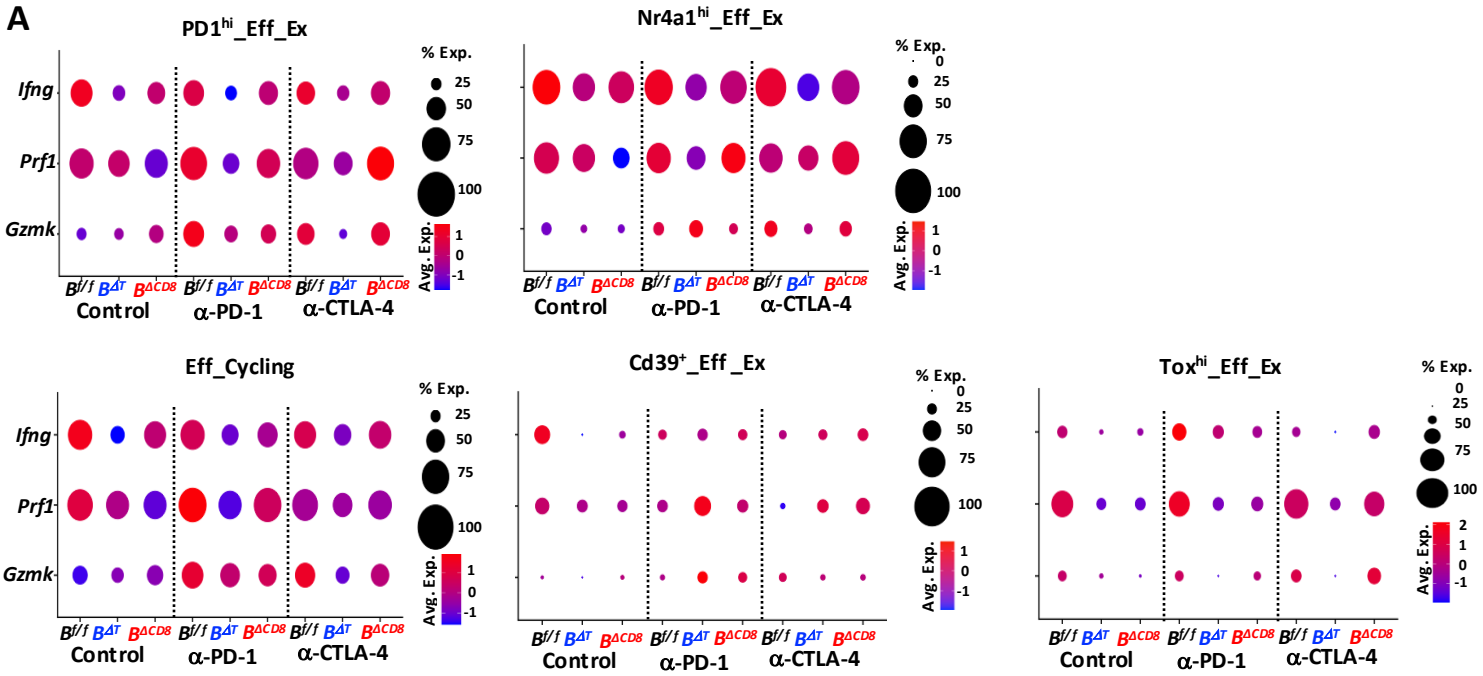

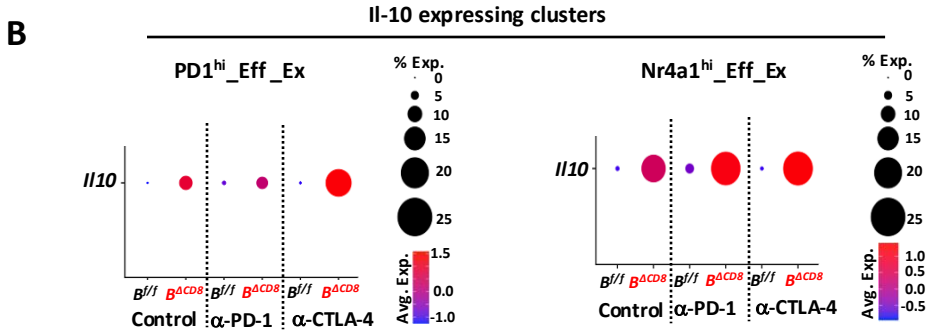

Suppl. Figure 7

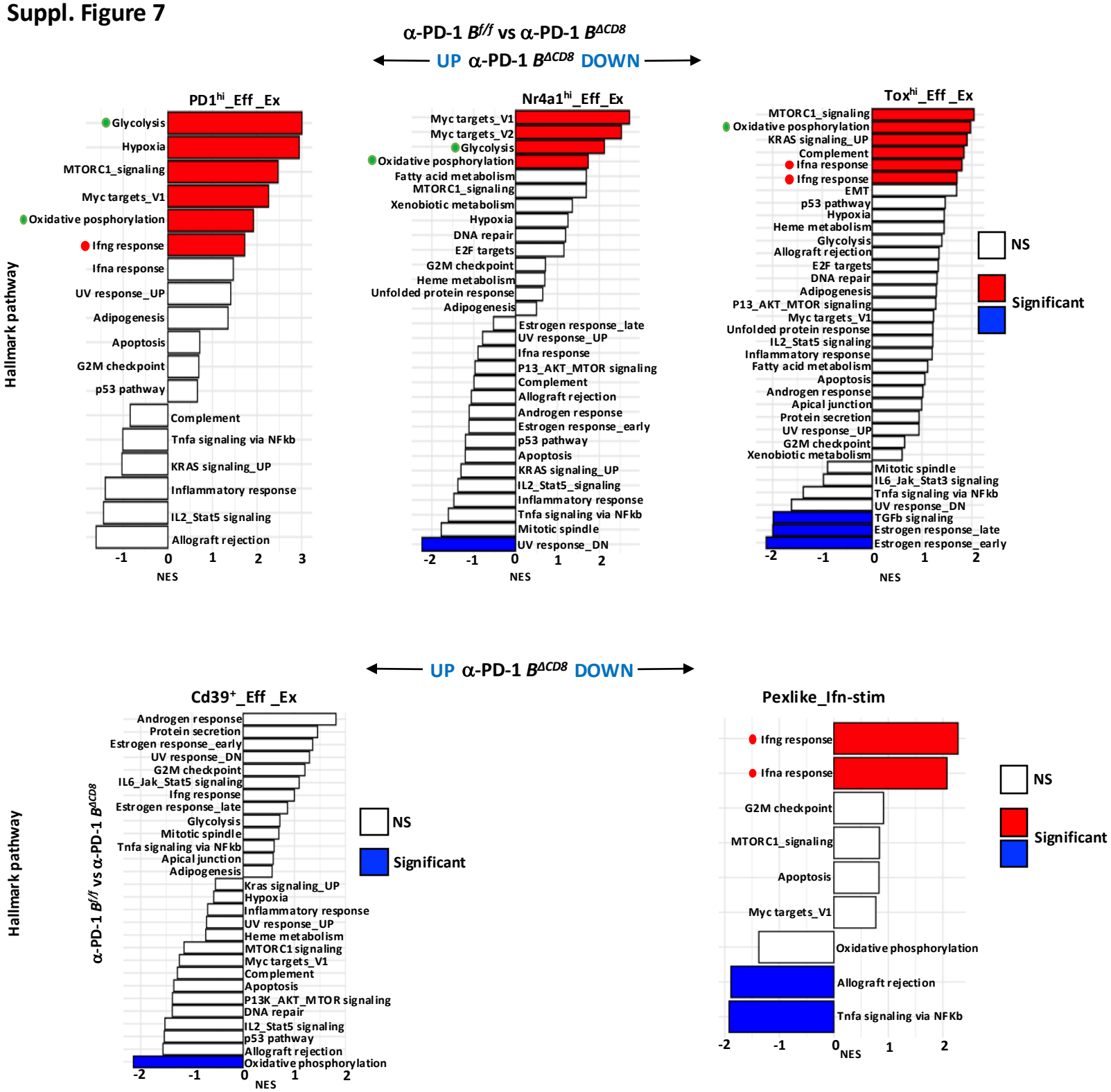

Suppl. Figure 8

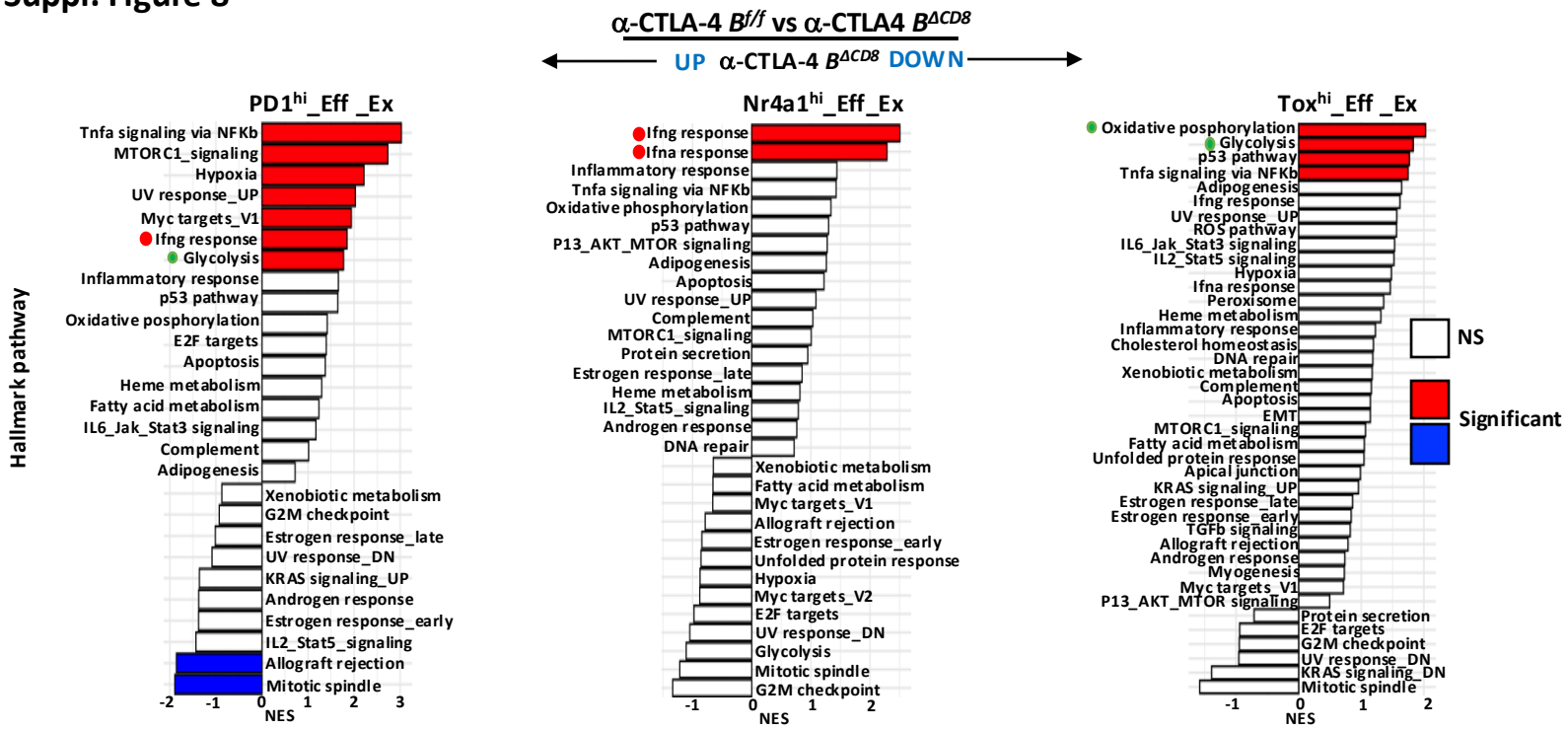

Suppl. Figure 9

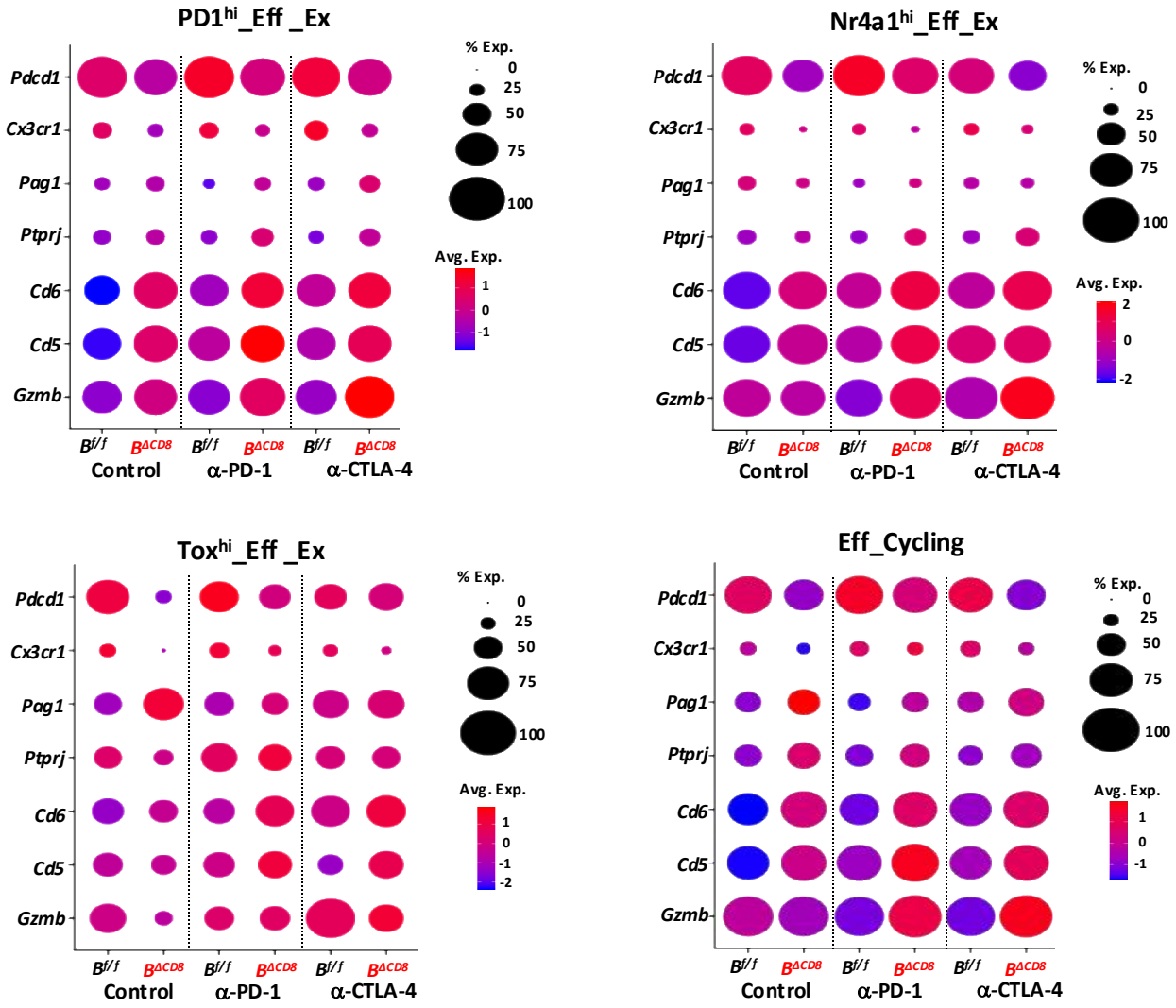

Suppl. Figure 10

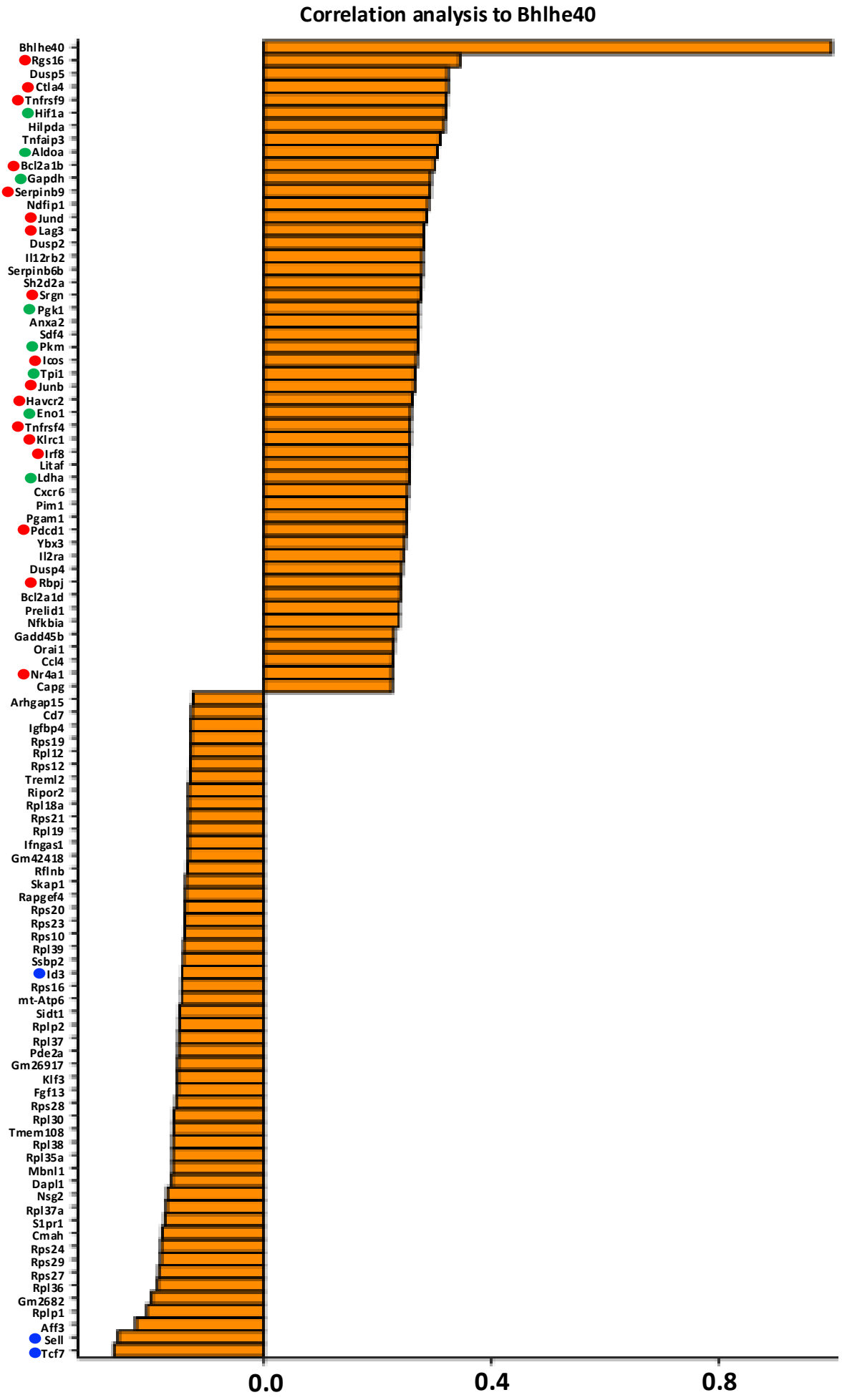

Suppl. Figure 11

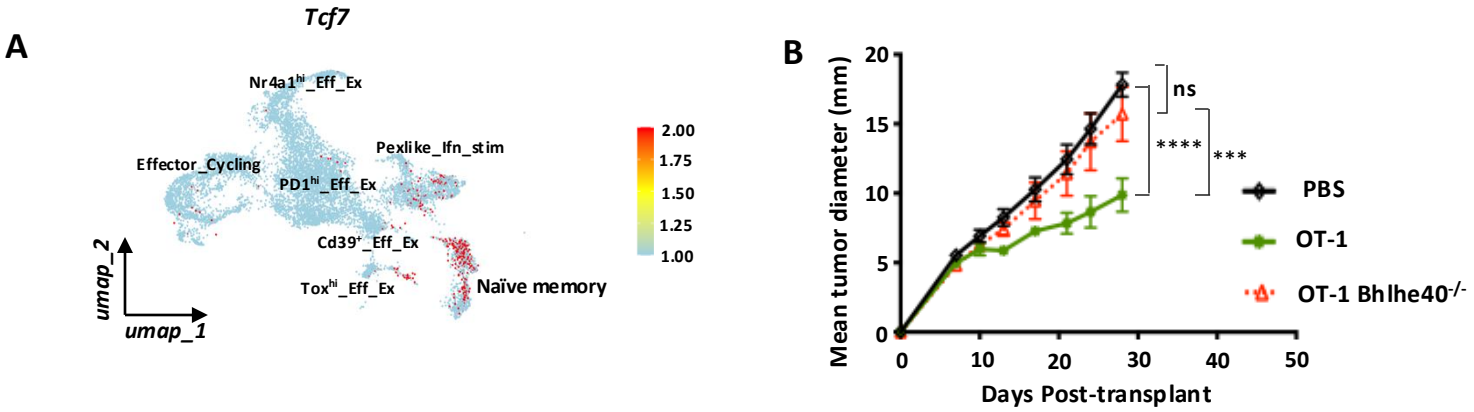

Suppl. Figure 12

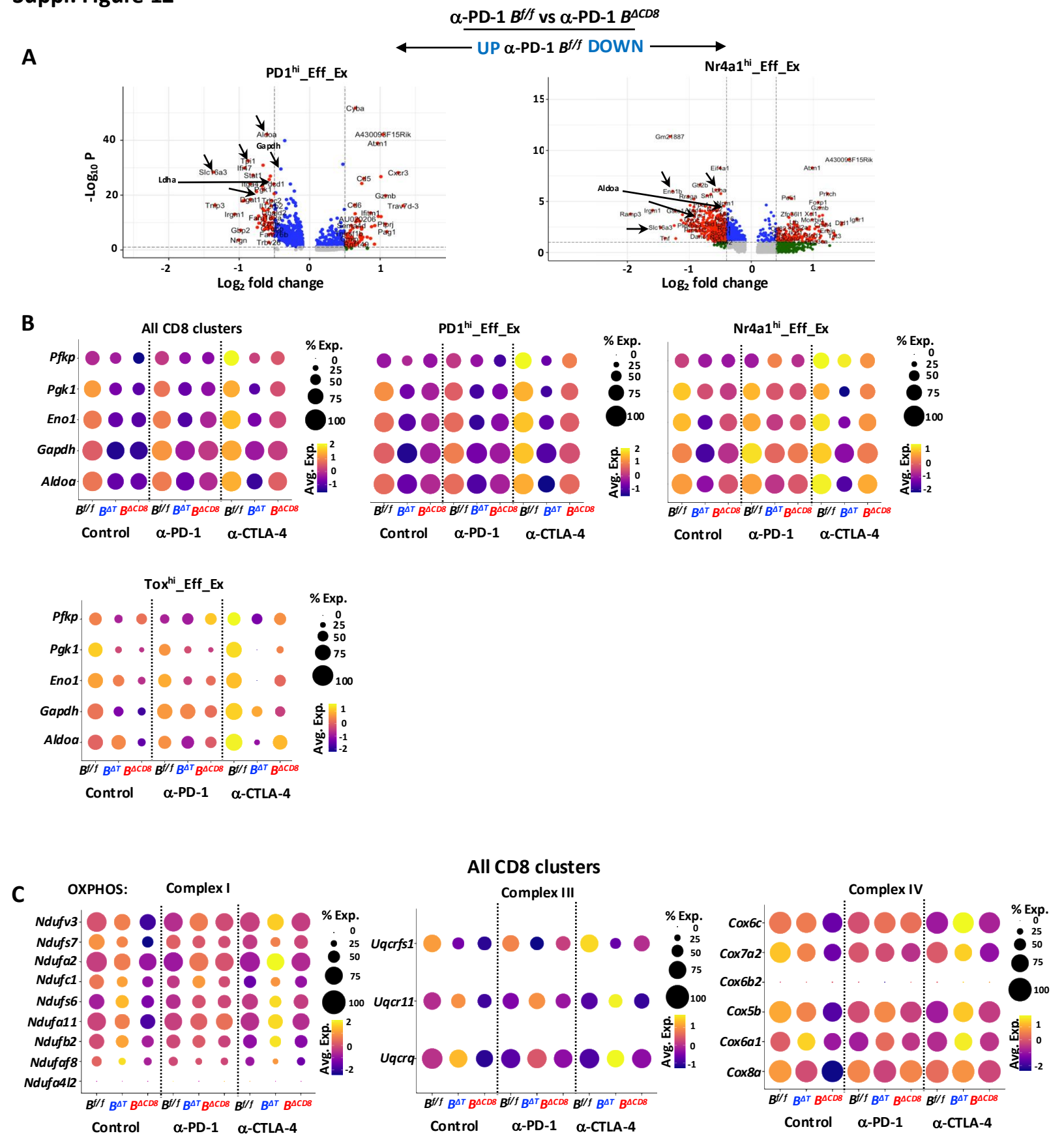

Figure S13

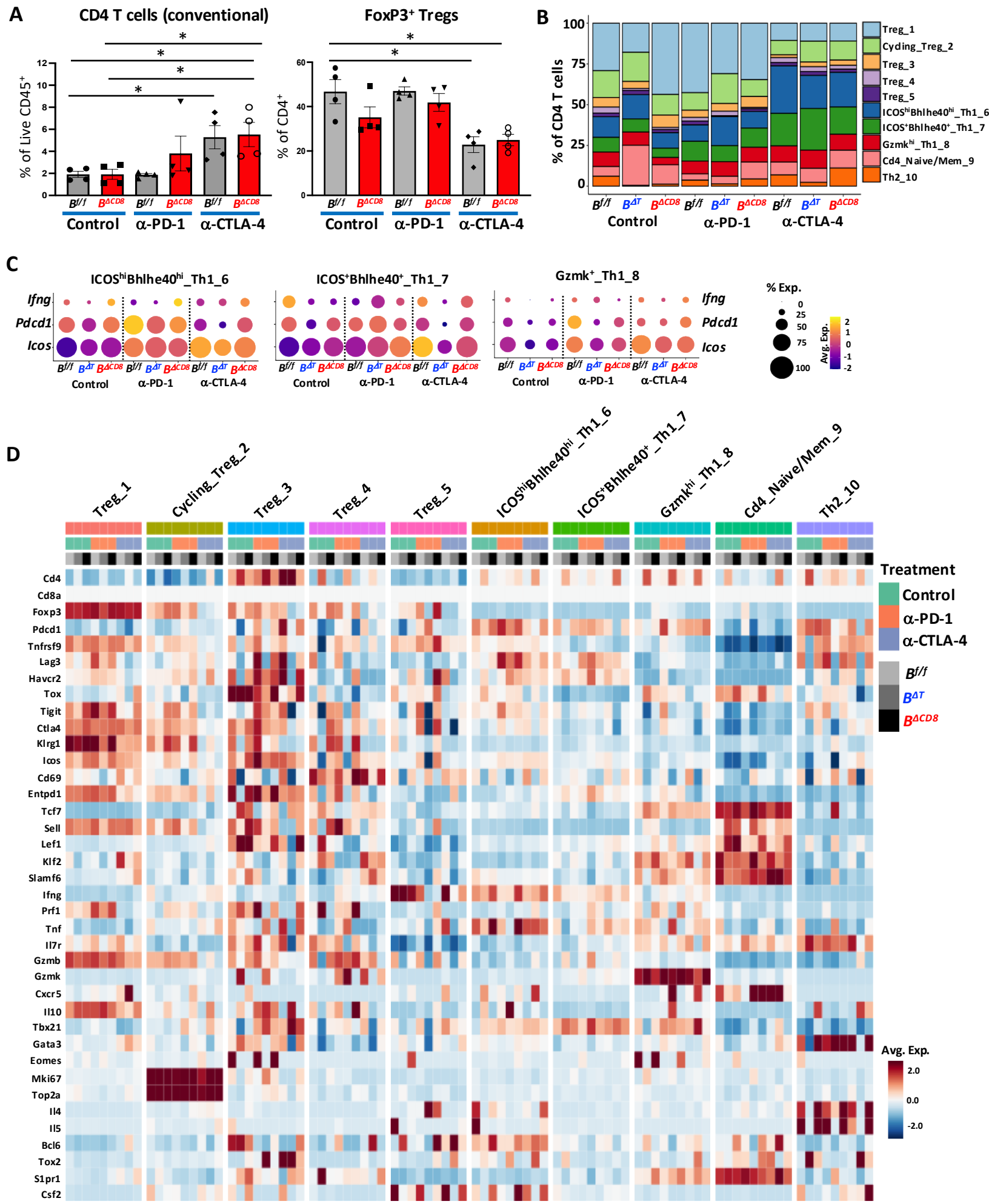
A
CD4 T cells (conventional)
FoxP3+ Tregs
% of Live CD45+
% of CD4+
Control
α-PD-1
α-CTLA-4
B
% of CD4 T cells
Treg_1
Cycling_Treg_2
Treg_3
Treg_4
Treg_5
ICOShiBhlhe40hi_Th1_6
ICOS+Bhlhe40+_Th1_7
Gzmkhi_Th1_8
Cd4_Naive/Mem_9
Th2_10
C
ICOShiBhlhe40hi_Th1_6
ICOS+Bhlhe40+_Th1_7
Gzmk+_Th1_8
Ifng
Pdcd1
Icos
% Exp.
Avg. Exp.
D
Treg_1
Cycling_Treg_2
Treg_3
Treg_4
Treg_5
ICOShiBhlhe40hi_Th1_6
ICOS+Bhlhe40+_Th1_7
Gzmkhi_Th1_8
Cd4_Naive/Mem_9
Th2_10
Cd4
Cd8a
Foxp3
Pdcd1
Tnfrsf9
Lag3
Havcr2
Tox
Tigit
Ctla4
Klrg1
Icos
Cd69
Entpd1
Tcf7
Sell
Lef1
Klf2
Slamf6
Ifng
Prf1
Tnf
Il7r
Gzmb
Gzmk
Cxcr5
Il10
Tbx21
Gata3
Eomes
Mki67
Top2a
Il4
Il5
Bcl6
Tox2
S1pr1
Csf2
Treatment
Control
α-PD-1
α-CTLA-4
Avg. Exp.